Polarimetric Synthetic Aperture Radar Image Processing and Applications for Earthquake/Tsunami Damage Assessment

July 2019

J I　Y A Q I

Graduate School of

Advanced Integration Science

CHIBA UNIVERSITY

(千葉大学審査学位論文)

Polarimetric Synthetic Aperture Radar Image Processing and Applications for Earthquake/Tsunami Damage Assessment

July 2019

J I　Y A Q I

Graduate School of

Advanced Integration Science

CHIBA UNIVERSITY

DECLARATION

I hereby declare that this submission is my own work and that, to the best of my knowledge and belief, it contains no material which to a substantial extent has been accepted for the award of any other degree or diploma of the university or other institute of higher learning, except where due acknowledgment has been made in the text.

Yaqi Ji, Chiba, July 2019

Polarimetric Synthetic Aperture Radar Image Processing and Applications for Earthquake/Tsunami Damage Assessment

Yaqi Ji

ABSTRACT

Polarimetric synthetic aperture radar (PolSAR) data perform excellently for earth information exploration. In this thesis, both the PolSAR image classification technique and the application of PolSAR image for earthquake/tsunami damage assessment are introduced. Firstly, an unsupervised classification method for PolSAR image is presented and discussed. This algorithm employs the sparse representation theory. Based on the designed energy function, a kind of iteration optimization algorithm is proposed for class labels and dictionary updating. Three airborne PolSAR datasets are tested. Comparison with supervised and unsupervised algorithms verifies the excellent performance of this classification method. The PolSAR image can be applied for disaster monitoring to obtain fast and accurate detection results. Two kinds of earthquake/tsunami damage assessment methods are also introduced in this thesis. The first algorithm gives the damage level assessment result, which employs the two data obtained before and after the event. An index is designed based on the valid polarimetric features' change before and after the disaster event. Based on this index, accurate damage level map can be created to show the severity of building damage. Both the Tohoku earthquake event and the Kumamoto earthquake event are analyzed to test the validity of this method. The second damage assessment method is based on a single post-event PolSAR image. This unsupervised algorithm does not need prior damage information for training processing. It considers the complex damage situation that damaged buildings may under large orientation angle. All urban areas are classified into four categories, and all the damaged buildings can be figured out. This algorithm is tested by analyzing the Tohoku earthquake event. The comparison with the supervised method shows its superiority.

偏波合成開口レーダ画像処理と地震·津波損傷評価への応用

概要

近年、偏波合成開口レーダ（PolSAR）による地球観測が盛んに行われている。本論文では、PolSAR画像分類技術および地震　津波被害評価を目的とした応用研究を行った。まず、新しいエネルギー関数が定義された。その原理は、スパース表現エラーを最小限に抑え、隣接するピクセルに同じラベルを付けるように強制することである。このエネルギー関数に基づいて、クラスラベルと辞書の両方を更新するための反復最適化法を提案した。航空機搭載のPolSARデータを用いて、他の教師付き分類法および教師無し分類法との比較により、本提案手法が最良の性能であることを示した。また、この論文では2種類の地震　津波被害評価方法を紹介した。まず、新しい損傷レベルの指標は、災害発生前後の偏波特性の変化に基づいて設計され、建造物の損傷度合いを示すための正確な損傷レベルマップがこの指標に基づいて作成可能である。東北地方太平洋沖地震と熊本地震を解析し、この指標の妥当性を検証した。2つ目の方法は、単一の地震後のPolSAR画像に基づくものである。衛星の飛行経路と平行でない損傷した建造物を考慮して、建造物を4種類のカテゴリーに分類した。この方法は、東北地方太平洋沖地震の分析に活用され、教師付き方法と比較することでその優位性を示すことができた。将来、この研究成果はPolSARによる災害監視に活用可能であると期待される。

Acknowledgement

I would like to express my gratitude to all those who helped me during the process of my doctoral study.

I gratefully acknowledge the help of my supervisor, Professor. Josaphat Tetuko Sri Sumantyo, who has offered me valuable suggestions in my academic studies. His incisive comments and constructive criticism helped me to solve the countless problems in my research. I do appreciate his patience, encouragement, and professional instructions for both my academic work and daily life.

I would like to express my gratitude to all the staffs and students of Josaphat Microwave Remote Sensing Laboratory (JMRSL) for their help during my three years' study at Chiba University. Especially Doctor. Ming Yam Chua, who gave me a lot of valuable advises for the improvement of my work.

I appreciate my family, who has always been supporting and caring for me all of my life. Many thanks to my husband, Doctor. Xinyi Li, for his encouragement and supporting for my study.

Contents

List of Figures

81

List of Tables

1

Introduction

1.1 Background

Synthetic Aperture Radar (SAR), as a rapidly developing microwave remote sensing technology, can provide high-resolution images for earth exploration. SAR system is mounted on a flight carrier, and it moves relative to observation target. By transmitting microwave pulses to the target surface and receiving scattered electromagnetic signals, the long-range targets' high-resolution images can be obtained. SAR system is often used for military target identification, in civil, often used for topographic mapping, disaster monitoring, mineral resources exploration, ship detection, and so on.

Polarimetric SAR (PolSAR) remote sensing technology provides abundant and reliable information of surface features of the earth, which can be applied to interpret the characteristics of objects. PolSAR is an imaging radar used to measure the polarization characteristics of the target and obtain the target image at the same time, it receives and transmits electromagnetic waves of different polarization modes. Choosing the best polarization mode can suppress the clutter and improve the anti-interference ability. By analyzing electromagnetic waves of various polarization modes, more information of target ground objects can also be obtained. The polarization scattering matrix [1] obtained by SAR radar contains the complete electromagnetic scattering characteristics of objects, by exploring which, the polarization characteristics of the objects can be obtained. Data obtained by the polarimetric SAR system provide a sufficient basis for subsequent classification, identification, and other processing, and can be successfully applied to crop detection and disaster estimation, detection of deforestation and fire analysis.

The above advantages of PolSAR system make it receive great attention. After decades of development, PolSAR theory system has been quite perfect, and great progress has been made in image application research. A large amount of data obtained by PolSAR system can support the further analysis and processing of PolSAR image, and it also promotes the development of PolSAR information processing technology.

Further processing and analysis of PolSAR images is the main way to obtain detailed information of target features. This thesis introduces both the image processing technique and the application of PolSAR data for disaster monitoring. PolSAR image processing techniques include segmentation, classification, edge detection, target recognition, and so on. A novel unsupervised PolSAR image classification algorithm is introduced in this thesis. It means the classification of image data with pixel points or pixel sets as the unit; this work is to set class labels to this unit by analyzing its characteristics. The classification results can be directly fed back to users as the final data or used for further image processing. The application of PolSAR data for disaster monitoring is also introduced. Two kinds of damage assessment algorithms are proposed for earthquake/tsunami disaster events. This kind of technique can quickly detect out damaged buildings which can provide information rapidly for after disaster rescue and city reconstruction.

1.2 Development of PolSAR image classification technique

Classification using PolSAR datasets [2–4] is one challenging work in remote sensing. It can be classified into two classes according to the characteristics. According to the statistical properties of PolSAR image [5–10], or considering the polarimetric scattering mechanisms [11–15]. Considering about the usage of training data is another way to category classification methods. It is supervised and unsupervised algorithms. Supervised methods can obtain trained classifiers by training samples with label information. These training samples can be extracted from ground-truth information. After training processing, the trained classifiers will be applied to calculate the class labels for test data.

Kong et al. [16] is the first team that did the PolSAR image classification work successfully. They utilized maximum likelihood (ML) classifier [17–19]. After that, many machine learning techniques have been widely utilized. Such as neural network [20], random forest (RF) [21, 22], support vector machine (SVM) [23–25]. SVM presents high generalization capability. In 2001, Fukuda and Hirosawa [23] did the PolSAR image classification work using SVM method successfully. That is the first time of this classifier's application in this filed. After that, the SVM classifier is widely used [24,25].

Sparse representation theory is another widely used technique for PolSAR image classification. Its principle is presented as Figure 1.1, where every block means a atom of a vector or a matrix, different color represents for different value while white color means value zero. Every test pixel can be represented by several dictionary atoms, and the obtained sparse coefficient is sparse. Pixel-based classification results can be obtained by directly using spare representation classifier (SRC) [26]. To solve the optimization problem, Zhang's team [27] introduced the Simplified Matching Pursuit (SMP) method. Feng et al. [28] proposed a new classification method considering the segmented region as a unit. They combined the majority voting and the joint sparse representation based classifier [29].

Supervised classification techniques need training processing to get an effective classifier. Compared with the performance of supervised methods, its results generally have higher accuracies. But some target areas may not have corresponding ground-truth information, and the unsupervised classification techniques can perform well.

Unsupervised classification algorithms set class labels by exploring terrains' physical characteristics. The method by Cloude and Pottier [12] is one of the classical techniques. Scattering angle α and entropy H can create a plane. All the terrain targets can be classified into eight classes, and every class will be located in the zones on the plane. The algorithm by Kersten et al. [30] compared five clustering techniques, and they gave the conclusion that the Wishart distribution based method is the most effective. The unsupervised method designed by Yu et al. [31] combines the region growing technique and the Markov random field (MRF) model. Zhong et al. [32] proposed a sparsity-based

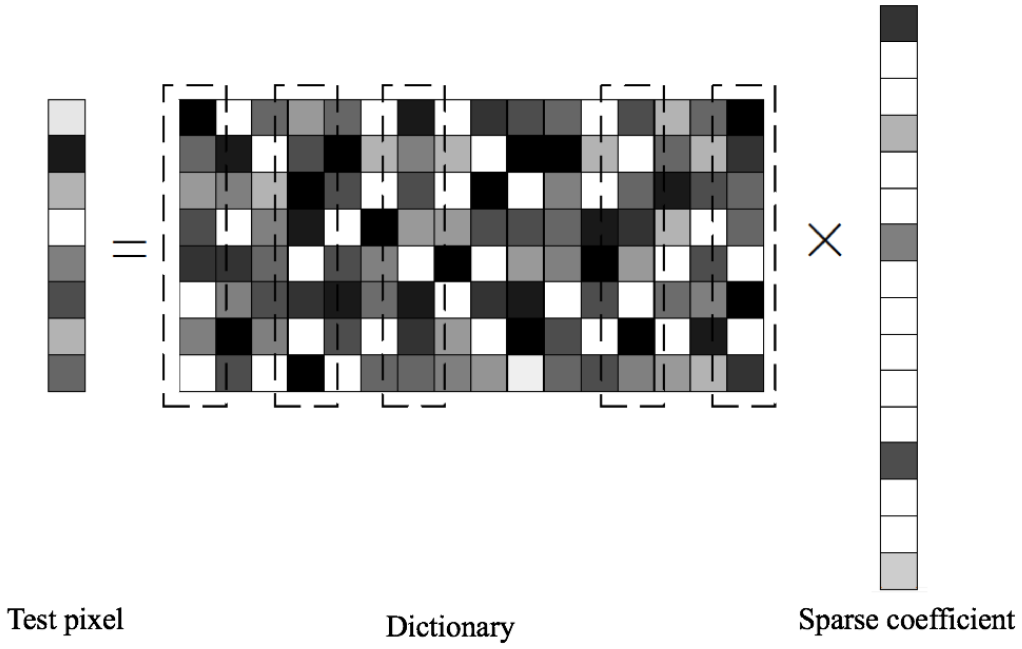

Figure 1.1: Principle of sparse representation theory

similarity measure. They defined a Riemannian sparse coding scheme to represent each Hermitian positive definite (HPD) matrices, and spectral clustering was used to cluster the resulting sparse coefficient vectors.

1.3 Introduction of PolSAR image for disaster damage assessment

Fast and accurate after disaster event damage assessment is one of the most predominant work for human [33]. Ground-survey based methods can be utilized to detect damage information. This kind of method can always obtain accurate results. However, its highly time-consuming [34] brings the consequence that fast response cannot be done. Remote sensing technology is a much better choice. It can give a quick response for a large scale area. Both SAR images and high-resolution optical images [35, 36] are suitable tools [37–39]. Direct interpretation of disaster situation can be extracted from high-resolution optical images [40–42]. However, the usage of this technique will be easily influenced by the night time and uncooperative weather. SAR system can be operated in the whole day. Different weather condition also makes little influence. Thus,

disaster monitoring work can be done excellently by SAR data. Polarimetric information is sensitive to objects' characteristics [4]. It makes PolSAR data an useful tool for earth information detection.

It is Yamaguchi [43] who used PolSAR data for disaster monitoring for the first time. He analyzed four types of disaster events using images composed by scattering power. The color changes can be found between the two images obtained before and after the event. This change is significant evidence that can be applied in disaster-hit areas identification. Polarimetric parameters obtained from four-component decomposition was used, by analyzing which, the author found that color variation caused by the value change of double-bounce and surface scattering is a good indicator for disaster damage. Figure 1.2 shows the main scattering mechanisms for a building before and after the disaster event. It is shown that double-bounce scattering will decrease after the disaster event. After Yamaguchi's research, many other works that monitor disaster damage by PolSAR images have been proposed. In 2013, Singh and Yamaguchi [44] identified disaster-affected areas based on double-bounce scattering power's change between the PolSAR data obtained before and after the earthquake event. Sang-Eun Park and Yamaguchi [45] detected the change of nine polarimetric features after the earthquake, and Expectation-Maximization (EM) [46] based thresholding approach was introduced. An approach that uses the Markov Random Field (MRF) is introduced [47], and it can create the change map. Damage area detection by PolSAR data has achieved great success. Damage level mapping can be used to provide information for life rescue and city reconstruction. However, only several types of research provide a rough damage level information. For Singh and Yamaguchi's [44] research, double-bounce scattering power's value change was classified into seven degrees to identify damage level. Chen et al. [48, 49] analyzed the relationship between damage with the change rule of double-bounce scattering power, and they proposed an index to represent damage levels.

The works mentioned above are using two datasets to explore the value change. In some situation, matched pre-event PolSAR data is not available [50]. Thus, only using post-event PolSAR image is another way to monitor disaster damage. All the buildings

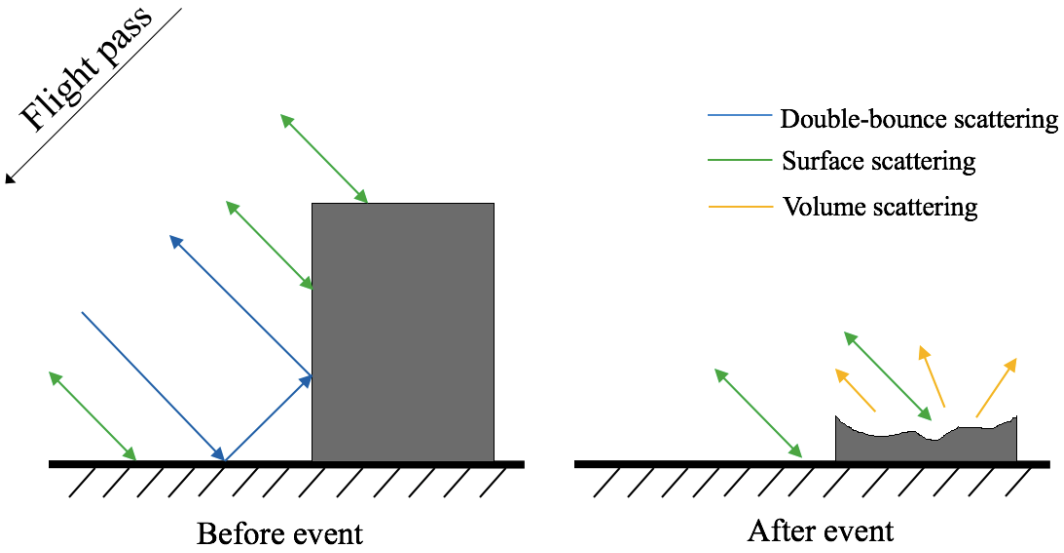

Figure 1.2: The change of scattering mechanisms for a building before and after the disaster event

can be divided into parallel buildings and oriented buildings according to their orientations. Figure 1.3 is the illustration of these two kinds of building. Parallel building means the building that parallel to the flight pass while oriented building means the building that divergent to the flight pass. These two building situations should be analyzed to detect all the damaged buildings when using single post-event image. For this kind of work, several outstanding algorithms have been proposed. Li et al. [51] introduced a novel algorithm to explore the spatial distribution of damaged buildings. Their work is based on the circular correlation coefficient ρ for the reason that this parameter has a high correlation with man-made structures. Unfortunately, the situation with oriented buildings was not analyzed. H-α-Wishart classification and normalized circular correlation coefficient are introduced in the work of Zhao et al. [52]. They detected both the damaged buildings and oriented buildings. The work of Zhai et al. [50, 53] introduced two damage assessment algorithms. Both of them used supervised Wishart classifier. Urban areas were classified into three classes by the method [50]. The work by Zhai et al. in [53] is to remove all the other regions except the damaged buildings. They introduced the HH-HV correlation coefficient (ρ_{HHHV}) and normalized difference of the dihedral component [54]. These two supervised techniques can acquire satisfac-

tory building damage maps. However, training processing is needed, which means that they need prior damage information. Thus they can not be used for real-time disaster monitoring. On the other hand, complex building structures may exist, for example, the damaged buildings under large orientation angle. This kind of building can be easily categorized to oriented and undamaged. Methods based on texture features [55, 56] were also proposed for post-event SAR image analysis. Shi et al. [55] used 181 kinds of features. They gave the conclusion that the texture feature can be employed for damage detection. Sun's team [56] used the random forest classifier. They combined five texture descriptors. However, this kind of techniques requires SAR images in very high resolution.

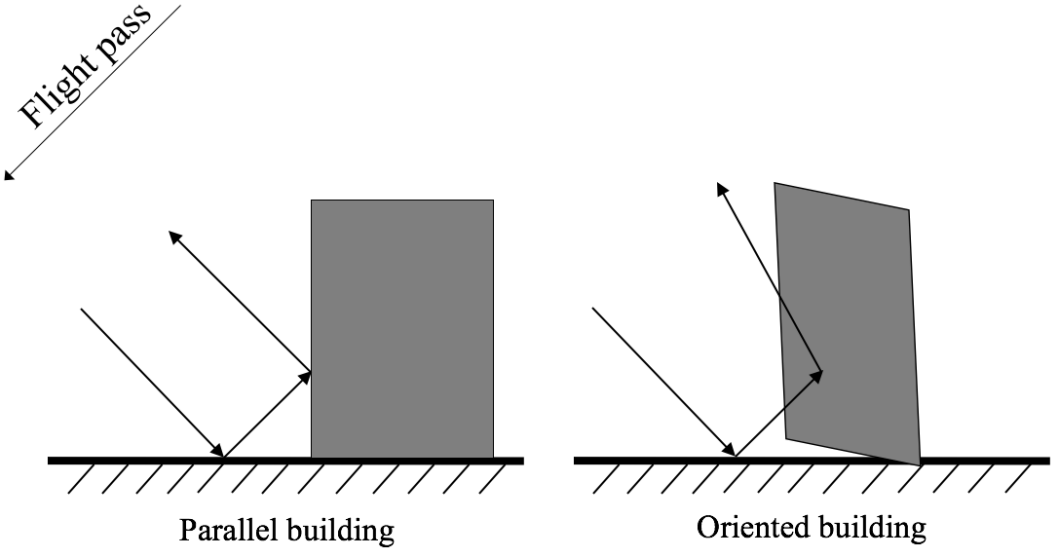

Figure 1.3: Illustration of parallel building and oriented building

1.4 Main research contents

This thesis mainly studied the PolSAR image classification technique and the application of PolSAR dataset for earthquake/tsunami damage assessment.

In Chapter 1, the background and the development information about both the image classification and the damage assessment work is introduced.

Chapter 2 is about the basic theory of Polarimetric SAR. This Chapter introduces

the description matrix of PolSAR data. The polarization target decomposition methods and polarimetric features are mainly introduced.

In Chapter 3, a novel unsupervised classification method is proposed. Sparse representation theory is introduced to create the new energy function, through which both the dictionary and the class labels can be updated. Its optimization work is conducted by the iteration processing. Three air-born PolSAR datasets are tested. The comparison with other supervised and unsupervised algorithms shows its superiority.

Chapter 4 introduces an algorithm to calculate earthquake/tsunami damage level. Both the two PolSAR datasets are used to detect the value change of valid polarimetric features. A novel damage level index which can better describe damage information is proposed. Based on this index, both the damage level map and damage degree map, which can give a good description of the disaster situation are created. Detailed analysis of the Tohoku earthquake and Kumamoto earthquake is presented to verify the effectiveness of this proposed technique.

In Chapter 5, an earthquake/tsunami damage assessment method based on post-event PolSAR data is introduced. It considers the damaged buildings with large orientation angle and classified buildings into four categories. Two polarimetric features are detailedly analyzed to figure out their relationship with different damage conditions. A thresholding method is designed based on these features to extract out all the damaged buildings. This proposed method is unsupervised, and no prior damage information is needed, which can give fast and accurate damage assessment result. The Tohoku earthquake event is analyzed by this method, and the comparison with a supervised method indicates its superiority.

Chapter 6 is about the summery and outlook.

2

Basic Theory for Polarimetric SAR

2.1 Introduction

The working principle of the PolSAR system is to measure scattering echo of the target and to obtain polarimetric matrix for subsequent processing and analysis. By analyzing the data which can describe the target information, such as scattering matrix, a large amount of information about the target object can be obtained, and then the processing work about polarimetric SAR image can be done. Polarimetric SAR system can provide diverse properties of a target by different polarization ways through different transmission and reception modes. It can provide multiple information for the research about target scattering characteristics. Among the obtained target features, polarization features are the most effective and commonly used features which can reflect the scattering mechanism. According to the polarization features, the structural characteristics of the ground object can be detected, so as to further judge the target category or recognize the target.

In this chapter, the basic theory of PolSAR dataset is introduced. The data description forms and the target decomposition theory are mainly introduced.

2.2 Polarization characterization of electromagnetic wave

In the horizontal coordinate system, a completely polarized wave's electric vector $\boldsymbol{E}$ can be decomposed into two directions, namely horizontal direction, and vertical direction. The formula is as follows,

$$\boldsymbol{E} = E_{\mathrm{x}}\widehat{\mathrm{x}} + E_{\mathrm{y}}\widehat{\mathrm{y}} \tag{2.1}$$

where $\widehat{\mathrm{x}}$ and $\widehat{\mathrm{y}}$ is the unit vector in direction of x and y. The relative relation between component E_{x} and E_{y} constitutes plane electromagnetic wave's polarization mode.

The mainly introduced polarization descriptors, which can describe plane electromagnetic waves includes polarization ellipse, Jones vector, and Stokes vector.

2.2.1 Polarization ellipse

Components E_{x} and E_{y} in equation (2.1) can be written as $E_{\mathrm{x}} = E_{0\mathrm{x}}\mathrm{cos}(\omega t - kz + \delta_{\mathrm{x}})$ and $E_{\mathrm{y}} = E_{0\mathrm{y}}\mathrm{cos}(\omega t - kz + \delta_{\mathrm{y}})$, respectively. Thus, this equation can be written as,

$$\boldsymbol{E} = E_0(\mathrm{cos}\gamma \cdot \widehat{\mathrm{x}} + \mathrm{sin}\gamma \cdot e^{j\delta} \cdot \widehat{\mathrm{y}}) \tag{2.2}$$

where $E_0 = (E_{0\mathrm{x}}^2 + E_{0\mathrm{y}}^2)$, $\gamma = \mathrm{arctan}(E_{0\mathrm{y}}/E_{0\mathrm{x}})$, and $\delta = \delta_{\mathrm{y}} - \delta_{\mathrm{x}}$.

When the plane electromagnetic wave propagates along $+z$ axis, its terminal trajectory is a directional ellipse, which can be expressed as the following formula.

$$(\frac{E_{\mathrm{x}}}{E_{0\mathrm{x}}})^2 - 2\frac{E_{\mathrm{x}}}{E_{0\mathrm{x}}}\frac{E_{\mathrm{y}}}{E_{0\mathrm{y}}}\mathrm{cos}\delta + (\frac{E_{\mathrm{y}}}{E_{0\mathrm{y}}})^2 = \mathrm{sin}^2\delta \tag{2.3}$$

When $E_{0\mathrm{x}} \neq 0$, $E_{0\mathrm{y}} \neq 0$, $\delta \neq 0$, and the intermediate variable γ is divided out, equation 2.2 is changed as equation 2.3.

The elliptic curve is shown in Figure 2.1, and the polarized ellipse can be expressed by three parameters.

A is the amplitude of the ellipse, which is defined as,

$$A = \sqrt{E_{0\mathrm{x}}^2 + E_{0\mathrm{y}}^2} \tag{2.4}$$

$\phi \in [-\frac{\pi}{2}, \frac{\pi}{2}]$ represents the direction of the ellipse,

$$\mathrm{tan}\ 2\phi = 2\frac{E_{0\mathrm{x}}E_{0\mathrm{y}}}{E_{0\mathrm{x}}^2 - E_{0\mathrm{y}}^2}\mathrm{cos}\delta \ \text{ with } \ \delta = \delta_{\mathrm{y}} - \delta_{\mathrm{x}} \tag{2.5}$$

$|\tau| \in [0, \frac{\pi}{4}]$ is ellipticity, which is defined as,

$$|\mathrm{sin}\ \tau| = 2\frac{E_{0\mathrm{x}}E_{0\mathrm{y}}}{E_{0\mathrm{x}}^2 - E_{0\mathrm{y}}^2}|\mathrm{sin}\ \delta| \tag{2.6}$$

When the two directional components in the polarization ellipse formula satisfy that

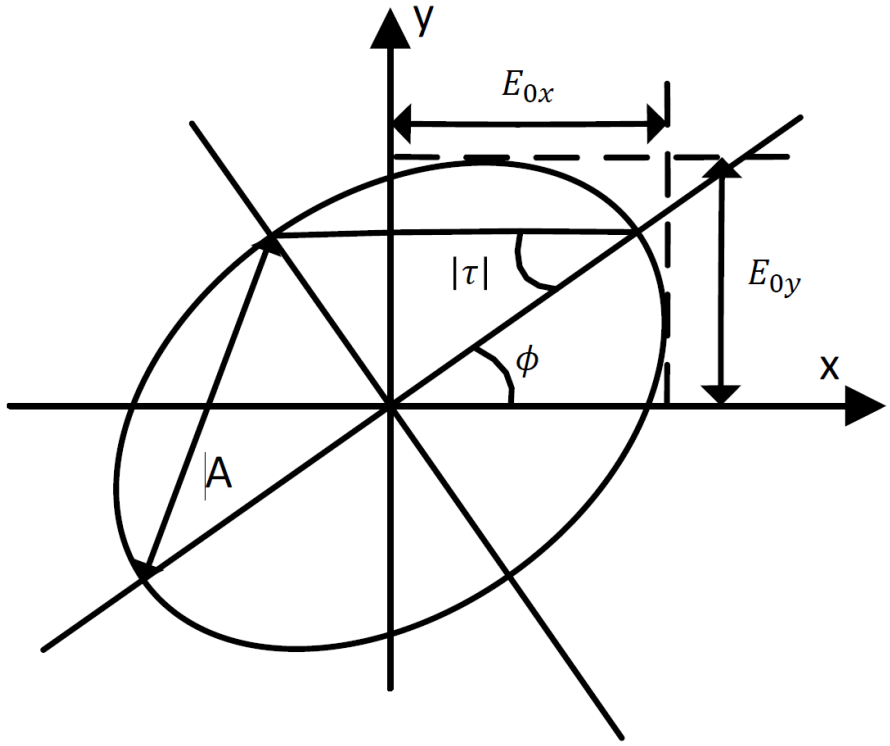

Figure 2.1: Schematic diagram of polarization ellipse

$E_{0\mathrm{x}} = E_{0\mathrm{y}}$, and $\delta = \delta_{\mathrm{y}} - \delta_{\mathrm{x}} = \pm\frac{\pi}{2} + k\pi$, this polarization state is circular polarization. When $\delta = -\frac{\pi}{2} + k\pi$, it is the right-handed circular polarization. When $\delta = \frac{\pi}{2} + k\pi$, it is left-handed polarization. When $\delta = \delta_{\mathrm{y}} - \delta_{\mathrm{x}} = 0$, it is linear polarization.

2.2.2 Jones vector

The Jones vector is used to express the plane monochromatic electric field, it is to describe the polarized wave with the least amount of information [57, 58]. The complex field vector $\overrightarrow{\boldsymbol{E}}(z,t)$ is,

$$\begin{aligned}\overrightarrow{\boldsymbol{E}}(z,t) &= \begin{bmatrix} E_{0\mathrm{x}}\cos(\omega t - kz + \delta_{\mathrm{x}}) \\ E_{0\mathrm{y}}\cos(\omega t - kz + \delta_{\mathrm{y}}) \end{bmatrix} \\ &= \mathrm{Re}\left\{ \begin{bmatrix} E_{0\mathrm{x}}e^{j\delta_{\mathrm{x}}} \\ E_{0\mathrm{y}}e^{j\delta_{\mathrm{y}}} \end{bmatrix} e^{-jkz}e^{j\omega t} \right\} = \mathrm{Re}\{\overrightarrow{\underline{\boldsymbol{E}}}(z)e^{j\omega t}\}\end{aligned} \tag{2.7}$$

Jones vector $\underline{\boldsymbol{E}}$ can be seen as $\overrightarrow{\underline{\boldsymbol{E}}}(z)$ that only consider about the cross section at

$z = 0$,

$$\underline{\boldsymbol{E}} = \overrightarrow{\underline{\boldsymbol{E}}}(0) = \begin{bmatrix} E_{0\mathrm{x}} e^{j\delta_{\mathrm{x}}} \\ E_{0\mathrm{y}} e^{j\delta_{\mathrm{y}}} \end{bmatrix} \tag{2.8}$$

Jones vector can be used to represent the polarization state, it is defined through polarized ellipsoid,

$$\underline{\boldsymbol{E}} = Ae^{+j\alpha} \begin{bmatrix} \cos\phi \cos\tau - j\sin\phi \sin\tau \\ \sin\phi \cos\tau - j\cos\phi \sin\tau \end{bmatrix} \tag{2.9}$$

where α is relative phase term. It can also be represented as,

$$\underline{\boldsymbol{E}} = Ae^{+j\alpha} \begin{bmatrix} \cos\phi & -\sin\phi \\ \sin\phi & \cos\phi \end{bmatrix} \begin{bmatrix} \cos\tau \\ j\sin\tau \end{bmatrix} \tag{2.10}$$

2.2.3 Stokes vector

According to the last section, the Jones vector is defined by amplitude and phase, it can only be acquired by coherent radar systems. This kind of coherent radar system has only been used in recent years. Previously, only incoherent radar systems were available. Since the incoherent radar system can only measure the significant power parameters of the incident wave, it is necessary to use only power measurement to present the characterization of wave's polarization state, which is Stokes vector [59].

Stokes vector is defined as follows (for fully polarized waves),

$$\underline{\boldsymbol{g}}_{\underline{E}} = \begin{bmatrix} g_0 \\ g_1 \\ g_2 \\ g_3 \end{bmatrix} = \begin{bmatrix} E_{0\mathrm{x}}^2 + E_{0\mathrm{y}}^2 \\ E_{0\mathrm{x}}^2 - E_{0\mathrm{y}}^2 \\ 2E_{0\mathrm{x}}E_{0\mathrm{y}}\cos\delta \\ 2E_{0\mathrm{x}}E_{0\mathrm{y}}\sin\delta \end{bmatrix} \tag{2.11}$$

The Stokes vector is defined as, (for non-completely polarized waves),

$$\underline{\boldsymbol{g}}_{\underline{E}} = \begin{bmatrix} g_0 \\ g_1 \\ g_2 \\ g_3 \end{bmatrix} = \begin{bmatrix} |E_{\mathrm{x}}|^2 + |E_{\mathrm{y}}|^2 \\ |E_{\mathrm{x}}|^2 - |E_{\mathrm{y}}|^2 \\ 2\mathrm{Re}(E_{\mathrm{x}}E_{\mathrm{y}}^*) \\ -2\mathrm{Im}(E_{\mathrm{x}}E_{\mathrm{y}}^*) \end{bmatrix} \tag{2.12}$$

Stokes parameters g_0, g_1, g_2, and g_3 in the above equations represent different intensity of electromagnetic wave respectively. g_0 is the sum of the horizontal and vertical strength, g_1 is the difference of strength in two directions, g_2 is the strength of linear polarization when elliptical azimuth equals to $45°$ or $135°$, and g_3 is the intensity of circular polarization. For fully polarized and non-fully polarized waves, stokes parameters satisfy that $g_0^2 = g_1^2 + g_2^2 + g_3^2$ and $g_0^2 > g_1^2 + g_2^2 + g_3^2$, respectively.

Stokes vector can also be represented by polarization ellipse parameters,

$$\underline{\boldsymbol{g}}_{\underline{E}} = \begin{bmatrix} g_0 \\ g_1 \\ g_2 \\ g_3 \end{bmatrix} = \begin{bmatrix} E_{0\mathrm{x}}^2 + E_{0\mathrm{y}}^2 \\ E_{0\mathrm{x}}^2 - E_{0\mathrm{y}}^2 \\ 2E_{0\mathrm{x}}E_{0\mathrm{y}}\cos\,\delta \\ 2E_{0\mathrm{x}}E_{0\mathrm{y}}\sin\,\delta \end{bmatrix} = \begin{bmatrix} A^2 \\ A^2\cos(2\phi)\cos(2\tau) \\ A^2\sin(2\phi)\cos(2\tau) \\ A^2\sin(2\tau) \end{bmatrix} \tag{2.13}$$

The transmitting wave in polarized SAR system can be approximated as a completely polarized wave, but because the received electromagnetic wave is complex, it is a partially polarized wave. Thus, stokes vectors are often introduced to present scattered wave.

2.3 Description methods for PolSAR data

Targets' detailed information can be obtained through analyzing the scattering characteristic description matrix obtained by PolSAR system. In this section, the introduced polarization scattering characteristic description matrix include scattering matrix, coherence matrix, covariance matrix, and Muller matrix.

2.3.1 Scattering matrix

When the electromagnetic wave propagates to the target surface and interacts with it, the energy of the incident wave will be absorbed by the target and radiated again. The characteristics of the scattered wave will change compared with that of the incident wave. The polarization scattering matrix is a description matrix used to characterize the relationship between the scattering wave and incident wave.

Polarization scattering matrix [**S**] is defined as,

$$\boldsymbol{E}^r = [\mathbf{S}]\boldsymbol{E}^t = \begin{bmatrix} E_{\mathrm{H}}^r \\ E_{\mathrm{V}}^r \end{bmatrix} = \frac{e^{jk_0 r}}{kr} \begin{bmatrix} S_{\mathrm{HH}} & S_{\mathrm{HV}} \\ S_{\mathrm{VH}} & S_{\mathrm{VV}} \end{bmatrix} \begin{bmatrix} E_{\mathrm{H}}^t \\ E_{\mathrm{V}}^t \end{bmatrix} \tag{2.14}$$

where $\boldsymbol{E}^r$ represents scattering wave, $\boldsymbol{E}^t$ represents incident wave, v and h represent the basis of orthogonal vertical and horizontal polarization. S_{HH} and S_{VV} are co-polarization components, S_{HV} and S_{VH} are cross polarization components. If the receiving and transmitting antennas are interchanged, the backscattering matrix is symmetric according to the reciprocity theorem, $S_{\mathrm{HH}} = S_{\mathrm{VH}}$ [60, 61].

The scattering matrix **S** that used to describe a given target can be written as,

$$\mathbf{S} = \begin{bmatrix} |S_{11}e^{j\phi_{11}}| & |S_{12}e^{j\phi_{12}}| \\ |S_{21}e^{j\phi_{21}}| & |S_{22}e^{j\phi_{22}}| \end{bmatrix} \tag{2.15}$$

The total power of the polarizing radar system is calculated as follows,

$$\mathrm{SPAN} = Tr(\mathbf{S}\mathbf{S}^{*T}) = |S_{11}|^2 + |S_{12}|^2 + |S_{21}|^2 + |S_{22}|^2 \tag{2.16}$$

where $\mathrm{Tr}(A)$ represents the trace of matrix A. In backscattering system, according to the reciprocity theorem, the total power can be expressed as,

$$\mathrm{SPAN} = \mathrm{Tr}(\mathbf{S}\mathbf{S}^{*T}) = |S_{11}|^2 + 2|S_{12}|^2 + |S_{22}|^2 \tag{2.17}$$

2.3.2 Mueller matrix

The Mueller matrix is introduced to express the relationship between the scattering wave's Stokes vector and incident wave. Unlike the scattering matrix, which is suit-

able for fully polarized waves, the Stokes vector is used to describe both incompletely polarized and completely non-polarized waves.

The Mueller matrix is defined as,

$$\boldsymbol{J}_s = [\mathbf{M}]\boldsymbol{J}_t \tag{2.18}$$

where $\boldsymbol{J}_t$ and $\boldsymbol{J}_s$ represent the incident electromagnetic wave and scattering electromagnetic wave, respectively, $\mathbf{M}$ is Mueller matrix.

$$[\mathbf{M}] = [\mathbf{R}][\mathbf{W}][\mathbf{R}]^{-1} \tag{2.19}$$

where,

$$[\mathbf{R}] = \begin{bmatrix} 1 & 0 & 0 & 1 \\ 1 & 0 & 0 & -1 \\ 0 & 1 & 1 & 0 \\ 0 & j & -j & 0 \end{bmatrix} \tag{2.20}$$

$$[\mathbf{W}] = \langle [\mathbf{S}] \otimes [\mathbf{S}]^* \rangle = \left\langle \begin{bmatrix} S_{\mathrm{HH}}S_{\mathrm{HH}}^* & S_{\mathrm{HH}}S_{\mathrm{HV}}^* & S_{\mathrm{HV}}S_{\mathrm{HH}}^* & S_{\mathrm{HV}}S_{\mathrm{HV}}^* \\ S_{\mathrm{HH}}S_{\mathrm{VH}}^* & S_{\mathrm{HH}}S_{\mathrm{VV}}^* & S_{\mathrm{HV}}S_{\mathrm{VH}}^* & S_{\mathrm{HV}}S_{\mathrm{VV}}^* \\ S_{\mathrm{VH}}S_{\mathrm{HH}}^* & S_{\mathrm{VH}}S_{\mathrm{HV}}^* & S_{\mathrm{VV}}S_{\mathrm{HH}}^* & S_{\mathrm{VV}}S_{\mathrm{HV}}^* \\ S_{\mathrm{VH}}S_{\mathrm{VH}}^* & S_{\mathrm{VH}}S_{\mathrm{VV}}^* & S_{\mathrm{VV}}S_{\mathrm{VH}}^* & S_{\mathrm{VV}}S_{\mathrm{VV}}^* \end{bmatrix} \right\rangle \tag{2.21}$$

the above equation shows that the intermediate matrix $[\mathbf{W}]$ can be transformed to get the Mueller matrix, they're equivalent. The intermediate matrix $[\mathbf{W}]$ is obtained by losing the absolute phase information through the scattering matrix $[\mathbf{S}]$. It can be known that the Mueller matrix corresponds to the scattering matrix $[\mathbf{S}]$, which are equivalent in describing the polarization scattering characteristics of the target.

2.3.3 Polarimetric coherence matrix T and covariance matrix C

In practical remote sensing applications, not all radar targets are stable and fixed. In general, the target is distributed in a dynamic environment and subject to changes in space and time. Even though the environment is dynamic, we can make assumptions about

stability, homogeneity, ergodicity. The target can be represented by the second-order fluctuations extracted from polarization covariance matrix and polarization coherence matrix [62–64].

The vectorization of polarization scattering matrix **S** is expressed as,

$$[\mathbf{S}] = \begin{bmatrix} S_{\mathrm{HH}} & S_{\mathrm{HV}} \\ S_{\mathrm{VH}} & S_{\mathrm{VV}} \end{bmatrix} \rightarrow \overrightarrow{\boldsymbol{k}}_4 = \frac{1}{2}\mathrm{Tr}([\mathbf{S}][\psi]) = [k_0, k_1, k_2, k_3]^T \tag{2.22}$$

where T represents transpose of matrix, $[\psi]$ is the 2×2 complex matrix set. In this section, two kinds of completely orthogonal basis sets are introduced for vectorization of the scattering matrix

The first complete orthogonal basis set is shown as

$$[\psi_{\mathrm{B}}] = \left\{ 2\begin{bmatrix} 1 & 0 \\ 0 & 0 \end{bmatrix}, 2\begin{bmatrix} 0 & 1 \\ 0 & 0 \end{bmatrix}, 2\begin{bmatrix} 0 & 0 \\ 1 & 0 \end{bmatrix}, 2\begin{bmatrix} 0 & 0 \\ 0 & 1 \end{bmatrix} \right\} \tag{2.23}$$

The corresponding scattering vector is

$$\overrightarrow{\boldsymbol{k}}_{4\mathrm{B}} = [S_{\mathrm{HH}} \;\; S_{\mathrm{HV}} \;\; S_{\mathrm{VH}} \;\; S_{\mathrm{VV}}]^T \tag{2.24}$$

The scattering vector can be expressed as the following formula,

$$\overrightarrow{\boldsymbol{k}}_{3\mathrm{B}} = [S_{\mathrm{HH}} \;\; \sqrt{2}S_{\mathrm{HV}} \;\; S_{\mathrm{VV}}]^T \tag{2.25}$$

The second completely orthogonal basis is shown as the following formula, it is the basis set of Pauli matrix.

$$[\psi_{\mathrm{P}}] = \left\{ \sqrt{2}\begin{bmatrix} 1 & 0 \\ 0 & 1 \end{bmatrix}, \sqrt{2}\begin{bmatrix} 1 & 0 \\ 0 & -1 \end{bmatrix}, \sqrt{2}\begin{bmatrix} 0 & 1 \\ 1 & 0 \end{bmatrix}, \sqrt{2}\begin{bmatrix} 0 & -j \\ j & 0 \end{bmatrix} \right\} \tag{2.26}$$

The corresponding Pauli scattering vector is shown as,

$$\overrightarrow{\boldsymbol{k}}_{4\mathrm{P}} = \frac{1}{\sqrt{2}}[S_{\mathrm{HH}} + S_{\mathrm{VV}} \;\; S_{\mathrm{HH}} - S_{\mathrm{VV}} \;\; S_{\mathrm{HV}} + S_{\mathrm{VH}} \;\; j(S_{\mathrm{VH}} - S_{\mathrm{HV}})]^T \tag{2.27}$$

In the case of reciprocity theorem, the three-dimensional vector is,

$$\overrightarrow{\boldsymbol{k}}_{3\mathrm{P}} = \frac{1}{\sqrt{2}}[S_{\mathrm{HH}} + S_{\mathrm{VV}} \;\; S_{\mathrm{HH}} - S_{\mathrm{VV}} \;\; 2S_{\mathrm{HV}}]^T \tag{2.28}$$

The polarization covariance matrix obtained from the scattering vector $\overrightarrow{\boldsymbol{k}}_{3\mathrm{B}}$ is,

$$[\mathbf{C}] = \langle \overrightarrow{\boldsymbol{k}}_{3\mathrm{B}} \overrightarrow{\boldsymbol{k}}_{3\mathrm{B}}^{*T} \rangle = \begin{bmatrix} |S_{\mathrm{HH}}|^2 & \sqrt{2}S_{\mathrm{HH}}S_{\mathrm{HV}}^* & S_{\mathrm{HH}}S_{\mathrm{VV}}^* \\ \sqrt{2}S_{\mathrm{HV}}S_{\mathrm{HH}}^* & 2|S_{\mathrm{HV}}|^2 & \sqrt{2}S_{\mathrm{HV}}S_{\mathrm{VV}}^* \\ S_{\mathrm{VV}}S_{\mathrm{HH}}^* & \sqrt{2}S_{\mathrm{VV}}S_{\mathrm{HV}}^* & |S_{\mathrm{VV}}|^2 \end{bmatrix} \tag{2.29}$$

The polarization coherence matrix $[\mathbf{T}]$ obtained from the Pauli scattering vector $\overrightarrow{\boldsymbol{k}}_{3\mathrm{P}}$ is shown as,

$$\begin{aligned} [\mathbf{T}] &= \langle \overrightarrow{\boldsymbol{k}}_{3\mathrm{P}} \overrightarrow{\boldsymbol{k}}_{3\mathrm{P}}^{*T} \rangle \\ &= \frac{1}{2} \begin{bmatrix} |S_{\mathrm{HH}} + S_{\mathrm{VV}}|^2 & (S_{\mathrm{HH}} + S_{\mathrm{VV}})(S_{\mathrm{HH}} - S_{\mathrm{VV}})^* & 2(S_{\mathrm{HH}} + S_{\mathrm{VV}})S_{\mathrm{HV}}^* \\ (S_{\mathrm{HH}} - S_{\mathrm{VV}})(S_{\mathrm{HH}} + S_{\mathrm{VV}})^* & |S_{\mathrm{HH}} - S_{\mathrm{VV}}|^2 & 2(S_{\mathrm{HH}} - S_{\mathrm{VV}})S_{\mathrm{HV}}^* \\ 2S_{\mathrm{HV}}(S_{\mathrm{HH}} + S_{\mathrm{VV}})^* & 2S_{\mathrm{HV}}(S_{\mathrm{HH}} - S_{\mathrm{VV}})^* & 4|S_{\mathrm{HV}}|^2 \end{bmatrix} \end{aligned} \tag{2.30}$$

$[\mathbf{T}]$ can be changed into the polarization covariance matrix by the formula,

$$[\mathbf{T}] = [\mathbf{A}][\mathbf{C}][\mathbf{A}]^{-1} \tag{2.31}$$

where,

$$[\mathbf{A}] = \frac{1}{\sqrt{2}} \begin{bmatrix} 1 & 0 & 1 \\ 1 & 0 & -1 \\ 0 & \sqrt{2} & 0 \end{bmatrix} \tag{2.32}$$

2.4 Polarization target decomposition theory

By further processing and analysis of PolSAR data, targets' scattering mechanism can be better reflected by expressing it in a way which can better reflect the scattering characteristics of the target. Target decomposition theory is developed to better express the polarization information of the target. Polarization feature obtained through target decomposition can provide important information for further image processing. According

to different decomposition subjects, the method can be classified into two categories: incoherent target decomposition and coherent target decomposition. In this section, a partial target decomposition method is selected, and its scattering mechanism and solution method are introduced in detail.

2.4.1 Coherent target decomposition

Pauli decomposition

Pauli decomposition is to express $[\mathbf{S}]$ using four physical scattering mechanisms, and it is defined as,

$$[\mathbf{S}] = \begin{bmatrix} S_{\mathrm{HH}} & S_{\mathrm{HV}} \\ S_{\mathrm{VH}} & S_{\mathrm{VV}} \end{bmatrix} = a[\mathbf{S}_a] + b[\mathbf{S}_b] + c[\mathbf{S}_c] + d[\mathbf{S}_d] \tag{2.33}$$

where $[\mathbf{S}_a]$, $[\mathbf{S}_b]$, $[\mathbf{S}_c]$, and $[\mathbf{S}_d]$ represent four kinds of physical scattering mechanisms. $[\mathbf{S}_a]$ is odd scattering, it is used to represent flat surface, sphere, etc. $[\mathbf{S}_b]$ and $[\mathbf{S}_c]$ are all double-bounce scattering mechanisms, they represent the double-bounce scattering that revolve around an axis 0° and 45°, respectively. $[\mathbf{S}_d]$ represents the antisymmetric component, its weight is usually set as 0.

These four scattering mechanisms are defined as,

$$\begin{aligned} [\mathbf{S}_a] &= \frac{1}{\sqrt{2}} \begin{bmatrix} 1 & 0 \\ 0 & 1 \end{bmatrix} \\ [\mathbf{S}_b] &= \frac{1}{\sqrt{2}} \begin{bmatrix} 1 & 0 \\ 0 & -1 \end{bmatrix} \\ [\mathbf{S}_c] &= \frac{1}{\sqrt{2}} \begin{bmatrix} 0 & 1 \\ 1 & 0 \end{bmatrix} \\ [\mathbf{S}_d] &= \frac{1}{\sqrt{2}} \begin{bmatrix} 0 & -i \\ i & 0 \end{bmatrix} \end{aligned} \tag{2.34}$$

Equation 2.33 can be written as,

$$\begin{aligned}\boldsymbol{K} &= [a \;\; b \;\; c \;\; d] \\ &= \frac{1}{\sqrt{2}}(S_{\text{HH}} + S_{\text{VV}} \quad S_{\text{HH}} - S_{\text{VV}} \quad S_{\text{HV}} + S_{\text{VH}} \quad i(S_{\text{VH}} - S_{\text{HV}}))^T\end{aligned} \tag{2.35}$$

If the reciprocity theorem is satisfied, the above formula can be rewritten as

$$\begin{aligned}\boldsymbol{K} &= [a \;\; b \;\; c \;\; d] \\ &= \frac{1}{\sqrt{2}}(S_{\text{HH}} + S_{\text{VV}} \quad S_{\text{HH}} - S_{\text{VV}} \quad 2S_{\text{HV}})^T\end{aligned} \tag{2.36}$$

Pauli decomposition keeps the total power constant,

$$\text{SPAN} = |S_{\text{HH}}|^2 + |S_{\text{HV}}|^2 + |S_{\text{VH}}|^2 + |S_{\text{VV}}|^2 = |a|^2 + |b|^2 + |c|^2 + |d|^2 \tag{2.37}$$

The parameters a, b, c in Pauli decomposition can be used to compose the pseudo-color image, which can provide visual information. The relationship between these three parameters and the three channels in RGB color space is shows as,

$$|a|^2 \;\rightarrow\; \text{Blue}, \quad |b|^2 \;\rightarrow\; \text{Red}, \quad |c|^2 \;\rightarrow\; \text{Green} \tag{2.38}$$

Krogager decomposition

For Krogager decomposition [65], the scattering matrix is decomposed as three mechanisms: surface, dihedral, and helix scattering. The Krogager decomposition basis is defined as,

$$[\psi_{\text{K}}] = e^{j\varphi}\left\{ e^{j\varphi_s}\begin{bmatrix} 0 & j \\ j & 0 \end{bmatrix}, \begin{bmatrix} e^{j2\theta} & 0 \\ 0 & -e^{-j2\theta} \end{bmatrix}, \begin{bmatrix} e^{j2\theta} & 0 \\ 0 & 0 \end{bmatrix}\right\} \tag{2.39}$$

The expression formula for the scattering matrix using the above Krogager decomposition basis is shown as,

$$[\mathbf{S}] = e^{j\varphi}\left\{ e^{j\varphi_s}\cdot K_{\text{s}}\begin{bmatrix} 0 & j \\ j & 0 \end{bmatrix} + K_{\text{d}}\begin{bmatrix} e^{j2\theta} & 0 \\ 0 & -e^{-j2\theta} \end{bmatrix} + K_{\text{h}}\begin{bmatrix} e^{j2\theta} & 0 \\ 0 & 0 \end{bmatrix}\right\} \tag{2.40}$$

where K_{s}, K_{d}, and K_{h} mean the surface, double-bounce, and helix scattering component

coefficient, respectively. θ is the azimuth angle of helix scattering and double-bounce scattering component. K_{s}, K_{d}, and K_{h} are calculated by the equations,

$$K_{\mathrm{s}} = |S_{\mathrm{HV}}| \tag{2.41}$$

When $|S_{\mathrm{HH}}| > |S_{\mathrm{VV}}|$, the double-bounce scattering coefficient K_d^+ and the left-handed helix scattering coefficient K_h^+ can be expressed as,

$$\begin{aligned} K_{\mathrm{d}}^+ &= |S_{\mathrm{VV}}| \\ K_{\mathrm{h}}^+ &= |S_{\mathrm{HH}}| - |S_{\mathrm{VV}}| \end{aligned} \tag{2.42}$$

When $|S_{\mathrm{HH}}| < |S_{\mathrm{VV}}|$, the double-bounce scattering coefficient K_{d}^- and the left-handed helix scattering coefficient K_{h}^- can be expressed as,

$$\begin{aligned} K_{\mathrm{d}}^- &= |S_{\mathrm{HH}}| \\ K_{\mathrm{h}}^- &= |S_{\mathrm{HH}}| - |S_{\mathrm{VV}}| \end{aligned} \tag{2.43}$$

The three parameters from Krogager decomposition can be also used to compose pseudo-color image,

$$|K_{\mathrm{s}}|^2 \rightarrow \text{Blue}, \quad |K_{\mathrm{d}}|^2 \rightarrow \text{Red}, \quad |K_{\mathrm{h}}|^2 \rightarrow \text{Green} \tag{2.44}$$

2.4.2 Incoherent target decomposition

Cloude-Pottier Decomposition

Cloude-Pottier Decomposition [66] contains all the scattering mechanisms. By extracting the eigenvalues of polarization coherence matrix, the scattering entropy and angle are calculated. Compared with other methods, Cloude-Pottier decomposition is stable.

Cloude-Pottier decomposition is a further analysis of polarization coherence matrix, the non-negative eigenvalues can be calculated through the eigenvalue decomposition of $\langle \mathbf{T} \rangle$.

$$\langle \mathbf{T} \rangle = \mathbf{U}_3 \begin{bmatrix} \lambda_1 & 0 & 0 \\ 0 & \lambda_2 & 0 \\ 0 & 0 & \lambda_3 \end{bmatrix} \mathbf{U}_3^* \tag{2.45}$$

where $\langle \cdot \rangle$ means average calculation. The non-negative eigenvalues of coherence matrix satisfy that $\lambda_1 > \lambda_2 > \lambda_3 \geq 0$. Column vectors of matrix U_3 are corresponding eigenvectors. The obtained non-negative eigenvalues can be applied to calculate scattering entropy H, anisotropy parameter A, and scattering angle $\bar{\alpha}$.

$$H = -\sum_{i=1}^{3} p_i \log_3 p_i \tag{2.46}$$

$$\bar{\alpha} = \sum_{i=1}^{3} p_i \alpha_i \tag{2.47}$$

$$A = \frac{\lambda_2 - \lambda_3}{\lambda_2 + \lambda_3} \tag{2.48}$$

where

$$p_i = \frac{\lambda_i}{\sum_{n=1}^{3} \lambda_n}, i = 1, 2, 3 \tag{2.49}$$

Cloud-Pottier decomposition contains all the scattering mechanisms. Scattering entropy H represents the polarization degree of the target. The scattering angle α represents the physical mechanism of the target. Anisotropy parameter A characterizes the distribution of eigenvalues.

Freeman Decomposition

Freeman decomposition [67] is an incoherent decomposition method based on the ternary scattering mechanism model without using any real information of ground objects to express the polarization characteristics. Freeman decomposition is a further analysis of the covariance matrix, which is divided into three mechanisms: volume, even, and surface scattering. The expression formula is as follows,

$$\mathbf{C} = f_{\mathrm{s}}[\mathbf{C}_{\mathrm{s}}] + f_{\mathrm{d}}[\mathbf{C}_{\mathrm{d}}] + f_{\mathrm{v}}[\mathbf{C}_{\mathrm{v}}] \tag{2.50}$$

Among the three scattering mechanisms in Freeman decomposition, volume scattering, even scattering, and surface scattering represents vegetation areas, urban areas, and rough natural surface, respectively. This target decomposition method is used to describe the natural backscattering, which can effectively distinguish the submerged forest and the unsubmerged forest, vegetation area and non-vegetation area, and can estimate the forest flood and its interference to the full polarization radar signal.

It is assumed that the scatterer satisfies the reflection symmetry and the reciprocity theorem, and the three scattering mechanisms are not related to each other, a comprehensive backscattering model can be obtained,

$$\begin{aligned}
\langle|S_{\mathrm{HH}}|^2\rangle &= f_{\mathrm{s}}|\beta|^2 + f_{\mathrm{d}}|\alpha|^2 + f_{\mathrm{v}} \\
\langle|S_{\mathrm{VV}}|^2\rangle &= f_{\mathrm{s}} + f_{\mathrm{d}} + f_{\mathrm{v}} \\
\langle S_{\mathrm{HH}} S_{\mathrm{VV}}^*\rangle &= f_{\mathrm{s}}\beta + f_{\mathrm{d}}\alpha + f_{\mathrm{v}}/3 \\
\langle|S_{\mathrm{HV}}|^2\rangle &= f_{\mathrm{v}}/3
\end{aligned} \tag{2.51}$$

where f_v represents the contribution of volume scattering to covariance matrix, its scattering power is,

$$P_{\mathrm{v}} = \frac{8 f_{\mathrm{v}}}{3} \tag{2.52}$$

The scattering power of even scattering component is,

$$P_{\mathrm{d}} = f_{\mathrm{d}}(1 + |\alpha|^2) \tag{2.53}$$

The scattering power of surface scattering component is,

$$P_{\mathrm{s}} = f_{\mathrm{s}}(1 + |\beta|^2) \tag{2.54}$$

Freeman decomposition keeps the total power constant, it is shown as,

$$\mathrm{SPAN} = |S_{\mathrm{HH}}|^2 + 2|S_{\mathrm{HV}}|^2 + |S_{\mathrm{VV}}|^2 = P_{\mathrm{v}} + P_{\mathrm{d}} + P_{\mathrm{s}} \tag{2.55}$$

The three components from Freeman decomposition can also be mapped to RGB space to compose pseudo-color images.

$$P_{\mathrm{s}} \rightarrow \text{Blue}, \quad P_{\mathrm{d}} \rightarrow \text{Red}, \quad P_{\mathrm{v}} \rightarrow \text{Green} \tag{2.56}$$

Yamaguchi Four-component Decomposition

The Yamaguchi Decomposition [15] was proposed based on the Freeman decomposition. It introduced the helix scattering component, which can effectively describe urban topography. The double-bounce, surface, helix, and volume scattering power calculated by this method are defined as,

$$\begin{aligned} P_{\mathrm{d}} &= f_{\mathrm{d}}(1+|\alpha|^2) \\ P_{\mathrm{s}} &= f_{\mathrm{s}}(1+|\beta|^2) \\ P_{\mathrm{v}} &= f_{\mathrm{v}} \\ P_{\mathrm{h}} &= f_{\mathrm{h}} \end{aligned} \tag{2.57}$$

where f_{d}, f_{s}, f_{v}, and f_{h} are these scattering models' contributions in coherency matrix.

The total power is constant,

$$\text{SPAN} = |S_{\mathrm{HH}}|^2 + 2|S_{\mathrm{HV}}|^2 + |S_{\mathrm{VV}}|^2 = P_{\mathrm{v}} + P_{\mathrm{d}} + P_{\mathrm{s}} + P_{\mathrm{h}} \tag{2.58}$$

The components of the Yamaguchi decomposition can be used to compose color images, it is by inputting P_s, P_d, P_v into the R, G, B channels,

$$P_{\mathrm{s}} \rightarrow \text{Blue}, \quad P_{\mathrm{d}} \rightarrow \text{Red}, \quad P_{\mathrm{v}} \rightarrow \text{Green} \tag{2.59}$$

Neumann two-component decomposition

The Neumann two-component decomposition [68] is a model for polarimetric coherency and covariance matrix elements, which aims to represent vegetation characteristics.

The average particle backscattering matrix in the eigenpolarization basis is defined as,

$$E\{\mathbf{S}\} = \begin{bmatrix} a & 0 \\ 0 & b \end{bmatrix} = \frac{a+b}{2} \begin{bmatrix} 1+\delta^* & 0 \\ 0 & 1-\delta^* \end{bmatrix} \tag{2.60}$$

where $E\{\cdot\}$ means expectation value operation, $*$ represents complex conjugate operator. δ is the particle anisotropy, it indicates an average particle's scattering properties, it is defined as,

$$\delta = (\frac{a-b}{a+b})^* \tag{2.61}$$

The orientations of a large number of scatterers are distributed following circular normal distribution,

$$p_\psi(\psi|\tilde{\psi},\kappa) = \frac{e^{\kappa\cos(2(\psi-\tilde{\psi}))}}{\pi I_0(\kappa)}, \;\; \kappa \in [0,\infty] \tag{2.62}$$

where ψ represents the particle orientation angle, κ means the degree of concentration, $\tilde{\psi} \in [-\frac{\pi}{2}, \frac{\pi}{2}]$ means the average orientation angle, and $I_0(\kappa)$ means the modified Bessel function. τ is the normalized degree of orientation randomness, it is defined as,

$$\tau = I_0(\kappa)e^{-\kappa}, \;\; \tau \in [0,1] \tag{2.63}$$

2.5 Another polarimetric feature: circular correlation coefficient

Correlation coefficient at circular polarization basis ρ_{RRLL} [54] can be used to extract man-made structure [69]. For the damaged buildings extraction work, it is an effective parameter. For damaged buildings, helicity and surface roughness increase, it makes their ρ_{RRLL} value smaller than the values of undamaged ones. For that reason, ρ_{RRLL} acts as a suitable damage detection index.

ρ_{RRLL} is defined as,

$$\rho_{\text{RRLL}} = \frac{\langle S_{\text{RR}} S_{\text{LL}}^* \rangle}{\sqrt{S_{\text{RR}} S_{\text{RR}}^*}\sqrt{S_{\text{LL}} S_{\text{LL}}^*}} \tag{2.64}$$

where R means right hand circular polarization and L means left hand circular polarization.

2.6 Conclusion

The basic theory about PolSAR data is introduced in this Section. Theory of polarization is briefly introduced, and commonly used polarimetric SAR data description forms, such as scattering matrix, are introduced in detail. At the same time, the target decomposition methods which can better describe scattering characteristics of targets are introduced emphatically. Several typical polarization decomposition methods, including Pauli decomposition, Krogager decomposition, etc. are introduced in detail. At the last of this section, the polarimetric feature, correlation coefficient, is detailedly introduced. The polarimetric features extracted from the introduced target decomposition methods and the correlation coefficient are the mainly used parameters for both the following image classification processing and the disaster monitoring work.

3

Sparse Representation based PolSAR Image Classification

3.1 Introduction

An unsupervised classification method for PolSAR image is introduced in this chapter. Sparse representation theory is employed, for which an effective dictionary that used to represent test dataset is sufficient. Dictionary can be composed by pixels which have corresponding ground-truth information. Also, various dictionary updating methods [70, 71] can be applied to the initial dictionary, which is set randomly. This kind of method still needs ground-truth information for dictionary updating processing. Thus, both of these two methods are supervised. The algorithm proposed here is unsupervised. Dictionary and the output, class labels are two variables which need to be updated. A preliminary classification result is needed to create the initial values. Thus, the H/α/A Wishart classification algorithm is employed. An energy function is designed to implement the updating processing. The energy function is alternately minimized, and these variables can be calculated. Experiments are designed and conducted on three images. They verified the superiority of this algorithm.

3.2 Methodology

Figure 3.1 shows this algorithm's flowchart. The conducted preprocessing is filtering, and the Lee refined speckle filter is used [72]. After that, multiple classification features are extracted. Initial values of dictionary and class labels serve as the inputs, they are calculated by the H/α/A Wishart classifier and updated by energy function. Based on class labels, the final classification result can be obtained.

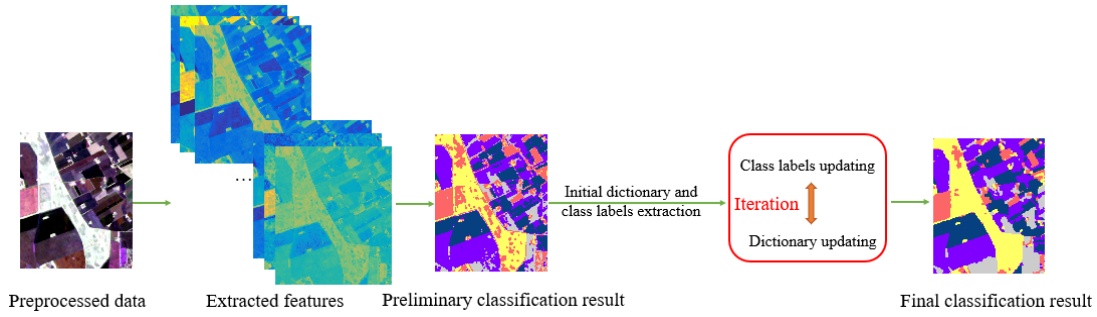

Figure 3.1: Flowchart for the classification method.

3.2.1 Classification Features

49 classification features are used for this proposed algorithm. They are concluded into two categories, polarimetric and color features. According to the research by [73], color features from PauliRGB image can act as useful classification features.

These classification features are listed as Table 3.1. The used polarimetric features include the SPAN value and values of polarization matrix elements.

3 target decomposition methods are introduced to extract the other 15 polarimetric features. These three decomposition methods include Cloude-Pottier decomposition, Neumann two-component decomposition, and Yamaguchi four-component decomposition. Cloude-Pottier decomposition [66] is based on **T** matrix, through which 8 features are calculated to serve as the classification features. Neumann two-component decomposition [68] is a model-based scheme. The modulus and phase value of parameter τ and particle scattering anisotropy δ are extracted. P_{d}, P_{s}, P_{h}, and P_{v} from Yamaguchi decomposition are also introduced [15]. The detailed information for these three decomposition methods has already been introduced in the last Section.

Except for the above polarimetric features, six color features under two color spaces are extracted for this classification method.

3.2.2 Preliminary classification method

Preliminary classification result which can be used to compose initial values is needed for this unsupervised classification method. It is calculated by H/α/A Wishart classifier.

Table 3.1: Classification features.

Category	Symbol	Description
Polarimetric matrices and mathematical transforms (polarimetric features)	$T_{11\text{mod}}$, $T_{22\text{mod}}$, $T_{33\text{mod}}$, $T_{12\text{mod}}$, $T_{13\text{mod}}$, $T_{23\text{mod}}$, $T_{12\text{mod}}$, $T_{13\text{pha}}$, $T_{23\text{pha}}$	elements of **T** under horizontal and vertical linear polarization
	$Lin45T_{11\text{mod}}$, $Lin45T_{22\text{mod}}$, $Lin45T_{33\text{mod}}$, $Lin45T_{12\text{mod}}$, $Lin45T_{13\text{mod}}$, $Lin45T_{23\text{mod}}$, $Lin45T_{12\text{pha}}$, $Lin45T_{13\text{pha}}$, $Lin45T_{23\text{pha}}$	elements of **T** under $+45°/-45°$ linear polarization
	$CirT_{11\text{mod}}$, $CirT_{22\text{mod}}$, $CirT_{33\text{mod}}$, $CirT_{12\text{mod}}$, $CirT_{13\text{mod}}$, $CirT_{23\text{mod}}$, $CirT_{12\text{pha}}$, $CirT_{13\text{pha}}$, $CirT_{23\text{pha}}$	elements of **T** under circular polarization
	SPAN	polarimetric power
Target decomposition features (polarimetric features)	H, A, α, β, HA, $(1-H)A$, $H(1-A)$, $(1-H)(1-A)$	Cloude-Pottier decomposition parameters
	τ, δ_{mod}, δ_{pha}	Neumann two-component decomposition parameters
	P_{s}, P_{d}, P_{v}, P_{h}	Yamaguchi four-component decomposition parameters
Color features	R, G, B	color features under RGB color space
	H, S, V	color features under HSV color space

Scattering mechanisms of targets can be represented by parameters H and α from Cloude-Pottier decomposition. All types of terrains can be divided into 8 classes, and every class can be found in the zones on the plane. But the results of this method are not satisfactory in some cases. [18] combined this method with the Wishart classifier. Training dataset can be formed by the initial classification algorithm, and they are used to train an effective Wishart classifier.

H/α/A Wishart classifier [74] is the extension of above method. It can better distin-

guish the different labeled classes located in the same zone. For this method, the original plane is classified into 16 zones by introducing parameter A.

3.2.3 Sparse representation based model

For an image which contains N pixels, the feature matrix is $\mathbf{X} = [\boldsymbol{x}_1, \boldsymbol{x}_2, ..., \boldsymbol{x}_N] \in R^{M \times N}$, which means that M features are extracted. Class label for pixel $i (i \in 1, ..., N)$ is presented by $y_i (y_i \in 1, ..., K)$, where K means number of classes.

SRC classifier is introduced by [26], it indicates that a few dictionary atoms can present every test sample through a suitable linear combination. $\mathbf{x}_i \in R^{M \times 1}$ represents the feature vector of pixel i. Overcomplete dictionary is $\mathbf{D} = [\boldsymbol{d}_1, \boldsymbol{d}_2, ..., \boldsymbol{d}_S] = [\mathbf{D}_1, \mathbf{D}_2, ..., \mathbf{D}_k, ..., \mathbf{D}_K] \in R^{M \times S}$, $\mathbf{D}_k \in R^{M \times S_k}$ is the sub-dictionary with class label as k, $S = \sum_{k=1}^{K} S_k$, $k = 1, ..., K$, S_k is atoms number. Test pixel can be shown as,

$$\begin{aligned} \boldsymbol{x}_i &\approx \boldsymbol{d}_1\alpha_1 + \boldsymbol{d}_2\alpha_2 + \cdots + \boldsymbol{d}_S\alpha_S \\ &= [\boldsymbol{d}_1\ \boldsymbol{d}_2\ ...\ \boldsymbol{d}_S][\alpha_1\ \alpha_2\ ...\ \alpha_S]^T = \mathbf{D}\boldsymbol{\alpha}_i \end{aligned} \tag{3.1}$$

where $\boldsymbol{\alpha}_i$ is the sparse coefficient, it can be obtained by

$$\boldsymbol{\alpha}_i = \ \arg\min_{\boldsymbol{\alpha}} \{\|\boldsymbol{x}_i - \mathbf{D}\boldsymbol{\alpha}\|_2 + \gamma\|\boldsymbol{\alpha}\|_1\} \tag{3.2}$$

where γ is a scalar constant, $\|\cdot\|_1$ and $\|\cdot\|_2$ represent the l_1 norm and l_2 norm, respectively. This problem can be approximately solved with OMP [75] method. When $\boldsymbol{\alpha}_i$ is calculated and fixed, y_i can be determined by the following equation,

$$y_i = \ \arg\min_k \|\boldsymbol{x}_i - \mathbf{D}\phi_k(\boldsymbol{\alpha}_i)\|_2 \tag{3.3}$$

where $\phi_k(\boldsymbol{\alpha}_i)$ represents setting other coefficients to zero except those labeled as k.

Energy function $E(\boldsymbol{Y}, \mathbf{D} \mid \mathbf{X})$ can be defined. Through which the $\mathbf{D}$ and $\boldsymbol{Y} = [y_1, y_2, ..., y_N]$ can be updated. $E(\boldsymbol{Y}, \mathbf{D} \mid \mathbf{X})$ contains sparse representation term and label smoothness term,

$$E(\boldsymbol{Y}, \mathbf{D} \mid \mathbf{X}) = E_{\text{sparse}}(\boldsymbol{Y}, \mathbf{D} \mid \mathbf{X}) + \lambda E_{\text{smooth}}(\boldsymbol{Y}, \mathbf{D} \mid \mathbf{X}) \tag{3.4}$$

where λ means scalar parameter. E_{sparse} correlates to data energy, E_{smooth} encodes prior knowledge on the problem.

Sparse representation term

E_{sparse} is based on the Fisher discrimination dictionary learning (FDDL) scheme [71].

$$E_{\text{sparse}}(\boldsymbol{Y}, \mathbf{D} \mid \mathbf{X}) = r(\mathbf{X}, \mathbf{D}, \mathbf{A}) \text{ s.t. } \|\mathbf{d}_s\|_2 = 1, \forall s \tag{3.5}$$

Feature vector $\mathbf{X} = [\mathbf{X}_1, ..., \mathbf{X}_k, ..., \mathbf{X}_K]$ when $\boldsymbol{Y}$ are fixed, $\mathbf{X}_k$ means the set with k as the class label. Sparse coefficient $\mathbf{A} = [\mathbf{A}_1, ..., \mathbf{A}_k, ..., \mathbf{A}_K]$, where $\mathbf{A}_k$ represents the sparse representation coefficient of $\mathbf{X}_k$ over $\mathbf{D}$. $\mathbf{A}_k = [\mathbf{A}_k^1; , ...; \mathbf{A}_k^l; ...; \mathbf{A}_k^K]$, where $\mathbf{A}_k^l$ is the sparse representation coefficient of $\mathbf{X}_k$ over $\mathbf{D}_l$.

Discriminative data fidelity term is

$$r(\mathbf{X}, \mathbf{D}, \mathbf{A}) = \sum_{k=1}^{K} r(\mathbf{X}_k, \mathbf{D}, \mathbf{A}_k) \tag{3.6}$$

where

$$r(\mathbf{X}_k, \mathbf{D}, \mathbf{A}_k) = \|\mathbf{X}_k - \mathbf{D}\mathbf{A}_k\|_F^2 + \|\mathbf{X}_k - \mathbf{D}_k\mathbf{A}_k^k\|_F^2 + \sum_{l=1, l\neq k}^{K} \|\mathbf{D}_l\mathbf{A}_k^l\|_F^2 \tag{3.7}$$

The above equation means that $\mathbf{X}_k$ can be better represented by $\mathbf{D}_k$, it means that the value of $\|\mathbf{X}_k - \mathbf{D}_k\mathbf{A}_k^k\|_F^2$ should be small, as well as $\|\mathbf{D}_l\mathbf{A}_k^l\|_F^2$.

$r(\mathbf{X}, \mathbf{D}, \mathbf{A})$ can be further written as,

$$r(\mathbf{X}, \mathbf{D}, \mathbf{A}) = \sum_{i=1}^{N} r(\boldsymbol{x}_i, \mathbf{D}, \boldsymbol{\alpha}_i) = \|\boldsymbol{x}_i - \mathbf{D}\boldsymbol{\alpha}_i\|_F^2 + \|\boldsymbol{x}_i - \mathbf{D}_{y_i}\boldsymbol{\alpha}_i^{y_i}\|_F^2 + \sum_{l=1, l\neq y_i}^{K} \|\mathbf{D}_l\boldsymbol{\alpha}_i^l\|_F^2 \tag{3.8}$$

where $\boldsymbol{\alpha}_i^{y_i}$ represents sparse coefficient of $\boldsymbol{x}_i$ over $\mathbf{D}_{y_i}$.

Label smoothness term

Label smoothness term is defined as follows, it can give penalties to different labeled neighboring pixels.

$$E_{\text{smooth}}(\boldsymbol{Y}, \mathbf{D} \mid \mathbf{X}) = \sum_{i=1}^{N} \sum_{j \in \mathcal{N}(i)} V_{\{i,j\}}(y_i, y_j) \tag{3.9}$$

$V_{\{i,j\}}(y_i, y_j)$ is neighbor iteration function, and this term calculates the sum value of all neighbor pairs' neighbor interaction functions. $\mathcal{N}(i)$ represents set of neighboring pixels for i.

Neighbor iteration function shown as follows,

$$V_{\{i,j\}}(y_i, y_j) = \begin{cases} 0 & \text{if } y_i = y_j \\ u_{\{i,j\}} & \text{otherwise} \end{cases} \tag{3.10}$$

where

$$u_{\{i,j\}} = \begin{cases} P \times s & \text{if } \|\boldsymbol{x}_i - \boldsymbol{x}_j\|_2^2 < T \\ s & \text{otherwise} \end{cases} \tag{3.11}$$

for neighbored pixels i and j, $\|\boldsymbol{x}_i - \boldsymbol{x}_j\|_2^2$ means their distance, it relates to the similarity between them. T means the threshold which can measure the similarity of neighboring pixels. Its value can be set empirically by analyzing neighboring pixels within different kinds of local regions. s and P mean the penalty term. T, P, and s are constants. For same labeled neighboring pixels, their neighbor iteration function value is 0. For the neighboring pixels whose distance is smaller than T, their penalty is $P \times s$, which is too large for the whole term. y_i and y_j will be set to be the same to minimize the smoothness term. For the neighboring pixels with large distance, such as the pixels that across strong edges, their penalty value is s, which is small to allow setting different labels to them.

Final energy function

Above all, the final energy function is,

$$
\begin{aligned}
E(\boldsymbol{Y}, \mathbf{D} \mid \boldsymbol{X}) = & \sum_{i=1}^{N} \{ \|\boldsymbol{x}_i - \mathbf{D}\boldsymbol{\alpha}_i\|_F^2 + \|\boldsymbol{x}_i - \mathbf{D}_{y_i}\boldsymbol{\alpha}_i^{y_i}\|_F^2 + \sum_{l=1, l\neq y_i}^{K} \|\mathbf{D}_l \boldsymbol{\alpha}_i^l\|_F^2 \\
& + \lambda \sum_{j \in \mathcal{N}(i)} \min\{|y_i - y_j|, 1\} u_{\{i,j\}} \} \ \text{ s.t. } \|\mathbf{d}_s\|_2 = 1, \forall s
\end{aligned}
\tag{3.12}
$$

where $u_{\{i,j\}}$ is defined as Equation 3.11. For one pair of neighboring pixels, their label smoothness term contains three situations, and the corresponding values are 0, s, and $P \times s$. When λ is considered, the label smoothness term's values is 0, λs, and $\lambda(P \times s)$. Because s and P are constants, λ can be fixed as 1.

3.2.4 Optimization

The calculation of $\mathbf{D}$ and $\boldsymbol{Y}$ is based on the updating of their initial values. This work is done by alternately minimizing the energy function, and it mainly contains two steps.

Class labels updating

For this step, $\mathbf{A}$ and $\mathbf{D}$ should be fixed, and through minimizing the corresponding energy function, $\boldsymbol{Y}$ can be updated. For the first loop, $\mathbf{D}$ is the initial value. For the step that iteration number (IN) comes to value that bigger than 1, $\mathbf{D}$ is the one that obtained during the last iteration ($IN - 1$). With $\mathbf{X}$ and $\mathbf{D}$ are fixed, the calculation of $\mathbf{A}$ can be done by the OMP method. Therefore, for class labels updating, energy function 3.12 is,

$$
\begin{aligned}
E(\boldsymbol{Y}, \mathbf{D} \mid \mathbf{X}) = & \sum_{i=1}^{N} \{ \|\boldsymbol{x}_i - \mathbf{D}_{y_i}\boldsymbol{\alpha}_i^{y_i}\|_F^2 + \sum_{l=1, l\neq y_i}^{K} \|\mathbf{D}_l \boldsymbol{\alpha}_i^l\|_F^2 \\
& + \lambda \sum_{j \in \mathcal{N}(i)} \min\{|y_i - y_j|, 1\} u_{\{i,j\}} \}
\end{aligned}
\tag{3.13}
$$

The Markov Random Field (MRF) model is introduced here to solve this optimization problem. For the whole image, an undirected graph $\mathcal{G} = \langle \mathcal{V}, \mathcal{E} \rangle$ can be built. $\mathcal{V}$ is node set, it represents pixels. The undirected edge set $\mathcal{E}$ represents the relationship of neighboring pixels. $\boldsymbol{Y}$ for the whole image can build an MRF model, to solve this

problem, the Belief Propagation (BP) algorithm [76] can be employed.

Dictionary updating

With fixed $\boldsymbol{Y}$, the next step is updating $\mathbf{D}$. Energy function 3.12 here is,

$$\begin{aligned} E(\boldsymbol{Y}, \mathbf{D} \mid \mathbf{X}) &= \sum_{i=1}^{N} \{ \|\boldsymbol{x}_i - \mathbf{D}\boldsymbol{\alpha}_i\|_F^2 + \|\boldsymbol{x}_i - \mathbf{D}_{y_i}\boldsymbol{\alpha}_i^{y_i}\|_F^2 + \sum_{l=1, l\neq y_i}^{K} \|\mathbf{D}_l \boldsymbol{\alpha}_i^l\|_F^2 \\ &= \sum_{k=1}^{K} r(\mathbf{X}_k, \mathbf{D}, \mathbf{A}_k) \ \text{ s.t. } \|\mathbf{d}_s\|_2 = 1, \forall s \end{aligned} \tag{3.14}$$

Dictionary updating method from FDDL is employed here to solve the above equation.

$\mathbf{D}$ is calculated by updating $\mathbf{D}_k = [\mathbf{d}_1, \mathbf{d}_2, ..., \mathbf{d}_{S_k}]$. At that time, all $\mathbf{D}_l$ ($l \neq k$) are fixed. The equation is,

$$\begin{aligned} &\min_{\mathbf{D}_k} = \{ \|\hat{\mathbf{X}} - \mathbf{D}_k \mathbf{A}^k\|_F^2 + \|\mathbf{X}_k - \mathbf{D}_k \mathbf{A}_k^k\|_F^2 + \sum_{l=1, l\neq k}^{K} \|\mathbf{D}_k \mathbf{A}_l^k\|_F^2 \} \\ &\text{s.t. } \|\mathbf{d}_z\|_2 = 1, z = 1, 2, ..., S_k \end{aligned} \tag{3.15}$$

where $\hat{\mathbf{X}} = \mathbf{X} - \sum_{l=1, l\neq k}^{K} \mathbf{D}_l \mathbf{A}^l$, $\mathbf{A}^l$ is sparse coefficient of $\mathbf{X}$ over $\mathbf{D}_l$. Thus, the above equation can be written as

$$\min_{\mathbf{D}_k} = \|\mathbf{Z}_k - \mathbf{D}_k \boldsymbol{\Lambda}_k\| \ \text{ s.t. } \|\mathbf{d}_z\|_2 = 1, z = 1, 2, ..., S_k \tag{3.16}$$

where $\mathbf{Z}_k = [\hat{\mathbf{X}}\ \mathbf{X}_k\ \mathbf{0}...\mathbf{0}\ \mathbf{0}...\mathbf{0}]$, $\boldsymbol{\Lambda}_k = [\mathbf{A}^k\ \ \mathbf{A}_k^k\ \ \mathbf{A}_1^k ... \mathbf{A}_{k-1}^k\ \mathbf{A}_{k+1}^k ... \mathbf{A}_K^k]$, $\mathbf{0}$ means zero matrix. The algorithm like [77] or [78] can be used to solve this updating problem.

3.3 Results and discussions

Three PolSAR images are introduced to test this algorithm.

3.3.1 Foulum dataset

The used Foulum data is about the Foulum area, Denmark. It is under L-band and obtained on April 17, 1988. The airborne system that got this data is EMISAR. Its

PauliRGB image is shown as Figure 3.2 (a). Subfigure (b) shows the ground-truth. Its image size is 495×600. In this area, there exist five kinds of targets.

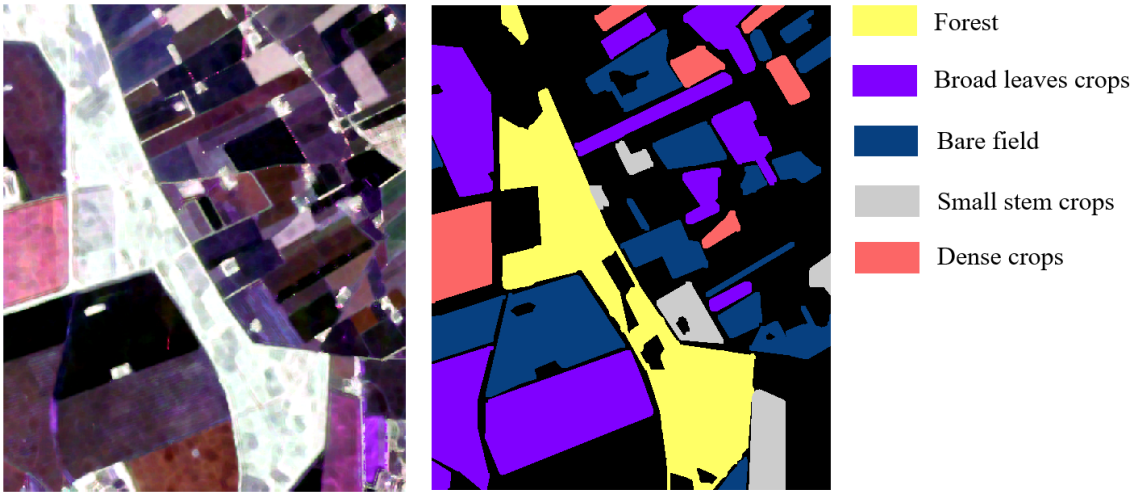

(a) PauliRGB image (b) Ground-truth image

Figure 3.2: PauliRGB and ground-truth image for Foulum area.

Validity analysis

Figure 3.3 (a) is the initial classification result. It shows that this unsupervised algorithm can obtain a satisfactory classification result. However, many misclassified regions exist. As can be seen, parts of forest areas are mislabeled as dense crops. At the same time, the small stem crops and broad leaves crops cannot be discriminated well.

Subfigure (b)-(d) are the results by the method in this chapter during different loops. T, s, and P are set as 2, 2, and 8, respectively. The size of D is $49 \times (5 \times Dsize)$ with $Dsize = 50$. The dictionary size represents that 50 dictionary atoms should be selected for every category to compose D. When the IN is 1, the initial dictionary is used. When IN equals to 2, D is the one acquired during the last loop. When IN is 6, Y have been updated six times, and the updating time for D is five. Figure 3.3 (b)-(d) show that classification performance is getting better step-by-step. For the sixth loop, almost all pixels are labeled accurately. The preliminary result's classification accuracy is 90.35%, while the accuracies for the other three results are 92.34%, 93.33%, and 94.44%, respectively.

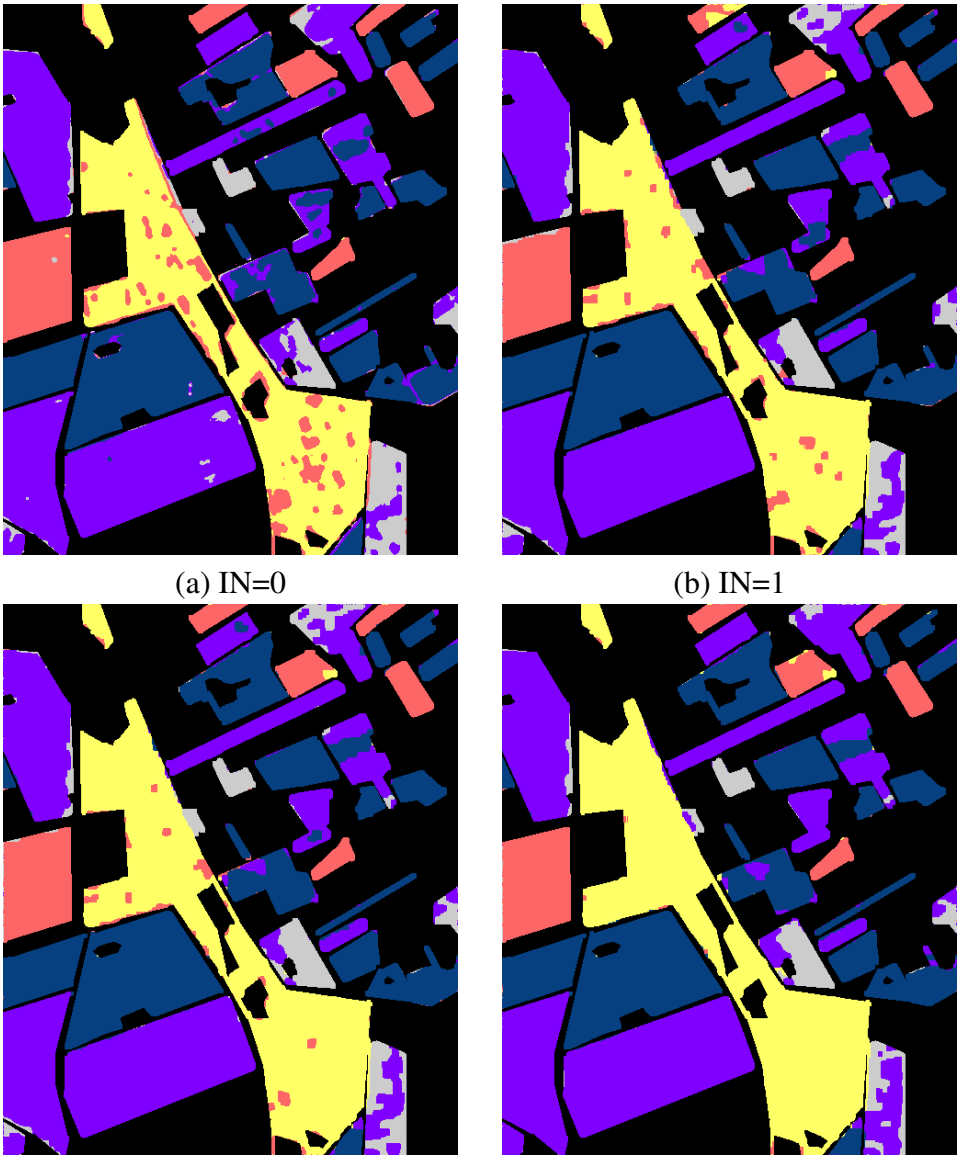

(a) IN=0 (b) IN=1

(c)IN=2 (d) IN=6

Figure 3.3: Classification results using proposed method for Foulum data. (a) IN=0 (preliminary result), accuracy=90.35%. (b) IN=1, accuracy=92.15%. (c) IN=2, accuracy=93.14%. (d) IN=6, accuracy=94.19%.

Parameter analysis

The final energy function indicates that the label smoothness term's performance is determined by the value of $P \times s$. s is set experimentally, it represents the penalty for neighboring pixels that with little similarity. The principle is to ensure its value is small enough to guarantee that setting different labels to this pair of neighboring pixels is al-

lowable. For this data, s is 2. Results by different $P \times s$ values are shown as Figure 3.4. The used dictionary is all the same at $Dsize = 100$, and IN=1.

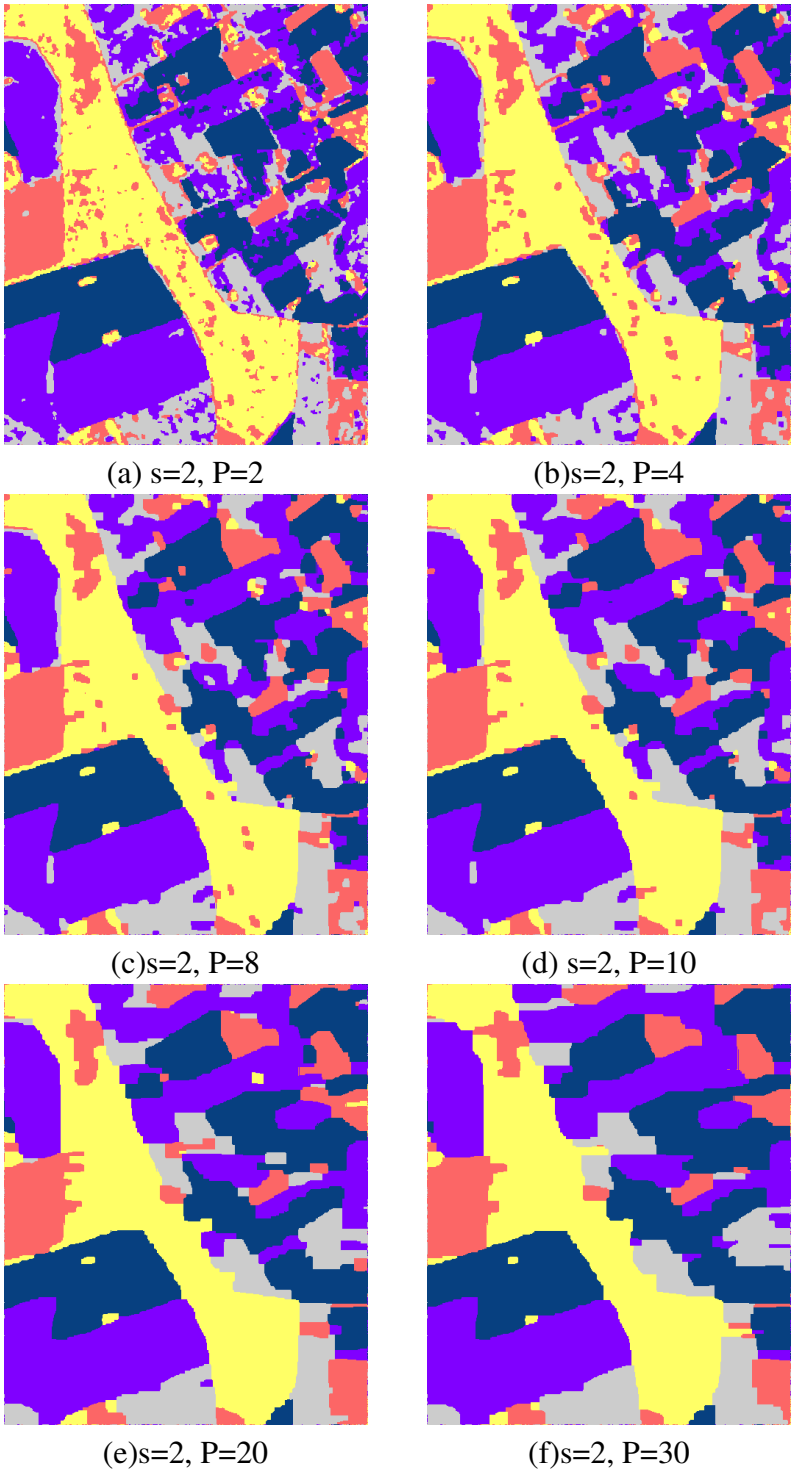

(a) s=2, P=2 (b)s=2, P=4

(c)s=2, P=8 (d) s=2, P=10

(e)s=2, P=20 (f)s=2, P=30

Figure 3.4: Classification results with different $P \times s$ values (Dsize=100 and IN=1).

Figure 3.4 shows that when $P \times s$ is small, many small misclassified regions exist. For the reason that this small value leads to the result that penalty value makes little influence on sparse representation term. It leads to the result that many neighboring pixels within flat regions are not labeled the same. However, when $P \times s$ is set too large, misclassification around the edge exists. Thus, P is set as 8 for the Foulum dataset.

Figure 3.5 shows the influence of another two parameters, IN and Dsize. As introduced before, the initial dictionary is composed by the preliminary classification result. Its randomness will affect the final classification results. To solve this problem, the accuracies of the results in the following discussions are ten results' averaged accuracy values with different initial D.

With IN=0, the overall accuracy shown in Figure 3.5 corresponds to the preliminary classification method. According to Figure 3.5, all results using the proposed method performs better. Accuracy rises rapidly with $Dsize$ is 50. During the same iteration loop, the accuracy value increased with Dsize is getting bigger, and the increasing speed slows down.

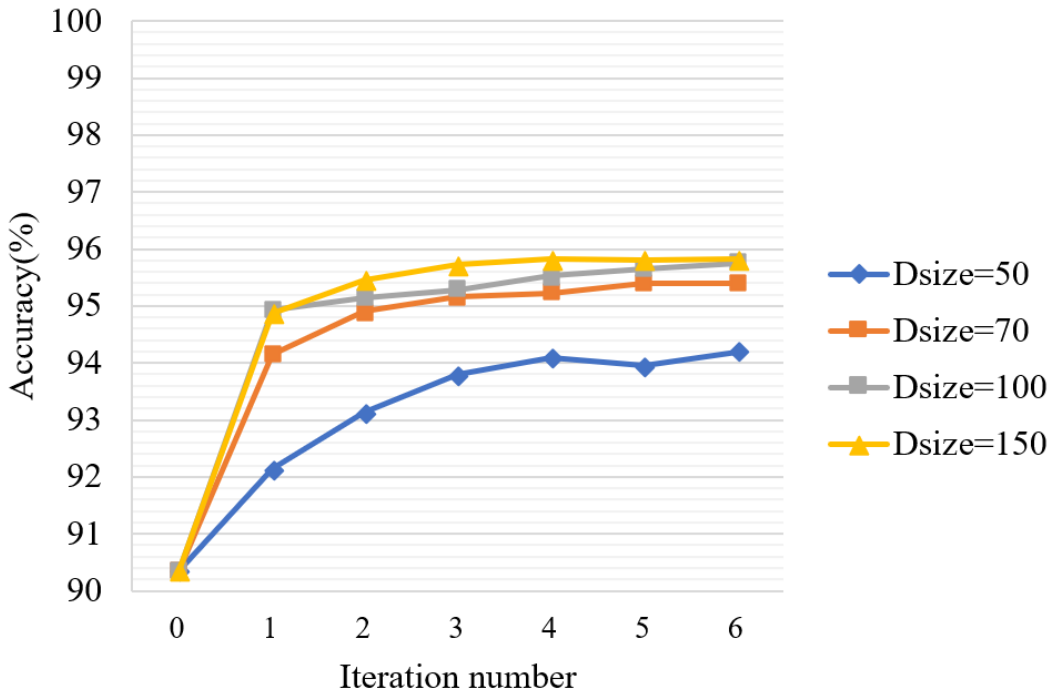

Figure 3.5: Classification accuracies with different IN and $Dsize$.

Comparison with other classification methods

Comparison with other three supervised methods is also implemented to test the superiority of this method. Results by SRC, SVM, and supervised Wishart classifier are calculated. Training data of all the supervised algorithms are the same.

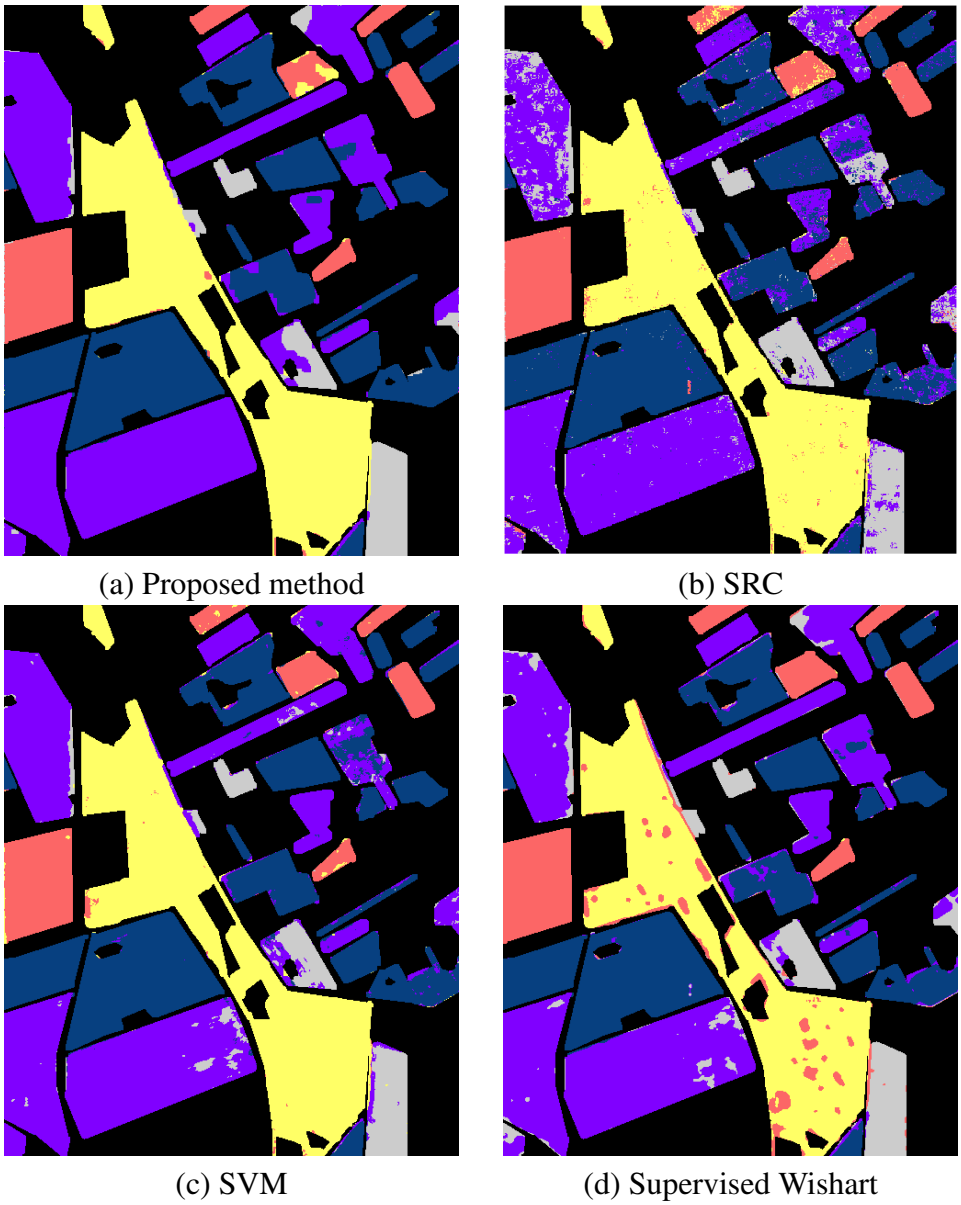

(a) Proposed method (b) SRC

(c) SVM (d) Supervised Wishart

Figure 3.6: Classification results by different algorithms. (a) Result by the proposed method (IN=6, $Dsize = 100$). (b) Result by SRC. (c) Result by SVM. (d) Result by supervised Wishart.

Figure 3.6 shows the classification results. Most supervised algorithms acquire rela-

tively good results because of the training processing. But misclassification still exists. For example, forest in the result by supervised Wishart classifier and broad leaves crops in the result by SRC classification. Compared with other supervised algorithms, SVM method acquires the best performance even though misclassification also exist. Figure 3.6 (a) is the proposed method's classification result with $IN = 6$ and $Dsize = 100$ which presents the best performance among all these results, most targets are labeled with the right class.

Table 3.2: Classification accuracies with different classifiers (%).

	H/α/A Wishart	SRC	SVM	S-Wishart	Proposed
Forest	84.36	98.18	98.10	90.37	**98.49**
Dense Crops	98.98	94.22	96.76	**99.38**	94.20
Broad Leaves Crops	93.28	85.14	93.51	93.68	**96.26**
Bare Field	94.27	92.57	97.12	94.97	**97.44**
Small Stem Crops	71.95	82.19	72.48	**89.54**	79.83
Overall	90.35	90.96	94.63	93.40	**95.75**

Table 3.2 shows the accuracies for every single category and the overall image. For these five algorithms, only this work and the H/α/A Wishart classification are unsupervised. Accuracy of this work is 95.75%, it is the best. As for other methods, the result by SVM classifier is the best, and the accuracy of H/α/A Wishart classifier is the lowest.

3.3.2 San Francisco dataset

L-band data was obtained by NASA/JPL AIRSAR system for the San Francisco area. Its PauliRGB image is shown as Figure 3.7 (a), and the image size is 750×880. The corresponding ground-truth image is shown as Figure 3.7 (b). Besides the shown three terrain types, some small areas such as parks, small lakes, and small sports fields exist. Some of them are marked on the PauliRGB image. These small areas will disturb the classification accuracy by classifying this data into three classes. Thus, another class is added here, which represents this area. When calculating the classification accuracy, the three classes shown in the ground-truth image will be considered. s P, and T are set as 2, 6, and 1.9 for the San Francisco dataset, respectively.

(a) PauliRGB image (b) Ground-truth image

Figure 3.7: PauliRGB and ground-truth image for San Francisco area.

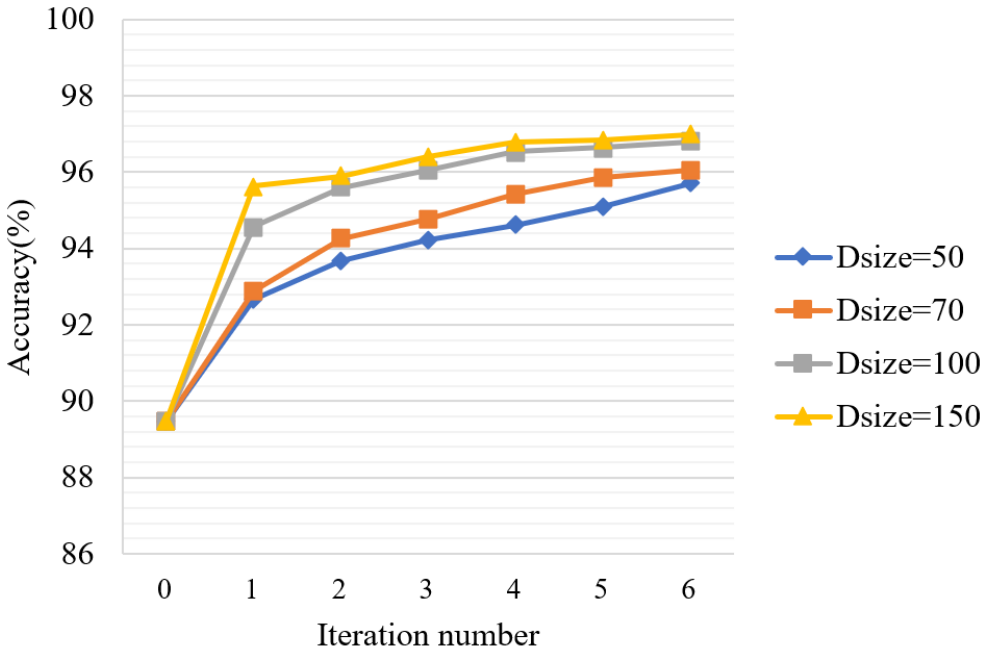

Figure 3.8: Classification accuracies with different IN and $Dsize$.

Parameter analysis

Figure 3.8 shows the classification accuracies when dictionary size and iteration number are set with different values. The same conclusion with the Foulum dataset can be given. For the San Francisco area, the classification accuracy increases when iteration process-

ing in progress. Moreover, with the dictionary that in a larger size, the classification accuracy becomes higher.

Comparison experiments

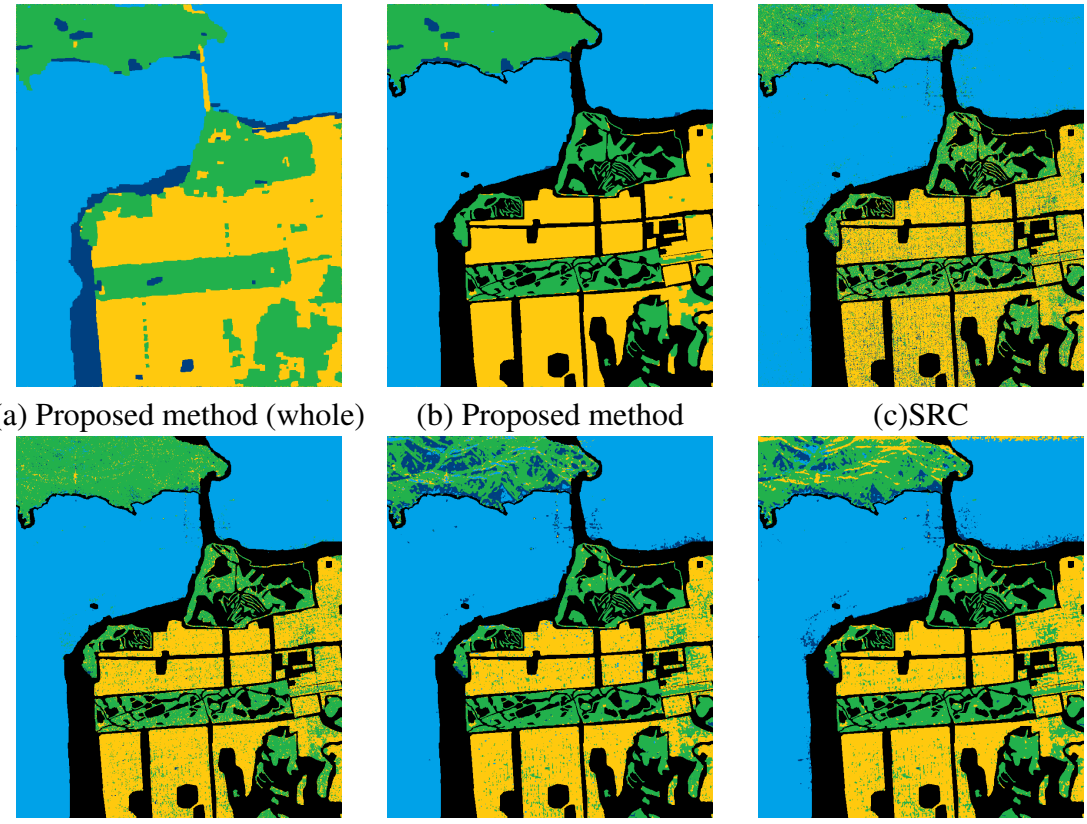

(a) Proposed method (whole) (b) Proposed method (c)SRC

(d) SVM (e) H/α/A Wishart (f) Supervised Wishart

Figure 3.9: Classification results by different algorithms. (a) Result by the proposed method (for whole dataset). (b) Result by the proposed method. (c) Result by SRC. (d) Result by SVM. (e) Result by H/α/A Wishart classifier. (f) Result by supervised Wishart classifier.

Figure 3.9 represents results of five classification methods. Figure 3.9 (a) is the result of the whole image, it is by the algorithm proposed in this chapter. The special categories are marked with dark blue. The region blocked with a yellow rectangle (shown as Figure 3.7 (a)) is the sea area where strong speckle noise exists. These areas are labeled with dark blue. Figures 3.9 (b)-(f) show the results with ground-truth information provided. The algorithm in this chapter (Figure 3.9 (b)) shows the most satisfactory performance.

While many misclassified small regions exist in the vegetation and urban areas in the results by the other four methods.

Table 3.3: Classification accuracy by different algorithms (%).

	SVM	SRC	H/α/A Wishart	Supervised Wishart	Proposed
Vegetation	99.59	98.88	99.02	97.35	**99.87**
Urban	89.74	78.98	75.39	79.52	**93.05**
Ocean	85.98	81.15	85.33	86.39	**95.45**
Overall	93.35	89.06	89.45	89.95	**96.80**

Table 3.3 shows the accuracies for this data. The accuracy by the proposed method increases by 7.35% when compared with preliminary classification result. This table indicates that result by the method proposed in this chapter has the highest accuracy.

3.3.3 Flevoland dataset

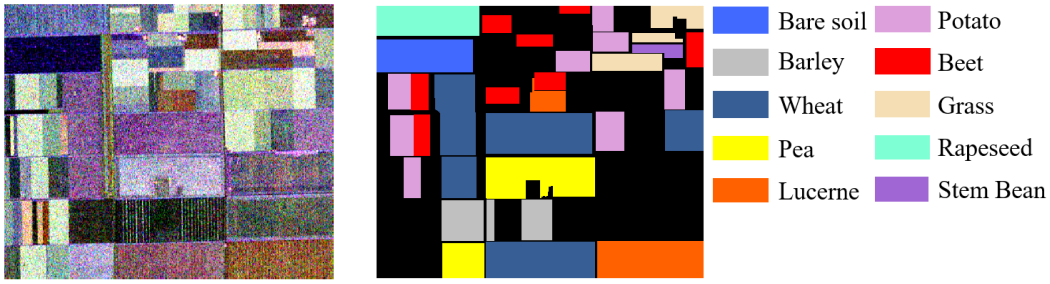

(a) PauliRGB image (b) Ground-truth image

Figure 3.10: PauliRGB and ground-truth image for the Flevoland area.

Image of Flevoland area is also tested. It was under C-band and acquired on August 16, 1989, by NASA/JPL AIRSAR system. Its size is 406 $\times$ 339. Figure 3.10 presents its PauliRGB and ground-truth image. Classification work for Flevoland image is to classify different kinds of farmlands. s, P, and T are set as 2, 8, and 2, respectively.

Figure 3.11 shows the classification results of five methods. For Figure 3.11 (a), IN is 6 and $Dsize = 100$. Serious classification errors exist in the results by SVM, SRC, and H/α/A Wishart classifier. It is because of the disturb of speckle noise. The method proposed in this section gives the best result.

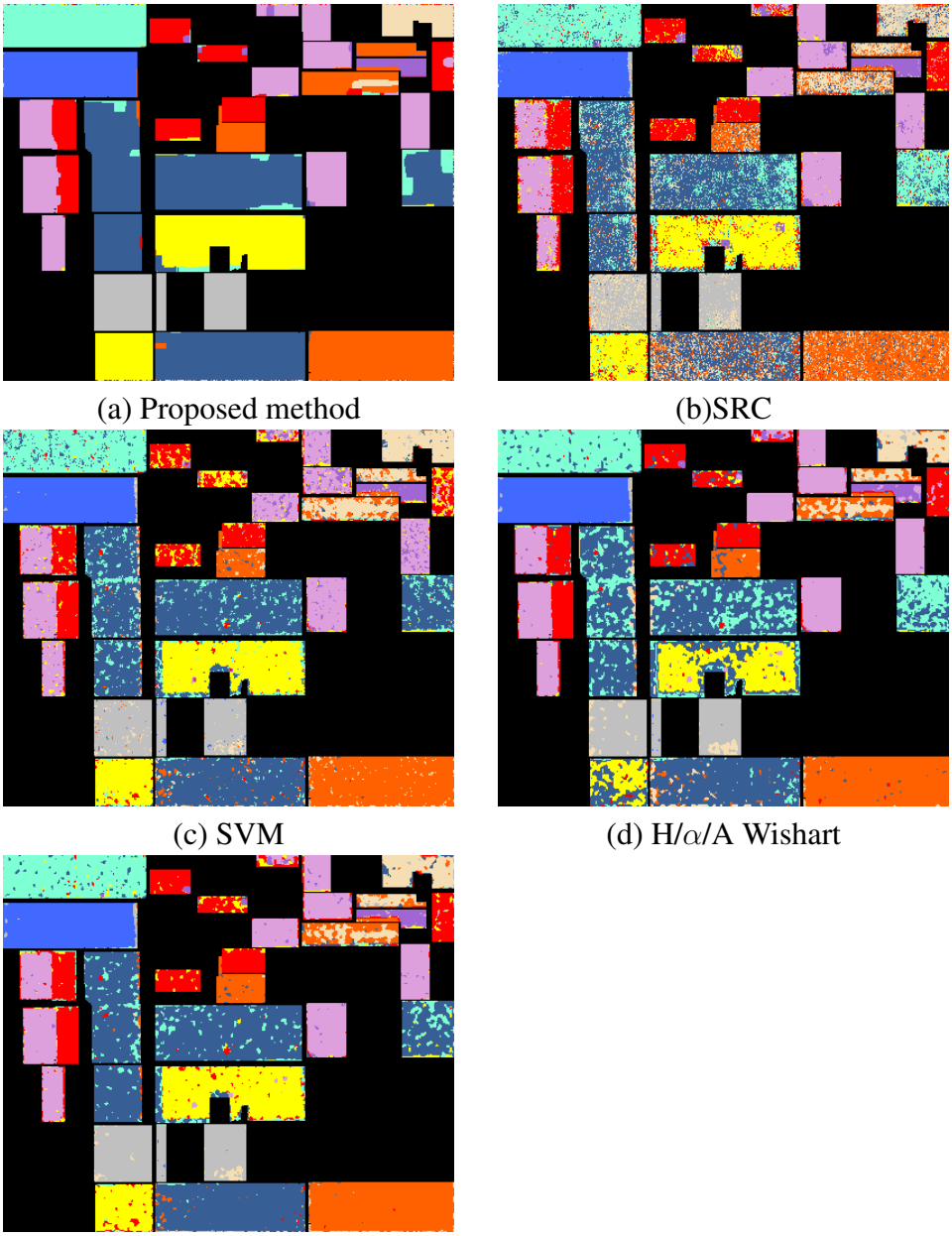

(a) Proposed method (b)SRC

(c) SVM (d) H/α/A Wishart

(e) Supervised Wishart

Figure 3.11: Classification results by different algorithms. (a) Result by proposed method. (b) Result by SRC. (c) Result by SVM. (d) Result by H/α/A Wishart classifier. (e) Result by supervised Wishart classifier.

Table 3.4 gives a better exhibition to compare these results. The performance of the algorithm in this chapter in the best, but there are two regions that should be labeled as the grass is classified as Lucerne. Table 3.4 also indicates that the classification performance for the grass field is worse than other algorithms. The reason is that grass and

Table 3.4: Classification accuracies by different algorithms (%).

	SVM	SRC	H/α/A Wishart	Supervised Wishart	Proposed
Pea	82.54	75.24	57.79	83.68	**95.33**
Beet	70.18	79.30	81.61	85.76	**86.54**
Wheat	85.71	62.07	71.01	89.12	**94.05**
Grass	**73.95**	52.60	57.82	58.35	44.72
Potato	82.85	87.16	93.85	92.04	**98.09**
Barley	91.44	74.46	90.95	94.15	**100.00**
Lucerne	93.86	75.40	95.58	96.70	**99.18**
Rapeseed	87.55	85.08	91.67	91.95	**98.81**
Bare Soil	97.90	96.27	96.81	96.71	**99.33**
Stem Bean	71.96	80.51	63.54	69.55	**82.31**
Overall	84.88	74.12	79.50	88.39	**92.71**

Lucerne share similar feature characteristics. For these two targets, once the dictionary atoms are updated wrongly, this error will continue during the following loops.

3.4 Comparison with the unsupervised method using discriminative clustering

The classification method proposed by Bi et al. [79] is based on a similar framework as above. The energy function for this method also contains two terms, and one is based on the supervised softmax regression (SR) model, the other one is a Markov random field smoothness constraint, which is used to enforce the class labels for neighboring pixels to be the same.

The energy function is defined as the following equation,

$$E(\boldsymbol{Y}, \mathbf{W} \mid \mathbf{X}) = E_{\mathrm{c}}(\boldsymbol{Y}, \mathbf{W} \mid \mathbf{X}) + E_{\mathrm{s}}(\boldsymbol{Y}, \mathbf{W} \mid \mathbf{X}) \tag{3.17}$$

where $E_{\mathrm{c}}(\boldsymbol{Y}, \mathbf{W} \mid \mathbf{X})$ represents the discriminative clustering term and $E_{\mathrm{s}}(\boldsymbol{Y}, \mathbf{W} \mid \mathbf{X})$ means the label smoothness term.

The discriminative clustering term is based on the SR model that defined as

$$
\begin{aligned}
h_W(x_i) &= \begin{bmatrix} P(y_i = 1|x_i; W) \\ P(y_i = 2|x_i; W) \\ \vdots \\ P(y_i = K|x_i; W) \end{bmatrix} \\
&= \frac{1}{\sum_{j=1}^{K} e^{W_j^T x_i}} \begin{bmatrix} e^{W_1^T x_i} \\ e^{W_2^T x_i} \\ \vdots \\ e^{W_K^T x_i} \end{bmatrix}
\end{aligned}
\tag{3.18}
$$

where $W = [W_1, W_2, ..., W_K]^T$, and W_j represents the parameter vector of the classifier for the class j. $h_W(x_i)$ gives the probability when the test pixel is labeled with different classes.

The discrimination term E_{c} is defined as

$$
\begin{aligned}
E_c(\boldsymbol{Y}, \mathbf{W} \mid \mathbf{X}) =& L(\boldsymbol{Y}, \mathbf{W} \mid \mathbf{X}) + R(\mathbf{W}) \\
=& -\sum_{i=1}^{N}\sum_{j=1}^{K} \frac{1}{N_j} 1\{y_i = j\} \log \frac{e^{W_j^T x_i}}{\sum_{l=1}^{K} e^{W_l^T x_i}} + \alpha_c \sum_{i=1}^{K}\sum_{j=1}^{M} W_{ij}^2
\end{aligned}
\tag{3.19}
$$

where $L(\boldsymbol{Y}, \mathbf{W} \mid \mathbf{X})$ means the softmax loss function and $R(\mathbf{W})$ is regularization item.

The label smoothness term E_{s} is defined as

$$
E_{\mathrm{s}}(\boldsymbol{Y}, \mathbf{W} \mid \mathbf{X}) = \alpha_{\mathrm{s}} \sum_{i=1}^{N} \sum_{j \in \mathcal{N}(i)} \mathcal{S}_{ij} \tag{3.20}
$$

where

$$
\mathcal{S}_{ij} = |y_i - y_j| \exp(-\frac{\|v_i - v_j\|_2^2}{2\sigma}) \tag{3.21}
$$

α_s means the label smoothness factor and σ represents the mean squared distance of neighboring pixels i and j. The whole energy function using discriminative clustering is defined as

$$
\begin{aligned}
E(\boldsymbol{Y}, \mathbf{W} \mid \mathbf{X}) = & -\sum_{i=1}^{N}\sum_{j=1}^{K}\frac{1}{N_j}1\{y_i = j\}\log\frac{e^{W_j^T x_i}}{\sum_{l=1}^{K} e^{W_l^T x_i}} \\
& + \alpha_c \sum_{i=1}^{K}\sum_{j=1}^{M} W_{ij}^2 \\
& + \alpha_{\mathrm{s}} \sum_{i=1}^{N}\sum_{j\in\mathcal{N}(i)} |y_i - y_j| \exp(-\frac{\|v_i - v_j\|_2^2}{2\sigma})
\end{aligned}
\tag{3.22}
$$

The optimization processing for this method contains three steps. The first step is to update $\mathbf{W}$ with fixed class label $\boldsymbol{Y}$, the second step is to update class label $\boldsymbol{Y}$ with fixed $\mathbf{W}$. The last step is to update the pixel number. For the detailed information of this equation and the corresponding optimization method, please refer to [79].

The energy function of the above unsupervised method is similar to that of the proposed classification method. Both of them contain two terms, and the label smoothness constraint is applied. The method by Bi et al. uses the discriminative clustering, while the proposed method is based on the sparse representation theory. Moreover, the label smoothness constraints for these two methods are in different structures. According to the analyses by Bi et al., the overall accuracy by the method using discriminative clustering only increases significantly in the first iteration. During the optimization processing, the overall accuracy value is improved slightly. For some cases, it will even decrease just from the second iteration loop. It means that the iteration processing makes little significance.

Table 3.5: Classification accuracy of the San Francisco dataset using different methods (%).

	Unsupervised method using discriminative clustering	Proposed method
Vegetation	99.62	**99.87**
Urban	83.15	**93.05**
Ocean	93.09	**95.45**
Overall	93.81	**96.80**

To better compare these two methods, the comparison experiments are conducted

based on the analysis of the San Fransisco dataset and the Flevoland dataset.

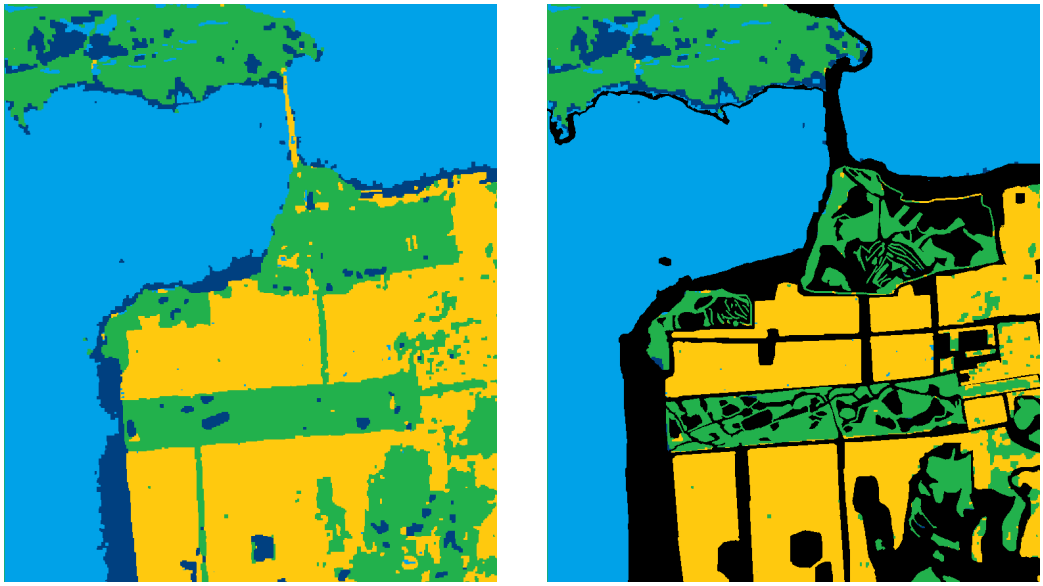

(a) Unsupervised method using discriminative clustering (whole dataset)

(b)Unsupervised method using discriminative clustering

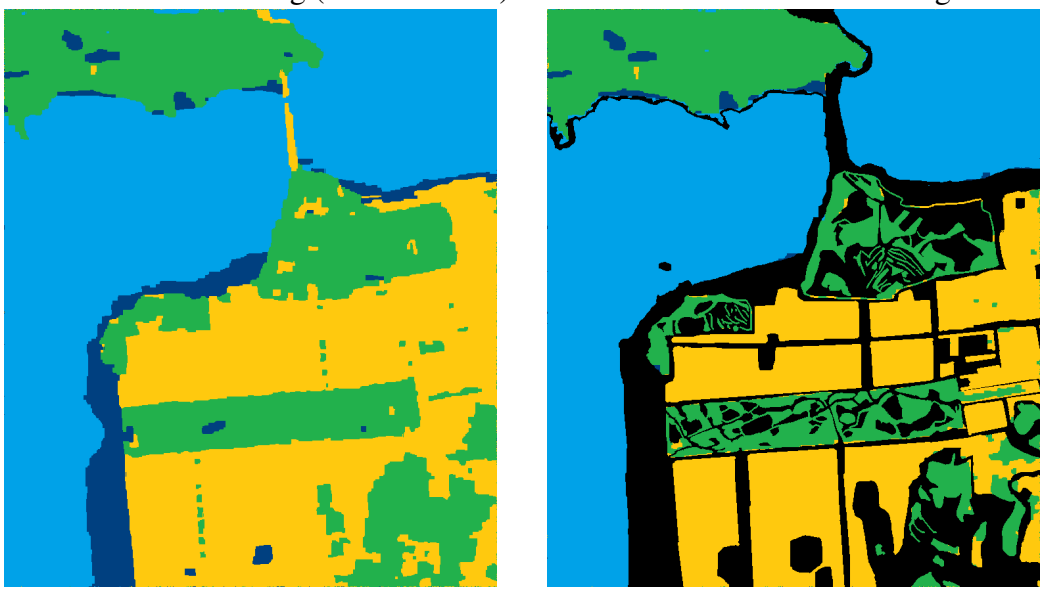

(c) Proposed method (whole dataset)

(d) Proposed method

Figure 3.12: Classification results for the San Fransisco area by different algorithms. (a) Result by the unsupervised method using discriminative clustering (for the whole dataset). (b) Result by the unsupervised method using discriminative clustering. (c) Result by the proposed method (for the whole dataset). (d) Result by the proposed method.

Figure 3.12 shows the classification results by these two methods for the San Fran-

sisco dataset. Both of them can obtain satisfactory results. But great misclassification exists especially in vegetation areas when using the method based on discriminative clustering theory. The result of the proposed method shows better performance, and most targets are classified accurately.

Table 3.5 can better compare the performance of these two methods. It indicates that the accuracies for every category and the overall image are higher than those by the method using discriminative clustering. Which means the proposed method can obtain better classification result.

The comparison experiments by analyzing the Flevoland area are also conducted. Figure 3.13 (a) shows the PauliRGB image for the Flevoland area that Bi et al. have tested. Seven categories exist in this area, and the corresponding ground truth image is shown as Figure 3.13 (b).

Figure3.14 presents the classification results by the proposed method and the technique that using discriminative clustering for this area. Table 3.6 shows the accuracies for these two results. The performance of these two methods for this area is similar. The overall accuracy for the proposed method is a little higher.

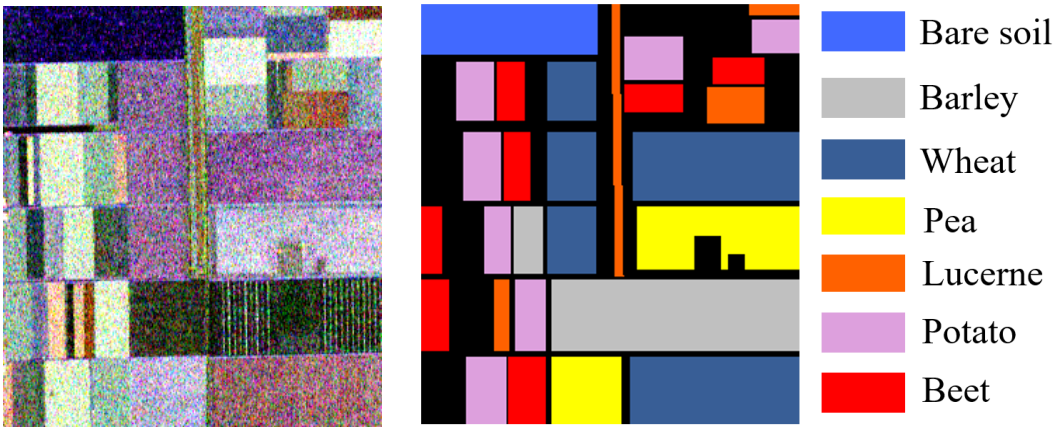

(a) PauliRGB image (b) ground truth image

Figure 3.13: PauliRGB image and the corresponding ground truth image for another region in Flevoland area

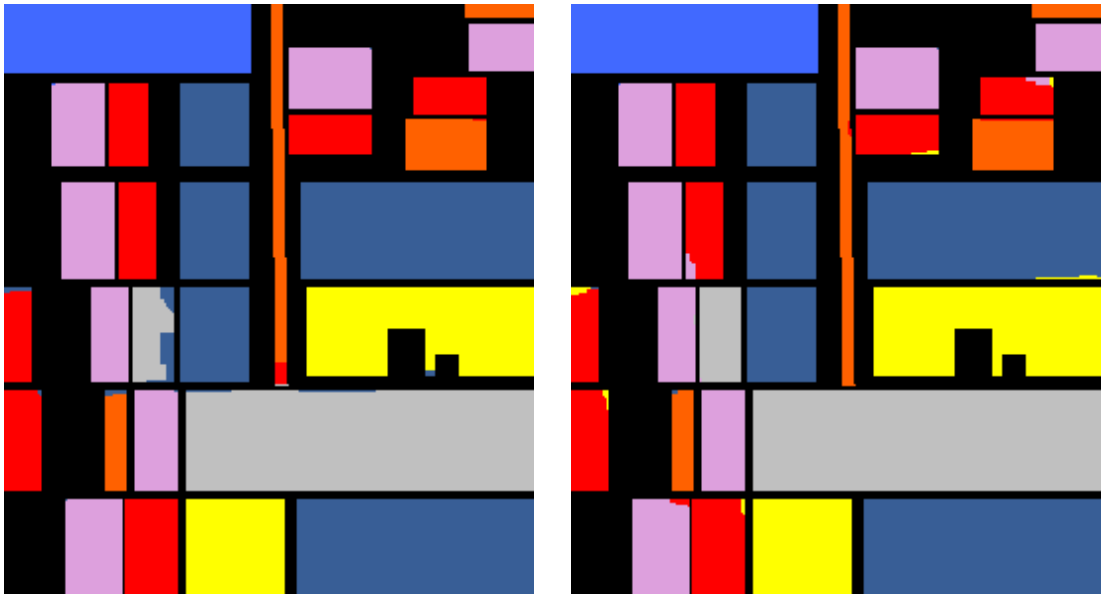

(a) Unsupervised method using discriminative clustering

(b) Proposed method

Figure 3.14: Classification results by the unsupervised method using discriminative clustering and the proposed method

Table 3.6: Classification accuracies for another area of the Flevoland dataset using different methods (%).

	Unsupervised method using discriminative clustering	The proposed method
Bare Soil	100.00	100.00
Lucerne	96.50	98.22
Wheat	100.00	99.74
Barley	97.14	99.98
Pea	99.79	100.00
Beet	99.42	97.06
Potato	99.92	99.56
Overall	99.18	99.42

3.5 Conclusion

An unsupervised classification method is presented in this chapter. By employing sparse representation theory, this method can obtain accurate classification results. By introducing the label smoothness constraint, neighboring pixel pairs that have similar features are enforced to have the same label. The above two technique is combined to compose

the new energy function. Through which class labels and dictionary can be updated.

This proposed technique is applied to three PolSAR datasets. The conducted experiments show that the classification accuracy increases with the iteration proceeded, which tested the validity of this algorithm. Influence of $P \times s$, $Dsize$, and IN to the final classification result was also detailed analyzed. Otherwise, comparison with other four supervised/unsupervised algorithms shows that the proposed method performs best.

4

Earthquake Damage Level Mapping using Pre- and Post-event PolSAR datasets

4.1 Introduction

In this chapter, a damage level index for urban areas is proposed. It uses the pair of PolSAR data acquired before and after the disaster event. The proposed damage level mapping algorithm contains two parts. Firstly, a region-based classification method is introduced, which can extract all the pixels that should be labeled as urban area, and it is implemented on data obtained before the disaster. For the second part, urban areas' damage level is evaluated by the proposed index, and it is based on the two datasets. For damage level calculation, the change of double-bounce scattering power is analyzed. However, it does not work well for seriously damaged buildings. Distance metric learning (DML) algorithm [80, 81] is used to solve this problem. Through DML algorithm, which can obtain Mahalanobis metric, the index under this metric can better interpret the damage situation. The proposed damage level index is implemented and verified by the detailed analysis of the Tohoku earthquake/tsunami event. An assessment map is crated for result evaluation. The linear fitting of the result with truth values is also analyzed. It further tests the validity of the new index. To verify the robustness of the index, a series of analysis about Kumamoto earthquake event is also conducted.

4.2 Study area

The information about the main study event, Tohoku earthquake/tsunami, and our used PolSAR data are detailedly introduced in this section.

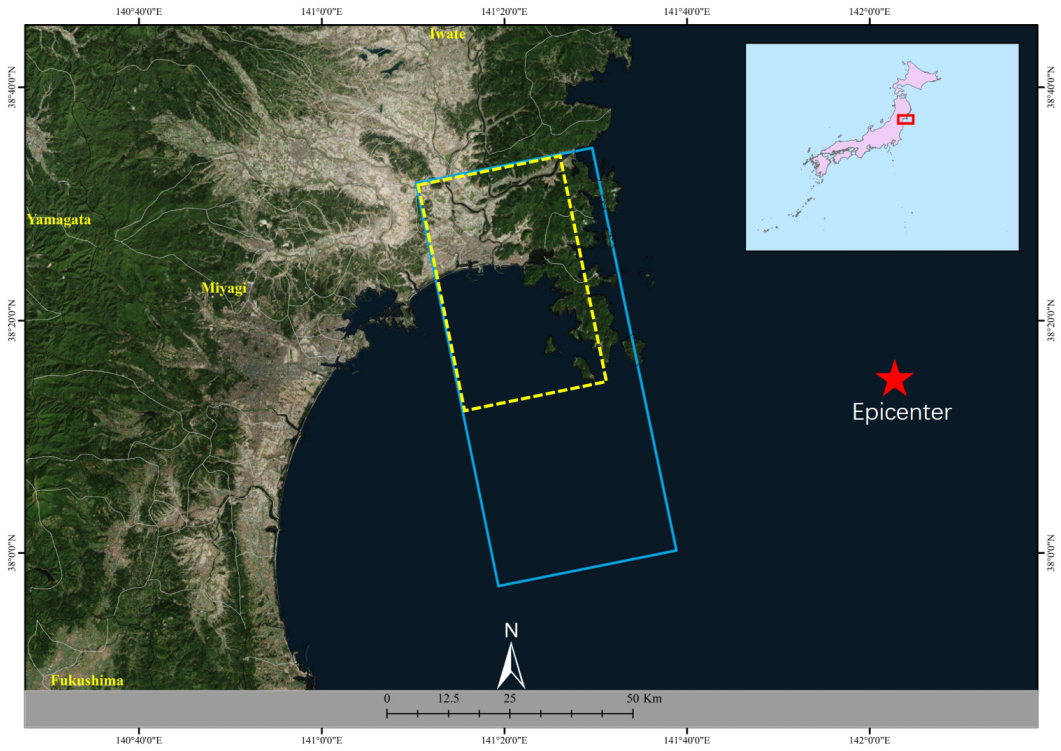

Figure 4.1: Location information about the Tohoku earthquake/tsunami. The study area is marked with yellow rectangle, the ALOS/PALSAR footprint is marked with blue rectangle.

The Tohoku earthquake, with a magnitude as 9, occurred on March 11, 2011. Along with this earthquake, the serious tsunami brought heavily damage along with northeastern Japan's coastal areas. Because of the large coverage scale of damage, the ground-survey based damage information detection methods [82, 83] are too difficult. Corresponding remote sensing technology exhibits strong superiority for this kind of work.

PolSAR data can provide multiple information to detect the texture of different terrains. It can be used for damage interpretation. The used PolSAR data to verify the proposed damage level index was obtained by ALOS satellite of JAXA [84–86]. Figure 4.1 indicates the location information of the study area, Miyagi Prefecture.

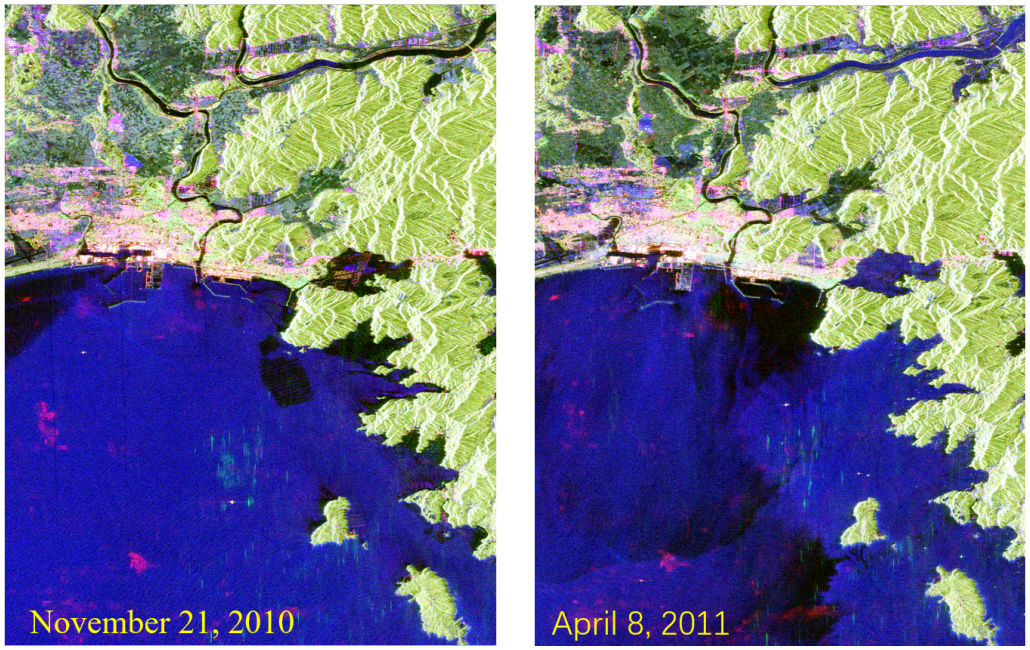

(a) Pre-event (b) Post-event

Figure 4.2: The preprocessed pre- and post-event PauliRGB images of the study area.

Two single look complex (SLC), ALOS/PALSAR fully PolSAR data are chosen. The post-event image was obtained on April 8, 2011, and the pre-event image was obtained on November 21, 2010. Because of serious decorrelation effect, polarimetric SAR interferometry mode [87, 88] cannot be used. For preprocessing, co-registration is applied to both of these two datasets. Resolution of these two images is 23.14m in ground-range directions and 4.45m in the azimuth direction. In the azimuth direction, multi-looking (eight-looking) processing is applied. The preprocessed PauliRGB images are shown as Figure. 4.2 (a) and (b).

4.3 Methodology

Figure 4.3 gives the illustration of this algorithm. Preprocessing step includes co-registration and multi-looking. Several polarimetric features are extracted from pre-event data. Then, a region-based classification method is employed through which the urban areas can be extracted. The used segmentation algorithm is multiresolution seg-

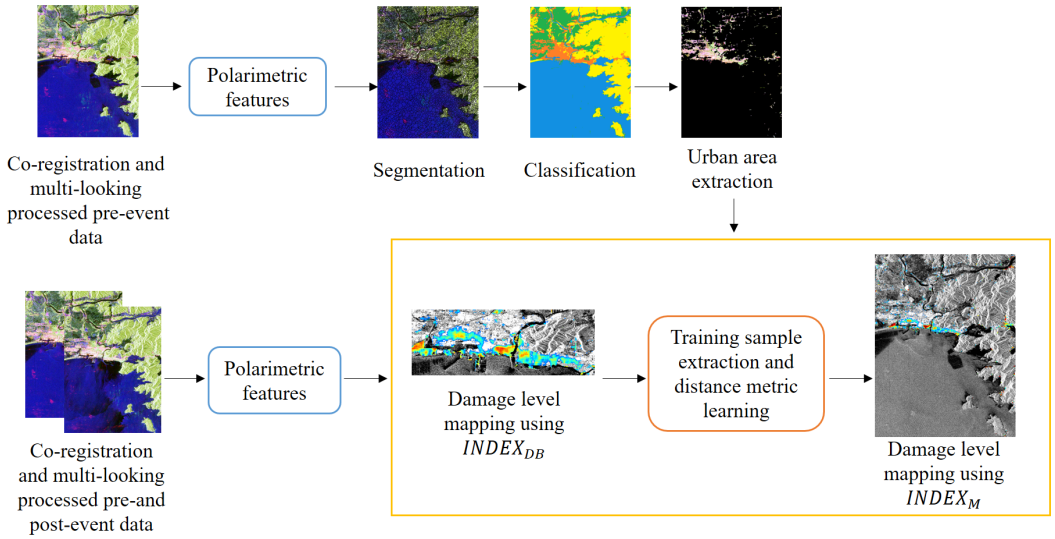

Figure 4.3: Flowchart of the damage level calculation method.

mentation [89]. Acquired segmented regions are the inputs of SVM classifier [90, 91]. With the classification result by the SVM classifier, urban areas can be extracted by picking out the urban labeled pixels. The above procedure is conducted on pre-disaster data while following damage level calculation processing is using both post- and pre-disaster image. Principle for this algorithm is to analyze the features' change created by the disaster. For this work, an index that is using the double-bounce scattering is introduced to get a preliminary result. Training samples are extracted from this preliminary result, and the DML algorithm is used for Mahalanobis metric calculation. A new index under the acquired metric is proposed, it can give a commendable exhibition about damage condition.

4.3.1 Urban area extraction

Urban area extraction is the first work to do. Based on the single pre-event PolSAR image, a region-based classification method is employed. The multiresolution segmentation algorithm [89] is conducted firstly to acquire segmented regions, by which the calculation time and the influence of speckle noise can be reduced.

Figure 4.4 (a) and (b) exhibit the two segmentation results. 10495 segmented regions are obtained from the pre-event image. The black lines in subfigure (a) are the

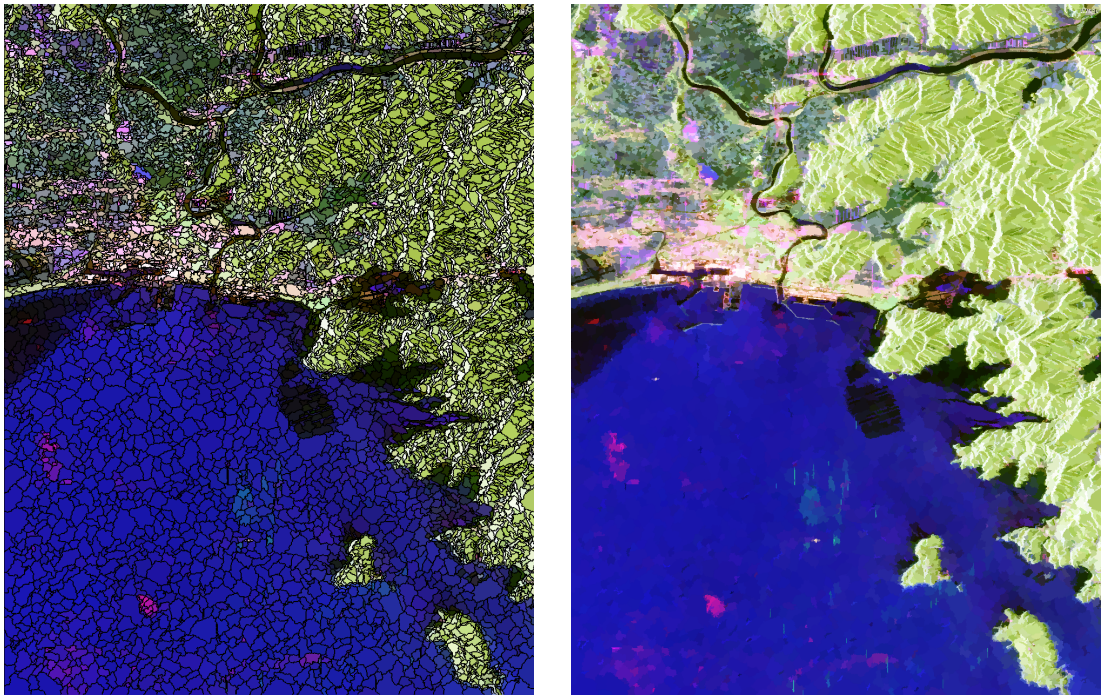

(a) (b)

Figure 4.4: Segmentation results. (a) Result with boundaries; (b) Result presented by average color.

segmentation boundaries. Subfigure (b) gives the average color of segmented regions.

The input for segmentation step is the color features of pre-event PolSAR PauliRGB image, while for classification processing, the classification features' average value of every segmented region serves as the test dataset of Support Vector Machine (SVM) classifier. Features from Cloude-Pottier and Yamaguchi decomposition, and color features [92] extracted from PauliRGB image are used as classification features. The training dataset for the SVM classifier is extracted by visually comparing the Google Earth image and the pre-event image. The whole image is classified into four classes, and for each category, 500 training pixels are selected. After training model is formed, the pre-event PolSAR image is classified by assigning a suitable class label to every segmented region.

The four classes for the study area are the urban area, mountain, farmland, and ocean. Figure 4.5 (a) exhibits the classification result, while Figure 4.5 (b) is a map about all the urban areas, it is created based on the pre-event image. This urban area map shows that

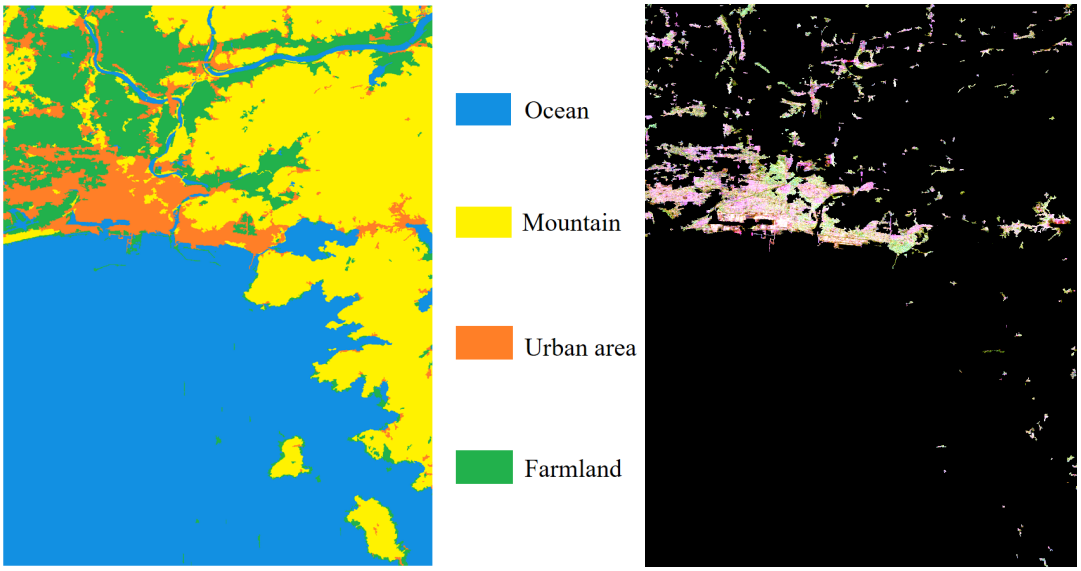

(a) Classification result (b) Urban area map

Figure 4.5: Classification result and urban area map.

the proposed urban area extraction algorithm can extract most urban labeled pixels. The following procedure will only be conducted on the extracted pixels showed in Figure 4.5 (b).

4.3.2 Ground truth damage level map

Building damage map created by Tohoku University [93] is employed to provide ground-truth information. Figure 4.6 (a) shows this map. It exhibits damaged buildings' location which colored with red. The survived buildings are marked with blue color. Other than that, the gray points show the flooded area. However, the information given by this map is insufficient, the damage levels cannot be figured out. Therefore, another reference map about damage levels should be made.

The new damage level reference map is created based on the building damage map. As the first step, the original building damage map is segmented into eighty blocks, it is implemented based on streets' distribution and buildings' shape. Percentage of damaged building pixels to the whole building pixels for each segmented region is regarded as the damage level. Four damage degrees are further defined by classifying these damage levels with values as $\leq 30\%$, $30\% - 50\%$, $50\% - 70\%$, and $\geq 70\%$ into no damage

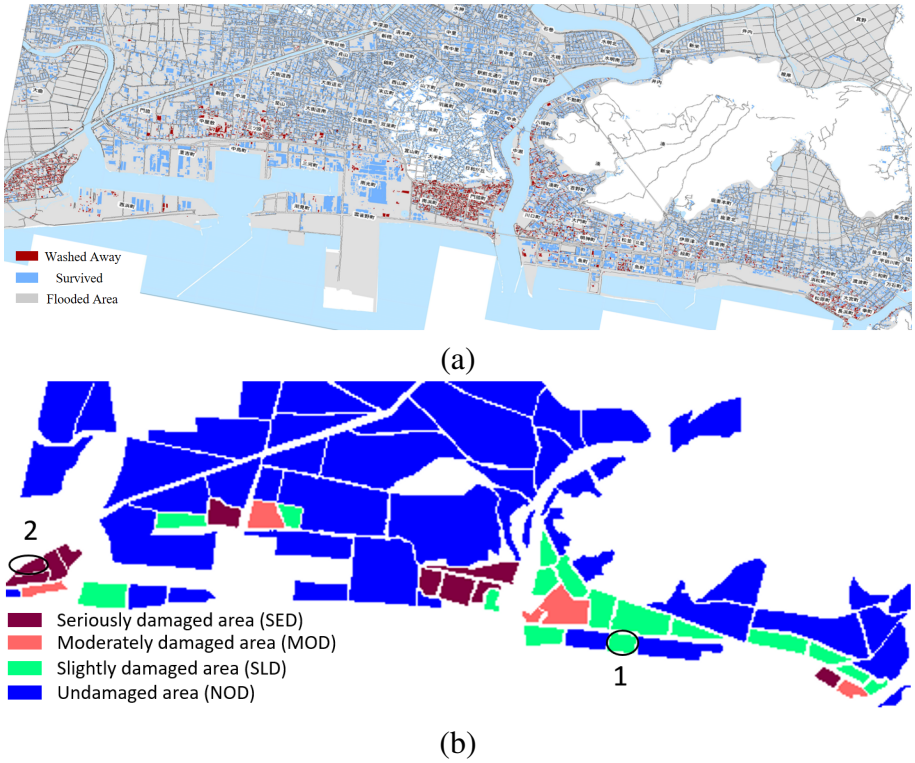

Figure 4.6: (a) Ground-truth building damage map. (b) Reference damage level map.

(NOD), slight damage (SLD), moderate damage (MOD), and serious damage (SED), respectively. Figure 4.6 (b) is graphed damage degree map. It will be used to provide reference information to evaluate damage level mapping result.

4.3.3 Index under double-bounce scattering power

Double-bounce scattering power has been verified as valid parameter for damage evaluation by several previously done studies [43–45, 94]. It relates to the ground-wall structures which will be destroyed when the building is damaged by the disaster. It leads to the left debris under random orientation. Range of P_d shall be different for buildings in different shapes or under different SAR flight directions. Its change value that before and after the event can not be directly used to represent damage level. The damage level index should consider the pre-event value as well as the change value. Based on this assumption, the index using double-bounce scattering power ($INDEX_{\mathrm{DB}}$) is defined as follows,

$$INDEX_{\mathrm{DB}} = \frac{\mid P_{\mathrm{d(pre\text{-}event)}} - P_{\mathrm{d(post\text{-}event)}} \mid}{P_{\mathrm{d(pre\text{-}event)}}} \tag{4.1}$$

where $INDEX_{\mathrm{DB}}$ means the damage level, $P_{\mathrm{d(post\text{-}event)}}$ and $P_{\mathrm{d(pre\text{-}event)}}$ are values of post- and pre-event double-bounce scattering power, respectively. For the reason that there exist nearly no ground-wall structures in the urban areas which are completely damaged, thus, value of $P_{\mathrm{d(post\text{-}event)}}$ should be near to 0, and $INDEX_{\mathrm{DB}}$ should be near to 1. As to undamaged buildings, because of no building structures are damaged, the decrease value of double-bounce scattering power should be close to 0. It leads to the result that $INDEX_{\mathrm{DB}}$ should be near to 0. Above all, the range of this index should be $0 \leq INDEX_{\mathrm{DB}} \leq 1$.

To verify the above discussion, two regions are selected (as shown in Figure 4.6 (b)). Table 4.1 presents the pre- and post-event change value, average value, and the result calculated by $INDEX_{\mathrm{DB}}$ using double-bounce scattering power for these two regions.

Table 4.1: The pre-event, post-event, change and $INDEX_{\mathrm{DB}}$ value of the two test regions.

Regions	GT	$P_{\mathrm{d(post\text{-}event)}}$	$P_{\mathrm{d(pre\text{-}event)}}$	$P_{\mathrm{d(pre\text{-}event)}} - P_{\mathrm{d(post\text{-}event)}}$	$INDEX_{\mathrm{DB}}$
1	SLD	0.3229	0.5863	0.2634	0.4493
2	SED	0.0589	0.2527	0.1938	0.7669

Figure 4.6 (b) shows that region 1 should be labeled as slightly damaged area, and region 2 is seriously damaged region. But when only change value is taken into consideration, region 1's damage level is more serious than that of region 2. It is because the pre-event value of region 1 is much larger than that of region 2. The damage level of region 2 is 0.7669 by the index that calculates the percentage of changed value. This level is larger than that region 1, which should be real damage situation.

Figure 4.7 (a) exhibits the damage level result by $INDEX_{\mathrm{DB}}$. Its background image is the pre-event SPAN image. Before damage level calculation, a 9×9 mean value filter is employed on the two data to reduce the interference of noise. Compared with reference map (Figure 4.6 (a)), this calculated index can interpret damage situation successfully. However, bottom right corner area should be damaged, and $INDEX_{\mathrm{DB}}$ failed

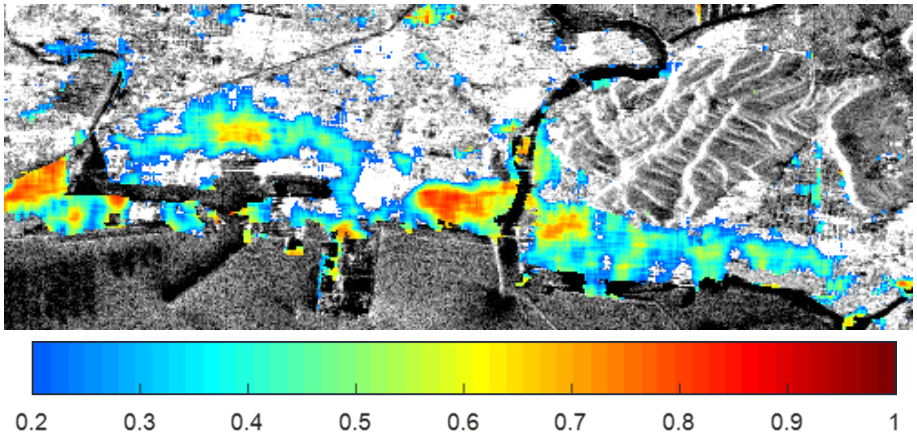

(a)

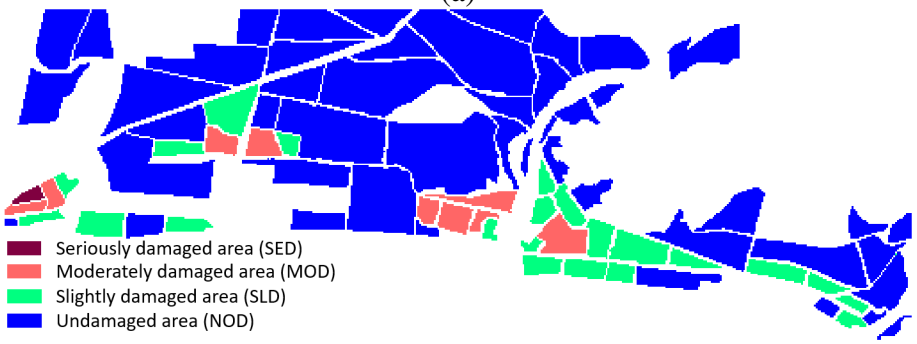

(b)

Figure 4.7: (a) Damage level map by $INDEX_{\mathrm{DB}}$; (b) Damage degree map.

to detect it out. Otherwise, most seriously damaged areas' damage levels are not accurate enough according to the reference map.

A damage level assessment map shown as Figure 4.7 (b) which is in block scale, is created to better evaluate the result. Figure 4.7 (a) that shows damage level in pixel scale is segmented into 80 blocks in the same way as the reference map in Figure 4.6 (b). Every block's average damage level is calculated, and the result is further categorized into 4 damage degrees. Its principle is the same as that of the reference map (Figure 4.6 (b)). The damage degree map is shown as Figure 4.7 (b). It indicates that damage degrees for NOD and SED areas are accurate. But many SED regions are labeled as MOD, which leads to grave errors among these two categories. Above all, accurate damage level result cannot be obtained by $INDEX_{\mathrm{DB}}$.

4.3.4 An improved damage level index

An improved damage level index is introduced in this section. Distance metric learning (DML) [80, 81] is a kind of data conversion method. Large margin nearest neighbor (LMNN) [95] is employed here to obtain improved index. LMNN is a supervised method, its logic is to make samples labeled the same closer; on the other hand, it will push the pixels in different classes further apart. For damage information detection work, each pair of pre- and post-event pixels that represent for damaged buildings should be labeled with different classes. It is because the disaster already changed their polarimetric scattering mechanisms. For the pair of pixels that represent for undamaged buildings, their class labels should be the same. The proposed index is to evaluate the distance of these pairs of pixels. By introducing the DML method, $INDEX_{\text{DB}}$ will be improved, and it can better quantify the damage level for SED areas.

LMNN method is learn a Mahalanobis metric using the following equation,

$$\mathcal{D}_{\mathbf{M}}(\boldsymbol{x}_i, \boldsymbol{x}_j) = \|\boldsymbol{x}_i - \boldsymbol{x}_j\|_M^2 = (\boldsymbol{x}_i - \boldsymbol{x}_j)^T \mathbf{M} (\boldsymbol{x}_i - \boldsymbol{x}_j) \tag{4.2}$$

where $\boldsymbol{x}_i \in R^d$ means the ith pixel, d features are extracted for it. $\mathcal{D}_{\mathbf{M}}(\boldsymbol{x}_i, \boldsymbol{x}_j)$ represents the squared distance of pixel $\boldsymbol{x}_i$ and $\boldsymbol{x}_j$ under the Mahalanobis metric. For pixel $\boldsymbol{x}_i$ whose class label is y_i, its target neighbors mean the k closest neighbor pixels that labeled same. $j \rightsquigarrow i$ represents that $\boldsymbol{x}_j$ is a target neighbor of $\boldsymbol{x}_i$. $y_{ij} \in \{0, 1\}$, it means that the value of y_{ij} is 1 for same labeled pixels $\boldsymbol{x}_i$ and $\boldsymbol{x}_j$, and $y_{ij} = 0$ means their labels are different.

For the training procedure, a Mahalanobis metric is trained using loss function below. One term of this function is to pull the same labeled targets closer, the second term will push the differently labeled targets further apart.

$$\begin{aligned} \varepsilon(\mathbf{M}) =& (1-\mu) \sum_{i, j \rightsquigarrow i} \mathcal{D}_{\mathbf{M}}(\boldsymbol{x}_i, \boldsymbol{x}_j) + \mu \sum_{i, j \rightsquigarrow i} \sum_{l} (1 - y_{il}) \\ & [1 + \mathcal{D}_{\mathbf{M}}(\boldsymbol{x}_i, \boldsymbol{x}_j) - \mathcal{D}_{\mathbf{M}}(\boldsymbol{x}_i, \boldsymbol{x}_l)]_+ \end{aligned} \tag{4.3}$$

where $[z]_+ = max(z, 0)$. The minimizing processing can be conducted by using a semi-positive programming algorithm and introducing a slack variable.

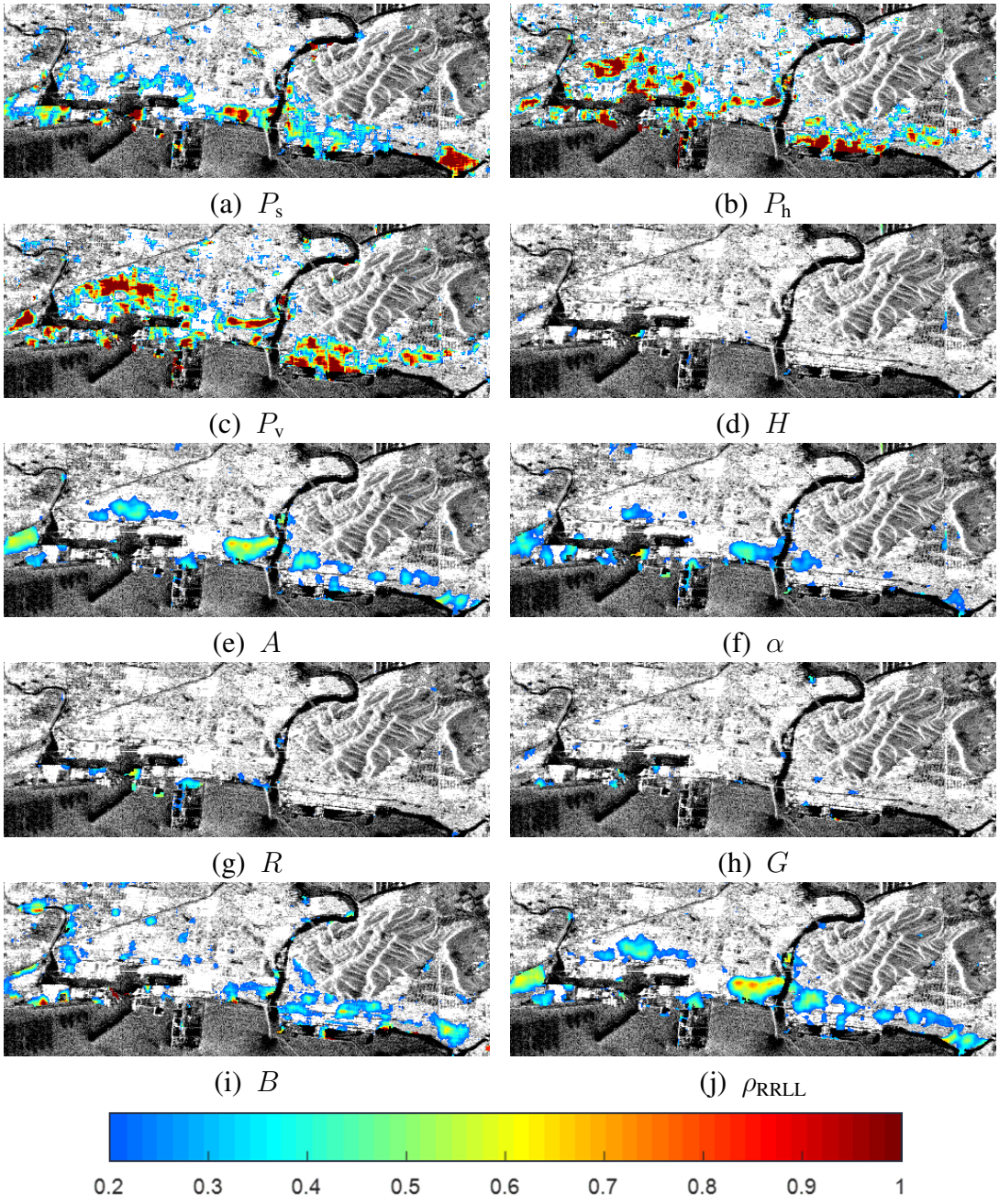

Figure 4.8: Results by $INDEX_P$. (a)-(c) are the results using P_s, P_h, and P_v, respectively; (d)-(f) are the results using H, A, and α, respectively; (g)-(i) are the results using color features R, G, and B, respectively; (j) is the result using ρ_{RRLL}.

After DML algorithm is introduced, the original $INDEX_{DB}$ is improved. It is the

multi-features based index shown as follows,

$$INDEX_{\mathrm{M}} = \frac{\| \boldsymbol{V}_{\text{(post-event)}} - \boldsymbol{V}_{\text{(pre-event)}} \|_M}{\| \boldsymbol{V}_{\text{(pre-event)}} \|_M} \tag{4.4}$$

where $V_{\text{(post-event)}}$ and $V_{\text{(pre-event)}}$ mean post- and pre-event feature vectors, respectively. Numerator of this function is their distance when Mahalanobis metric is employed.

Feature vectors for $INDEX_{\mathrm{M}}$ should be composed by several effective features that can interpret damage information. Damage level map by $INDEX_{\mathrm{DB}}$ indicates that P_d is a valid feature. Thus, it is one of the features for $INDEX_{\mathrm{M}}$. A series of experiments are conducted to explore more valid features. Four-component decomposition features (P_{s}, P_{h} and P_{v}), circular correlation coefficient (ρ_{RRLL}), Cloude-Pottier decomposition features (H, A and α), and color features (R, G and B) are tested by using $INDEX_{\mathrm{P}}$.

$$INDEX_{\mathrm{P}} = \frac{\mid P_{\text{(post-event)}} - P_{\text{(prec-event)}} \mid}{P_{\text{(pre-event)}}} \tag{4.5}$$

where $P_{\text{(post-event)}}$ and $P_{\text{(pre-event)}}$ represent the tested post- and pre-event parameter, respectively.

Figure 4.8 indicates the damage level results by 10 polarimetric features. Among all these results, maps by P_{s}, A, and ρ_{RRLL} can better identify damaged buildings. For the reason that buildings were totally damaged by the tsunami, leaving the empty ground, surface scattering P_{s} increased after the disaster event. Anisotropy A can detect out scattering characters' change. For damaged areas, the increase of surface roughness leads to that the circular correlation coefficient ρ_{RRLL} values of damaged buildings are smaller than those of undamaged buildings. It means ρ_{RRLL} is also a valid parameter. These damage level mapping results show that even though the SED areas can be detected, the damage levels are not accurate according to the reference map. In the following experiments, the improved damage level index $INDEX_{\mathrm{M}}$ will be tested. These valid features, P_{d}, P_{s}, A, and ρ_{RRLL} will be employed to create the feature vectors.

4.4 Results and discussions

The training dataset for LMNN can be extracted from the result by $INDEX_{\mathrm{DB}}$. For this training processing, a Mahalanobis metric can be calculated.

The location of the extracted training data is shown in Figure 4.9 (region 2, 3, and 6). 100 pixels exist in every region. Region 6 should be undamaged, and region 2 and 3 should be damaged. Table 4.2 lists the class labels for these pixels.

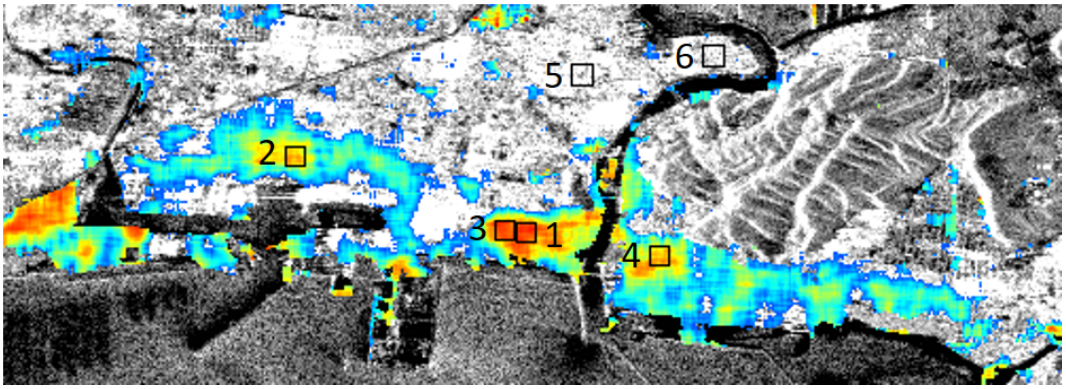

Figure 4.9: Location of test data (region 1, 4, 5) and training data (region 2, 3, 6).

Labels of pairs of pre- and post-event pixels for damaged regions shall be different, those of pairs of pixels for undamaged areas should be the same. Therefore, both the pre- and post-event pixels in region 6 are labeled as '0', and pre-disaster pixels in region 2 and 3 should be '0'. Meanwhile, post-event pixels in region 2 and 3 are labeled as '1'.

Table 4.2: Labels for training samples.

Data	Label
Pre-event pixels in region 6	0
Post-event pixels in region 6	0
Pre-event pixels in region 2 and 3	0
Post-event pixels in region 2 and 3	1

Nonlinear metric learning using gradient boosted regression trees (GB-LMNN) [96] is introduced here. Figure 4.10 (a) shows the result by $INDEX_{\mathrm{M}}$. All damaged regions can be detected, including the bottom area that discussed earlier. The calculated damage

levels for SED areas are increased when compared with the result of $INDEX_{\mathrm{DB}}$. The results for NOD and SLD regions are almost the same by these two indexes. Damage level assessment map (damage degree map) that created according to the reference map is shown in Figure 4.10 (b). It indicates that most regions are labeled with the right damage degree.

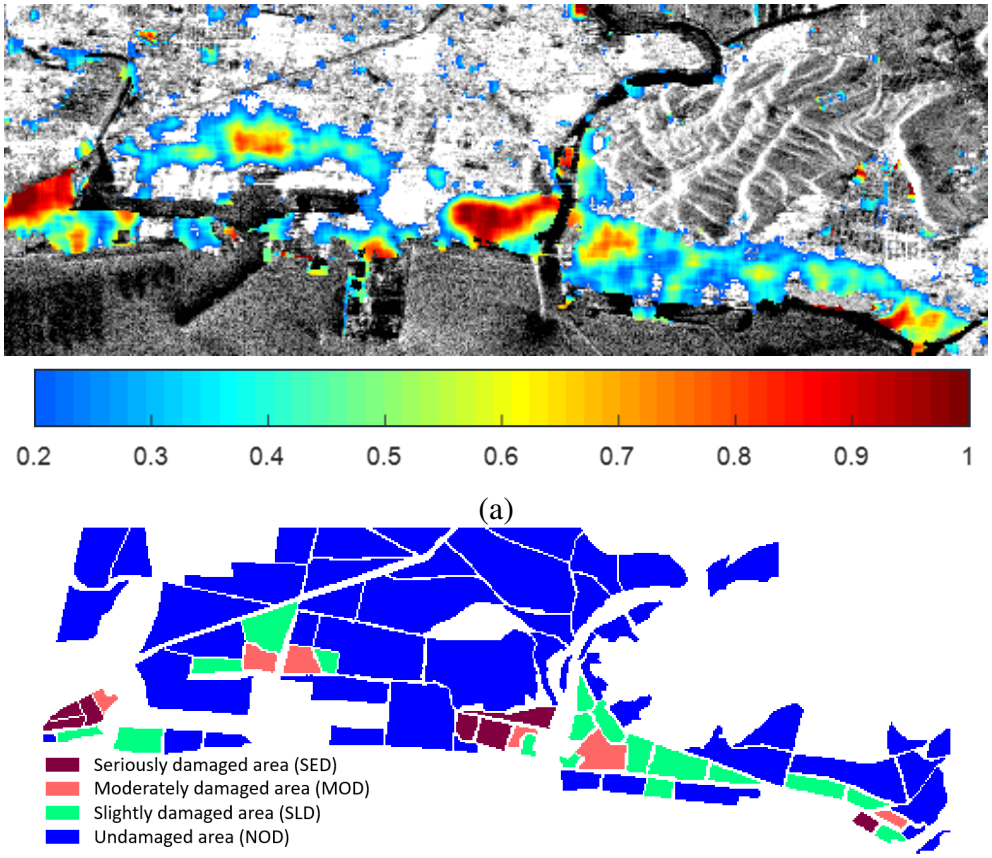

Figure 4.10: (a) Damage level result by $INDEX_{\mathrm{M}}$; (b) Damage degree map.

The damage degree accuracy of the results by the damage level index $INDEX_{\mathrm{DB}}$ and $INDEX_{\mathrm{M}}$ is evaluated, and Table 4.3 shows the results. The total number of error labeled blocks in the result by $INDEX_{\mathrm{DB}}$ is 17, and they are mainly labeled as SED. For all the SED blocks in the study area, 7 of them are mislabeled as MOD. Several error regions also exist in the damaged areas that under other three damage degrees. For example, 4 NOD regions are labeled as SLD. Only 10 blocks are wrongly labeled in the result by $INDEX_{\mathrm{M}}$, and the damage degree accuracy is improved. Error regions for

Table 4.3: Damage assessment accuracy for $INDEX_{\text{DB}}$ and $INDEX_{\text{M}}$.

		$INDEX_{\text{DB}}$				$INDEX_{\text{M}}$			
		SED	MOD	SLD	NOD	SED	MOD	SLD	NOD
		(NO. of Blocks)							
Damage degree (Ground Truth)	SED	1	7	1	1	7	3	0	0
	MOD	0	2	3	0	0	2	3	0
	SLD	0	0	15	1	0	1	13	2
	NOD	0	0	4	45	0	0	1	48
		Overall Accuracy: 92.23%				Overall Accuracy: 95.52%			

SED areas are reduced to 3 blocks, for NOD areas, only one error labeled region exists. The overall accuracy is also shown in the Table. It is the result by comparing every pixel's damage degree with those in the ground-truth map (Fig. 4.6 (b)). By introducing a Mahalanobis metric, the overall accuracy is improved from 93.23% to 95.52%.

As discussed earlier, the feature vectors in $INDEX_{\text{M}}$ are composed of several valid features. Thus, the improvement by using $INDEX_{\text{M}}$ may because of the usage of Mahalanobis metric or come from the combination of valid features. Therefore, the effectiveness of introducing the distance metric learning method should also be tested. For this purpose, a comparison experiment between the multi-features based results under Euclidean and Mahalanobis metric is also implemented. The damage level index that under Euclidean metric is shown as follows,

$$INDEX_{\text{E}} = \frac{\|V_{\text{(post-event)}} - V_{\text{(pre-event)}}\|_2}{\| V_{\text{(pre-event)}}\|_2} \tag{4.6}$$

The numerator of this equation means the distance of post- and pre-event feature vectors under Euclidean metric. 3 datasets are chosen to test the performance of $INDEX_{\text{M}}$ and $INDEX_{\text{E}}$. Their locations are shown in Figure 4.9, and they are labeled as 1, 4, and 5. Region 1 and 4 should be damaged regions, and area 5 is undamaged. Mahalanobis metric for $INDEX_{\text{M}}$ is the one by training the samples in region 2, 3, and 6.

Figure 4.11 shows the damage level results by $INDEX_{\text{M}}$ and $INDEX_{\text{E}}$ for these six regions, respectively. Test data in region 1, 4, and training data in region 2, 3 are

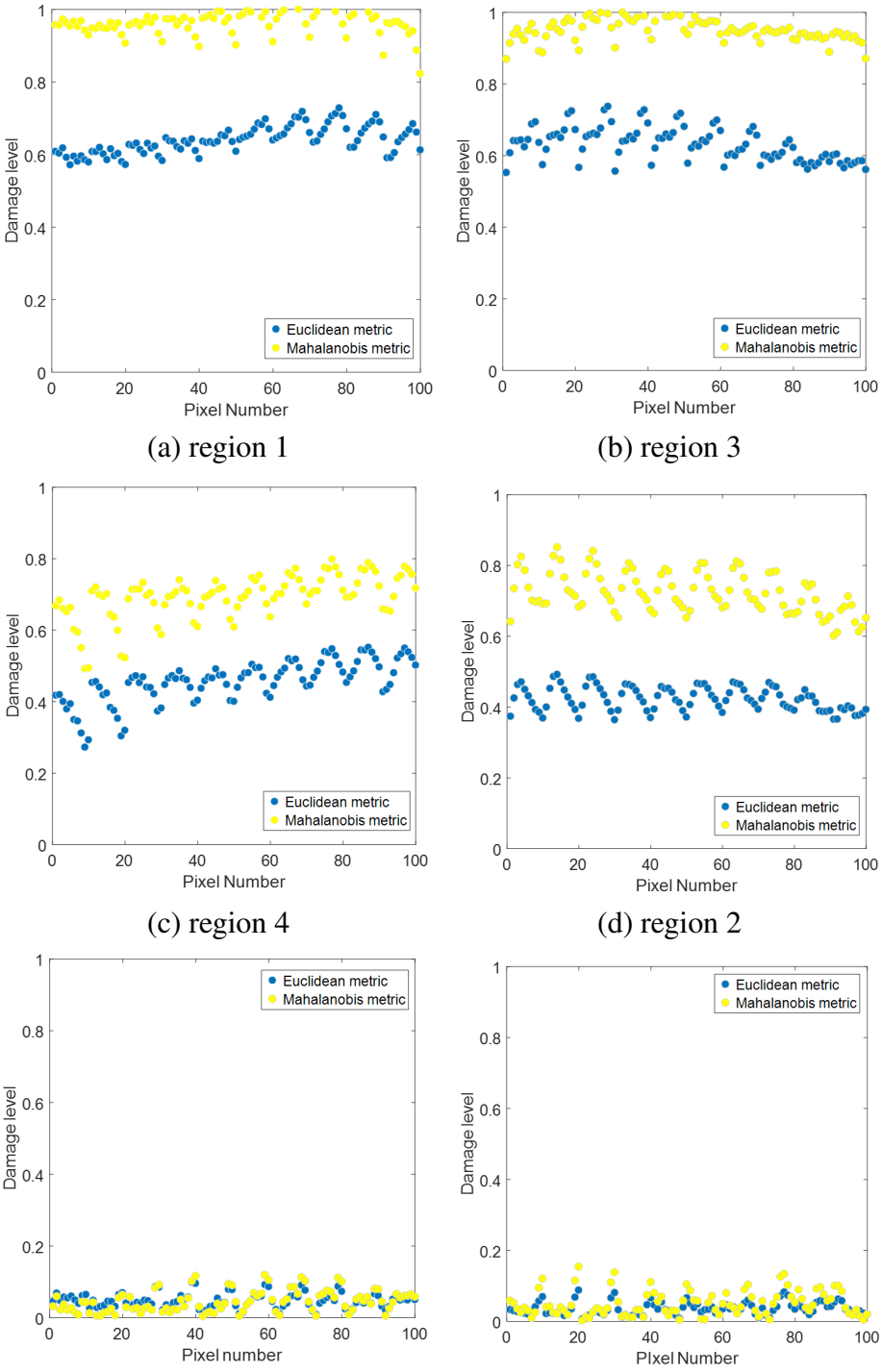

Figure 4.11: Damage levels of test and training datasets under Euclidean metric and Mahalanobis metric.

damaged, their calculated damage levels under Euclidean metric are smaller than those

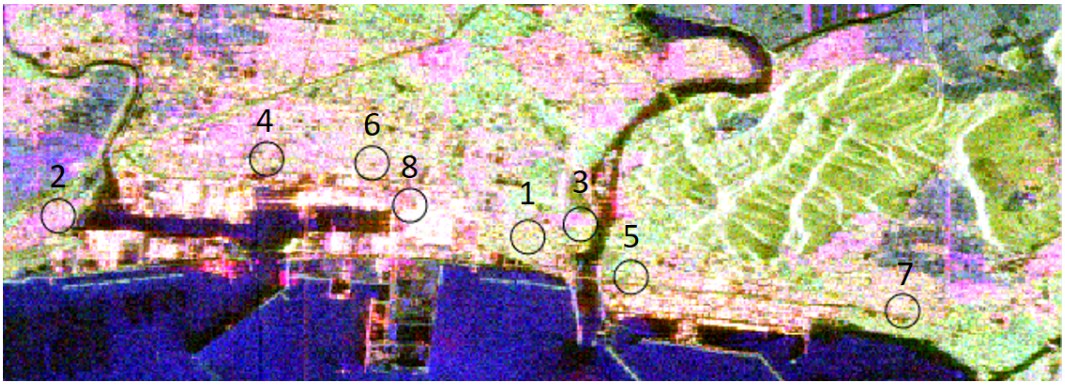

Figure 4.12: Location of the chosen areas for result assessment.

by Mahalanobis metric. As can be known according to the reference map (Figure 4.6 (b)), SED should be the accurate degree for region 1 and 3, and degree for region 2 and 4 is MOD. According to the distributions of damage levels presented in Figure 4.11, index by Mahalanobis metric can obtain a much better result than that under the Euclidean metric. For the undamaged samples in region 5 and 6, their results under different metric are almost the same, both of them are smaller than 20%. The analysis above indicates $INDEX_{\mathrm{M}}$ can greatly improve the accuracy, and this improvement is

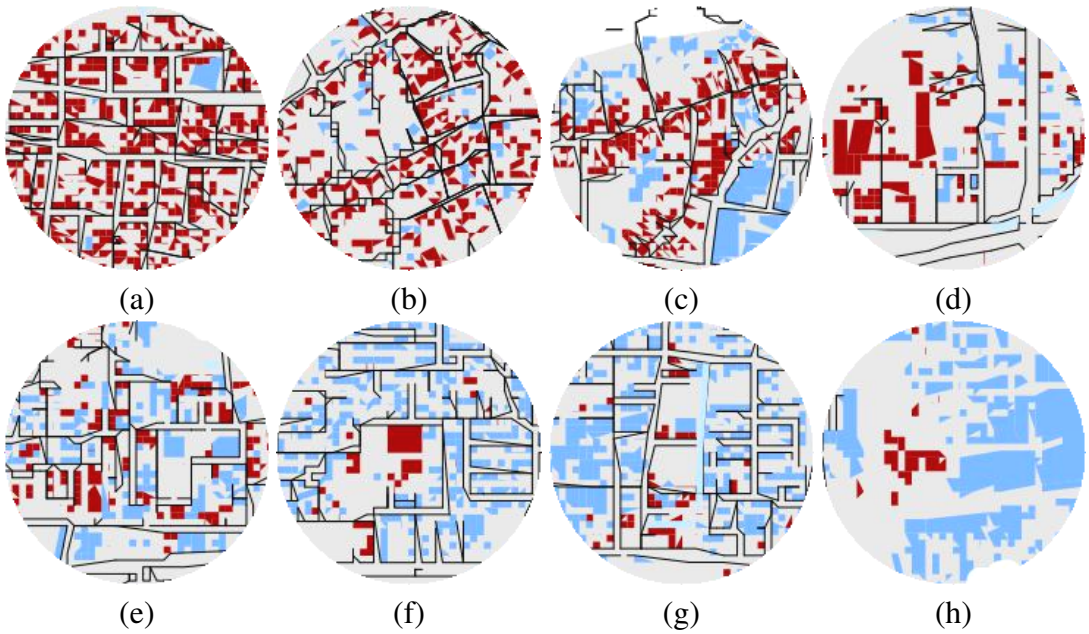

Figure 4.13: The detailed building damage information for the selected eight areas .

because of the employment of DML theory.

The above damage level assessment map (damage degree map) can estimate the results. But this is about the damage degree instead of levels. To better evaluate the damage level results, the experiment that evaluates damage levels is implemented. The PolSAR dataset is in different scale with reference map (Figure 4.6 (a)). Moreover, the sign on the reference map would interfere the assessment, therefore, the accuracy of the damage level for every urban area pixel cannot be evaluated. To solve this problem, typical regions are selected to estimate the relationship of obtained results and the truth levels. Figure 4.12 presents the location of these regions. Figure 4.13 exhibits the corresponding truth damage information that tailored from Figure 4.6 (a). The true damage levels for region 1-8 are 95%, 85%, 70%, 65%, 55%, 40%, 30% and 20%, respectively.

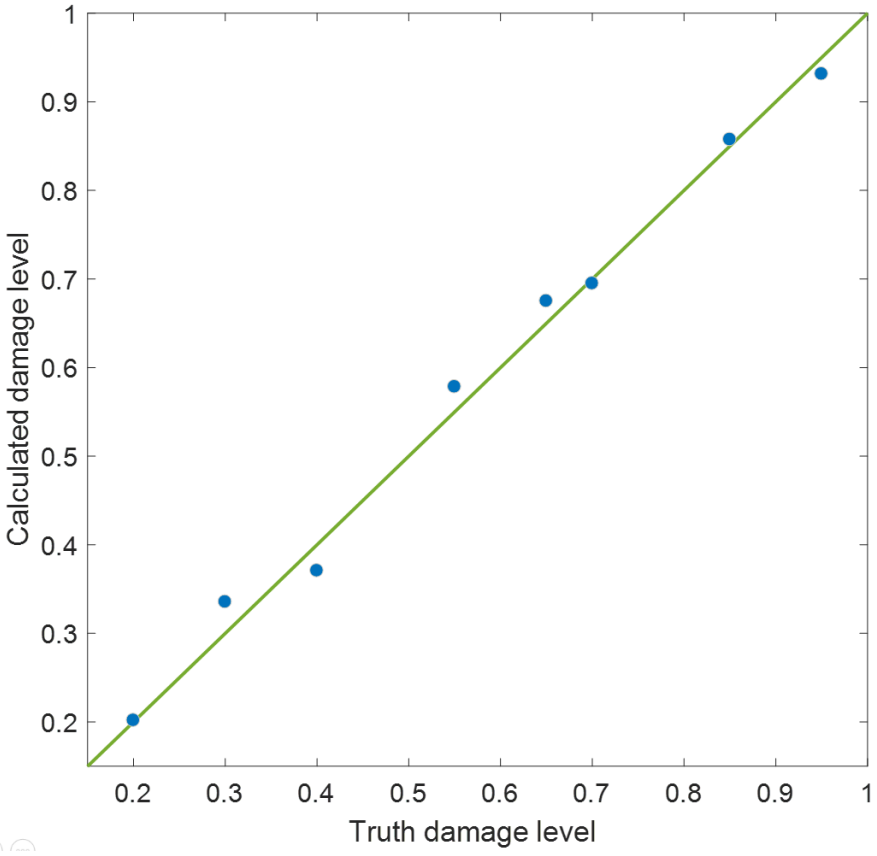

Figure 4.14: Linear fitting of the obtained results with reference information.

The relationship between the result by $INDEX_{\mathrm{M}}$ and truth values for these selected

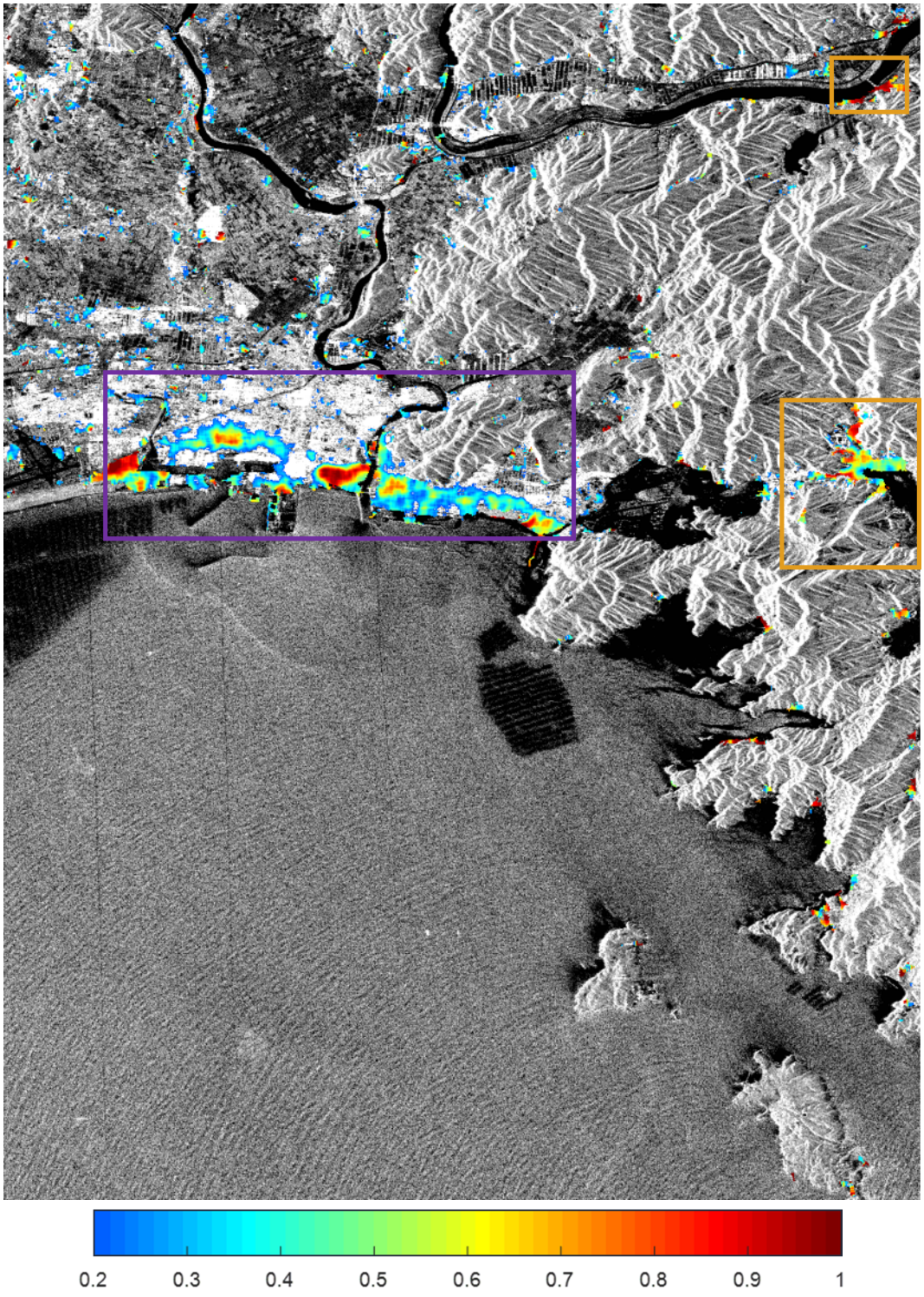

Figure 4.15: The damage level result by $INDEX_{\mathrm{M}}$. The Ishinomaki city is marked with purple rectangle box. The areas in the orange rectangle are the river area of Ishinomaki city and Onagawa Town, respectively.

eight regions is shown as Figure 4.14. The truth value is represented by x axis, and y axis indicates averaged damage level by $INDEX_{\mathrm{M}}$. Figure 4.14 indicates between these two parameters, a linear relationship exists.

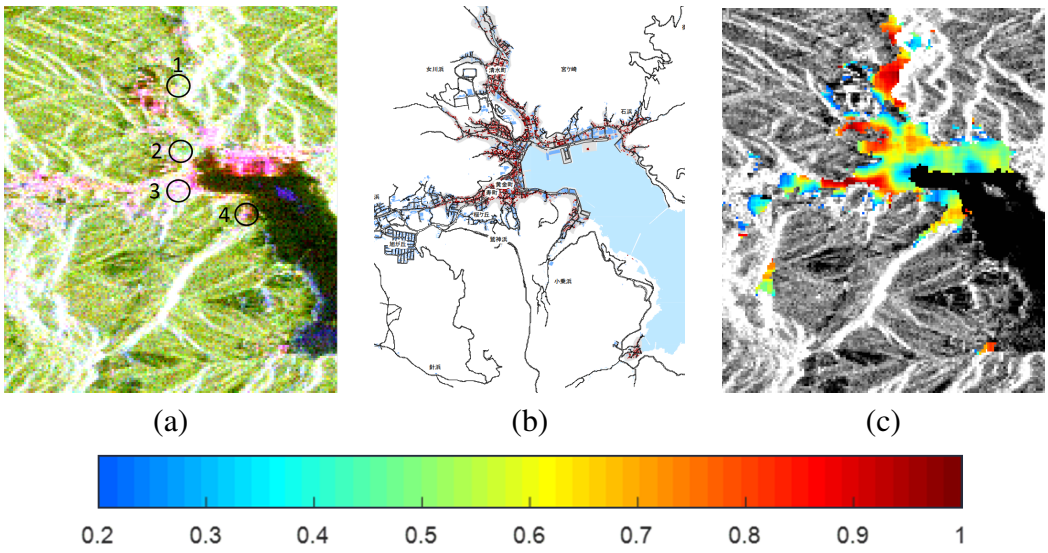

Figure 4.16: The pre-disaster image, reference map, and damage level map for Onagawa Town.

The overall damage result is shown in Figure 4.15. The region marked with the purple rectangle indicates Ishinomaki city. There also exist other two damaged regions, the area near the river in Ishinomaki City and Onagawa Town. Damage information of these two regions is also analyzed in the following discussion.

Damage information maps of Onagawa Town, Miyagi Prefecture, is shown as Figure 4.16. Location of this area is indicated in Figure 4.15. Figure 4.16 (a) presents pre-event image and Figure 4.16 (b) is ground-truth. This ground-truth map indicates most urban regions were damaged, especially buildings near the seashore. The result by $INDEX_{\mathrm{M}}$ is shown as Figure 4.16 (c), it indicates that all damaged areas are detected out, including small areas in the mountains. However, because of the interference of noise, parts of ocean areas are labeled as urban, which leads to the error.

Damage condition about near river region in Ishinomaki City is shown in Figure 4.17. Figure 4.15 indicates its location, which is in the northeast region marked with an orange rectangle box. Figure 4.17 (a) and (b) are pre-disaster image and reference map,

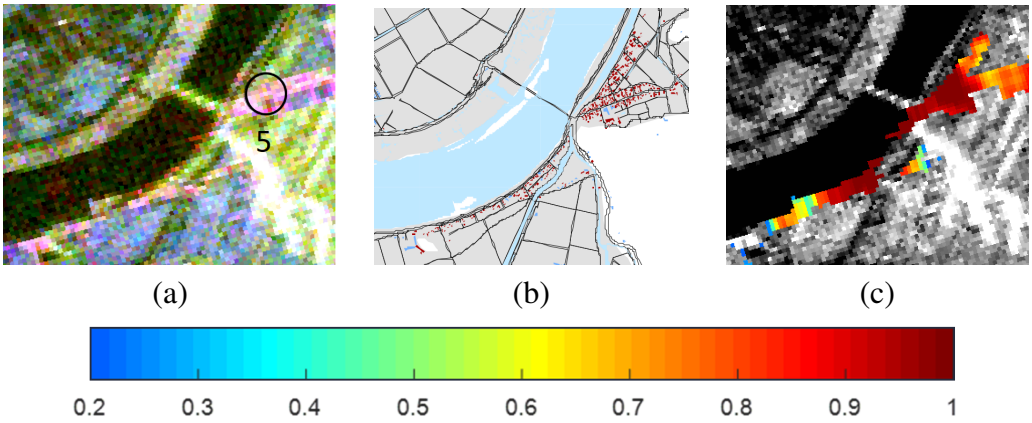

Figure 4.17: The pre-disaster image, reference map, and damage level map of the near river area of Ishinomaki City

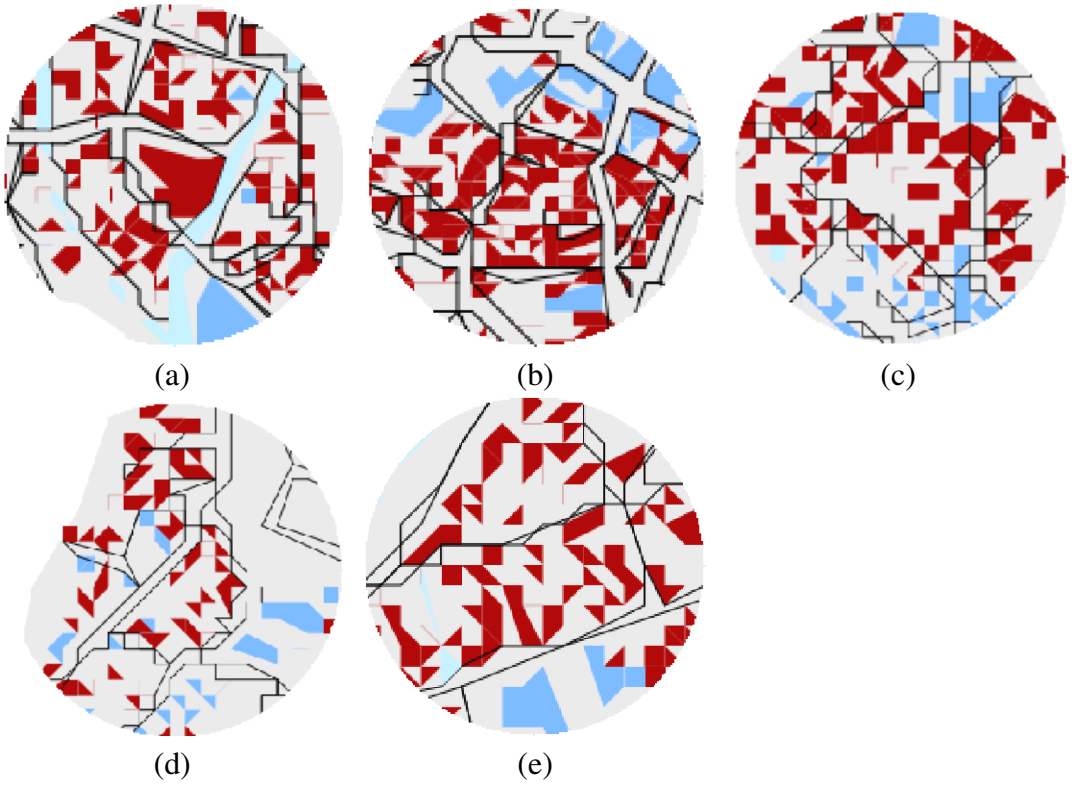

Figure 4.18: The selected regions' building damage map. (a)-(d) are for regions 1-4 in Figure 16 (a); (e) is for the region 5 in Figure 17 (a).

respectively. Severe damage happened along this river area, especially the zone close to the bridge. Figure 4.17 (c) is result by $INDEX_{\mathrm{M}}$, and it shows that serious damage happened for most urban areas.

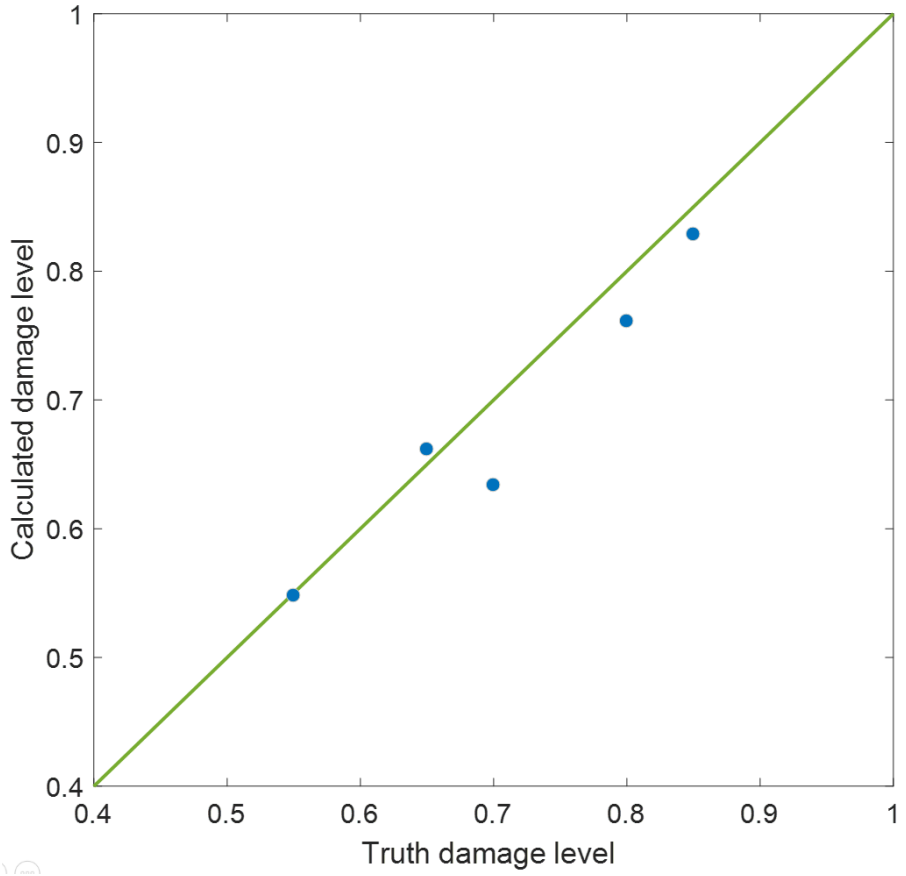

Figure 4.19: Linear fitting of obtained results with true levels.

To test the performance of the obtained result, 5 regions are chosen among these two areas. Figure 4.18 indicates their detailed damage information, and they are tailored from the ground-truth map. True damage levels of these blocks are 85%, 70%, 65%, 55%, 80%, respectively. Figure 4.19 shows the relationship of their truth damage levels and calculated results. It indicates that the results can present the damage situation successfully.

Tohoku earthquake occurred on March 11, 2011, the corresponding post-disaster PolSAR image was obtained on April 8, 2011. When the post-disaster data was acquired, most standing water has receded, it means that the standing water did not effect the damage level calculation.

The proposed damage level mapping algorithm could also be conducted effectively for events with standing water existing in the post-event image. For these two kinds of

damaged urban regions that standing water exists or not, the values of P_{d}, A, and ρ_{RRLL} will decrease, it is due to the destruction of building structures. After the disaster event, surface scattering power value (P_{s}) will increase in the damaged area without standing water. It is because of the totally destroyed buildings will leave the ground empty. For damaged areas that standing water exists, P_{s} will also increase. The reason is that P_{s} can be produced by the water surface.

4.5 Robustness test of the proposed index

The analysis above shows that damage level index $INDEX_{\mathrm{M}}$ can evaluate the urban areas' damage situation for the Tohoku earthquake/tsunami event. However, different damage situations exist in different disaster events. Therefore, the robustness of this proposed index needs to be discussed, and the damage information for Kumamoto earthquake is analyzed.

Kumamoto earthquake happened on April 14, 2016, and its magnitude is 7.0. The study area for this event is around Mashiki-town, Japan. L-band PolSAR datasets are used, and the pre- and post-even PolSAR datasets were obtained by ALOS2 satellite on December 3, 2015, and on April 21, 2016, respectively.

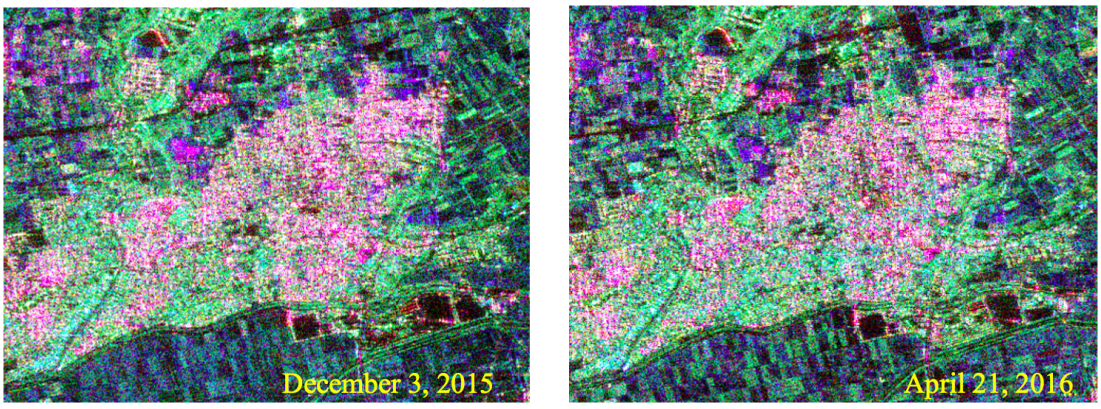

(a) Pre-event (b) Post-event

Figure 4.20: Pre- and post-event PauliRGB images for Mashiki-town (after pre-processing)

Pre- and post-event PauliRGB images for Mashiki-town are presented as Figure 4.20. Co-registration processing and multi-looking (two-looking) are conducted for

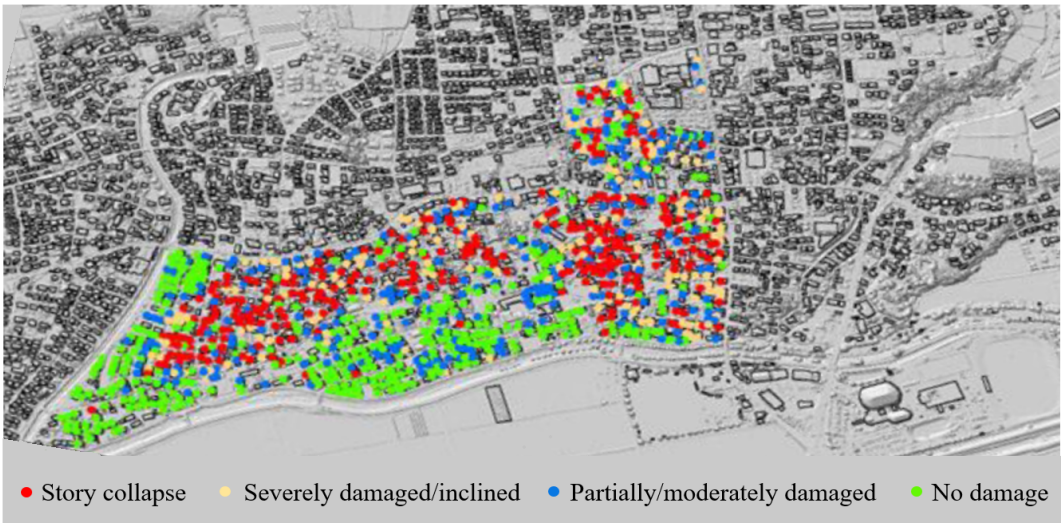

Figure 4.21: Reference map

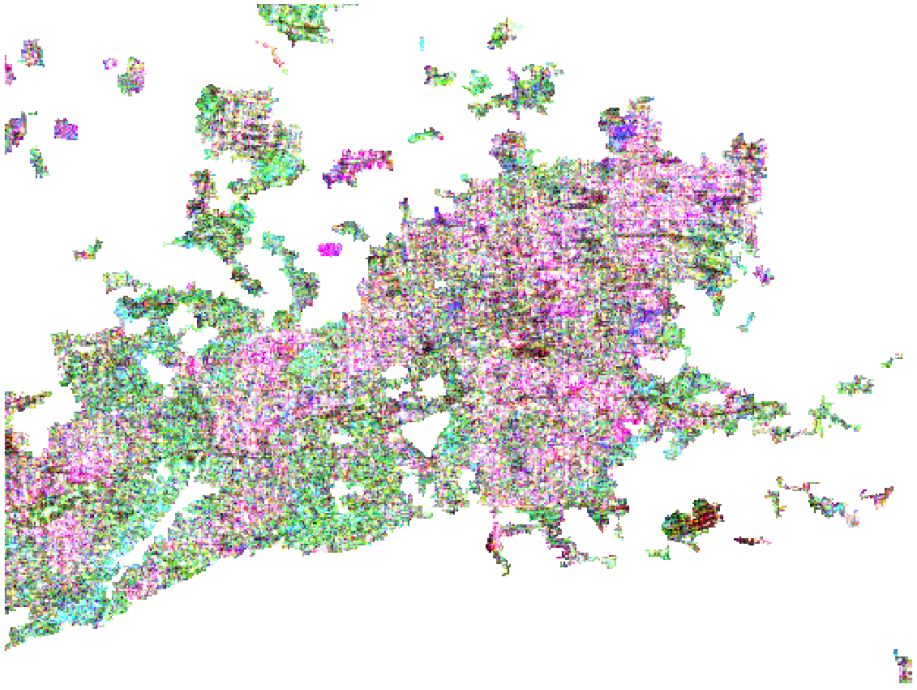

Figure 4.22: Urban area extraction result

these two datasets. The damage situation of Mashiki-town is different from that of Ishinomaki city. For Tohoku earthquake/tsunami, most buildings near the ocean were flushed away. While for Kumamoto earthquake, the damage situation is not so serious. The ground truth map for parts of the study area is shown as Figure 4.21. It was created by Yamada et al. [97]. All damaged buildings are classified into 4 degrees: no dam-

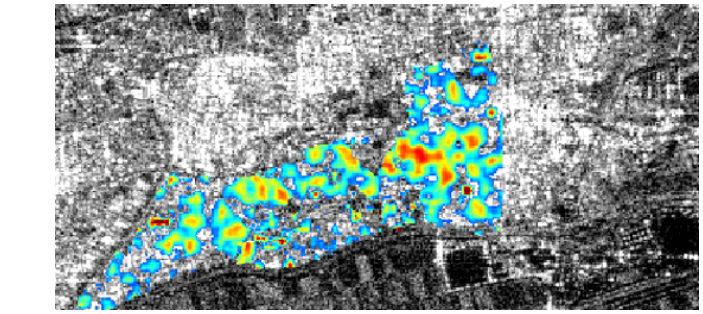

(a) P_{d}

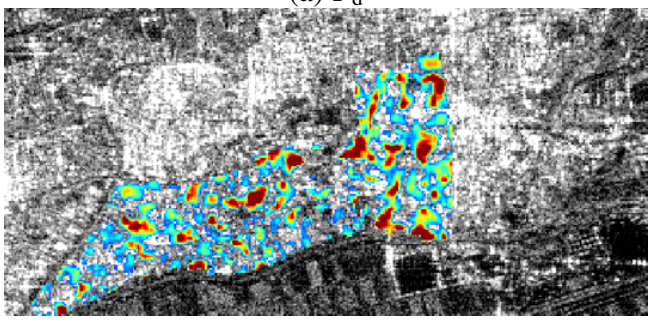

(b) P_{s}

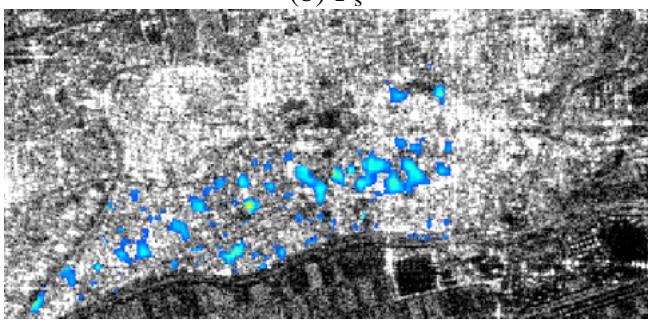

(c) A

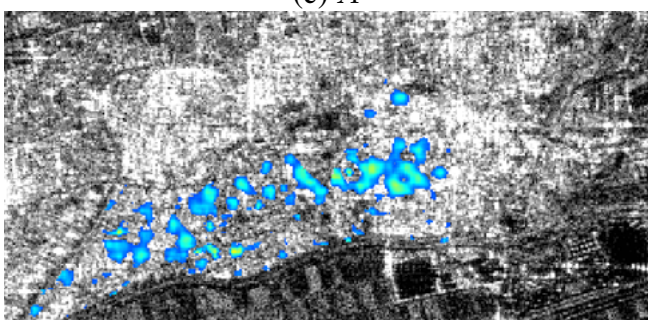

(d) ρ_{RRLL}

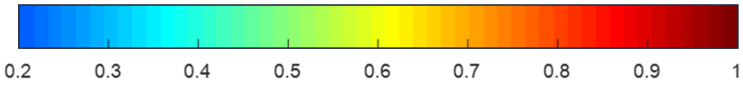

Figure 4.23: Single parameter based damage level mapping results for the area that corresponding ground-truth information exists. (a) result by P_{d}; (b) result by P_{s}; (c) result by A; (d) result by ρ_{RRLL}

age (D0), partially/moderately damaged (D1-D3), severely damaged/inclines (D4), and story collapse (D5), and they are marked with different colors [98]. The reference map indicates the location of the damaged buildings are scattered, and it is different from the

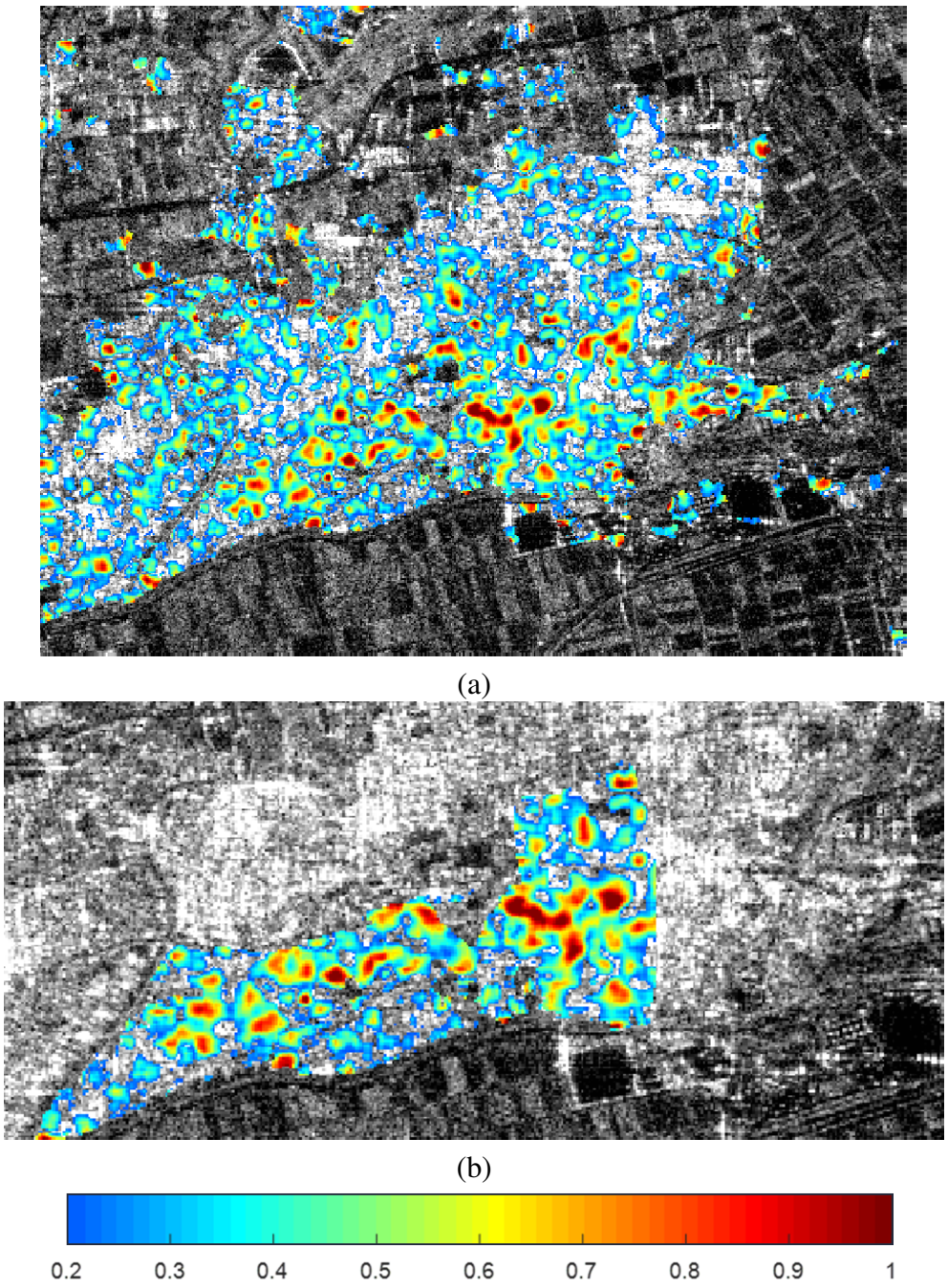

Figure 4.24: Damage level mapping results by the proposed index. (a) result for the whole study area; (b) result of the area with reference information

Tohoku earthquake.

Figure 4.22 is the extracted urban area by the introduced classification method. Figure 4.23 show the single parameter based results by the four valid polarimetric features. They are P_{d}, P_{s}, A, and ρ_{RRLL}. For these four results, only regions that reference information exists are calculated. Among these four results, the one by P_{d} shows the best performance. The similar problem exists for Kumamoto disaster event, it is that the calculated damage levels are not bigger enough, even though the damage level results using these four parameters can effectively detect damaged areas. However, the single parameter based results verify that these parameters P_{d}, P_{s}, A, ρ_{RRLL} are valid for damage assessment.

For Kumamoto earthquake, another training sample extraction method is introduced. Two datasets are grouped according to the result by P_{d}. One is the dataset of undamaged buildings, it can be created by pixels with $INDEX_{\mathrm{DB}}$ is under 0.2. Another one is damaged set, it can be created by the pixels with large $INDEX_{\mathrm{DB}}$, the threshold is 0.6. The training data for DML can be randomly chosen from these two groups. For each class, 200 training samples are selected.

Figure 4.24 (a) is the final result by the algorithm in this chapter, while the result of regions with reference information is presented as Figure 4.24 (b). This acquired result can give a satisfactory description of the damage condition.

4.6 Conclusion

In this chapter, a novel damage level calculation method for earthquake/tsunami happened in urban areas using post- and pre-disaster PolSAR datasets is introduced. This proposed algorithm has been tested by a series of experiments. Except for damaged areas detection, this algorithm can also evaluate the detailed damage levels for urban areas.

The proposed algorithm has been implemented on two kinds of L-band ALOS/ALOS2 PALSAR datasets. The discussion about the experiments shows that the DML algorithm can pull the pair of pre- and post-event pixels that should be undamaged near to each

other and make pair of pixels in damaged regions further apart. Under the Mahalanobis metric, a new index can solve the problem happened for double-bounce scattering power based index. By the improved index, the damage assessment accuracy for the seriously damaged area has been greatly improved. Moreover, for the Tohoku earthquake/tsunami event, the overall accuracy has been increased. The linear relationship between truth values and the obtained results shows that this proposed technique's performance is excellent.

5

Earthquake Damage Assessment using Single Post-event PolSAR Image

5.1 Introduction

In this chapter, a novel unsupervised earthquake/tsunami damage assessment method is proposed. This technique is implemented on the same disaster event as shown in the last section, it is the Tohoku earthquake/tsunami event. For the method introduced in this section, only single post-event PolSAR data is used to acquire damage information,

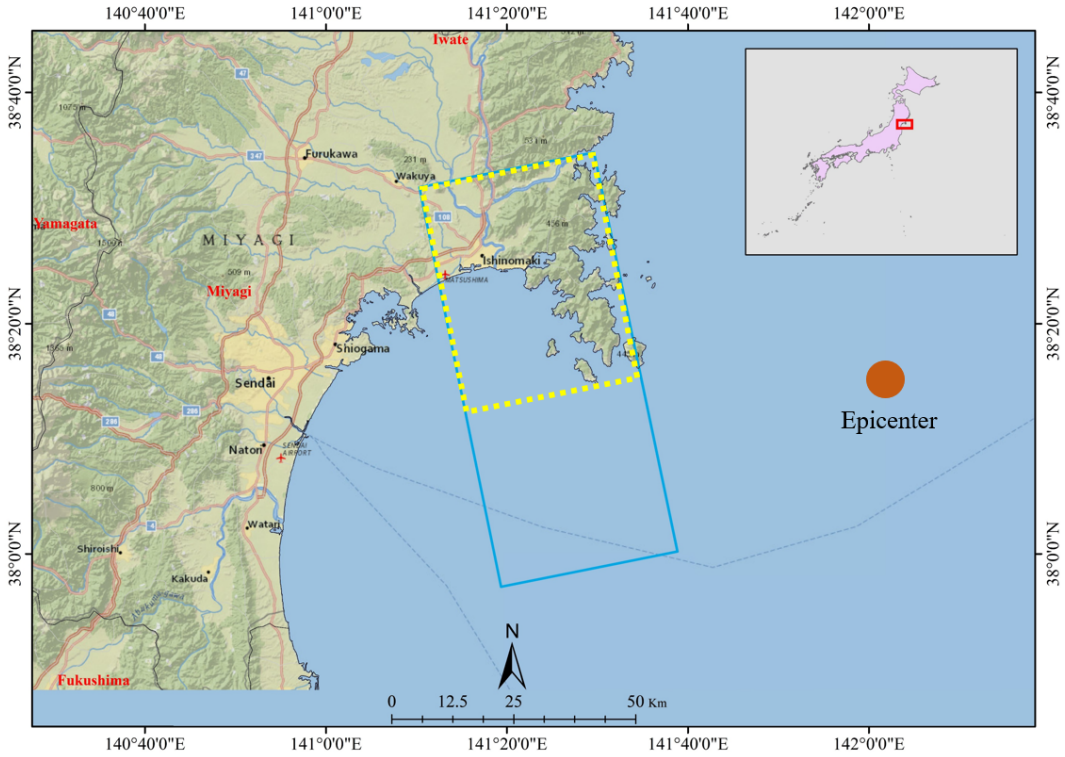

Figure 5.1: Information about Tohoku earthquake. Yellow rectangle indicates the study area.

which is different from the previous work. "Unsupervised" here means that this technique acquires results without reference information. Post-event data about the Tohoku earthquake/tsunami exhibit complex damage situations. The foreshortening mountain areas share similar characters with damaged buildings and oriented buildings, which will cause misclassification in urban area extraction. Moreover, the existing damaged building, which under big orientation angle would be easily recognized as undamaged. Without prior damaged buildings' information, damaged building extraction work for this disaster event is difficult. The proposed technique solves the above problems. For the urban areas extraction work, an improved classification technique is proposed. This improved classification method can better distinguish building areas and foreshortening mountain areas. For the work of detecting damaged buildings, all the buildings are firstly classified into oriented and parallel buildings. After that, the damaged building detection procedure is conducted for each of these two categories. Damaged buildings under large orientation angle are considered. Thus not all oriented building are labeled as undamaged. This proposed damage assessment method can acquire results with high accuracy.

5.2 Study area

The research of new damage assessment algorithm in this chapter is also based on the Tohoku earthquake/tsunami event. Information about this event has been introduced in the last section. Figure 5.1 presents the satellite footprint, the earthquake's epicenter, and the main study area, which is a little different from that in the last section. For preprocessing, multi-looking (eight-look) processing is applied, and Lee refined filter is employed. The preprocessed post-event PauliRGB images are shown as Figure 5.2.

The main study area is the same one that analyzed in the last section. Figure 5.2 shows its location. The ground-truth maps have been introduced in Section 4.3.2 (Figure 4.6 (a) and (b)).

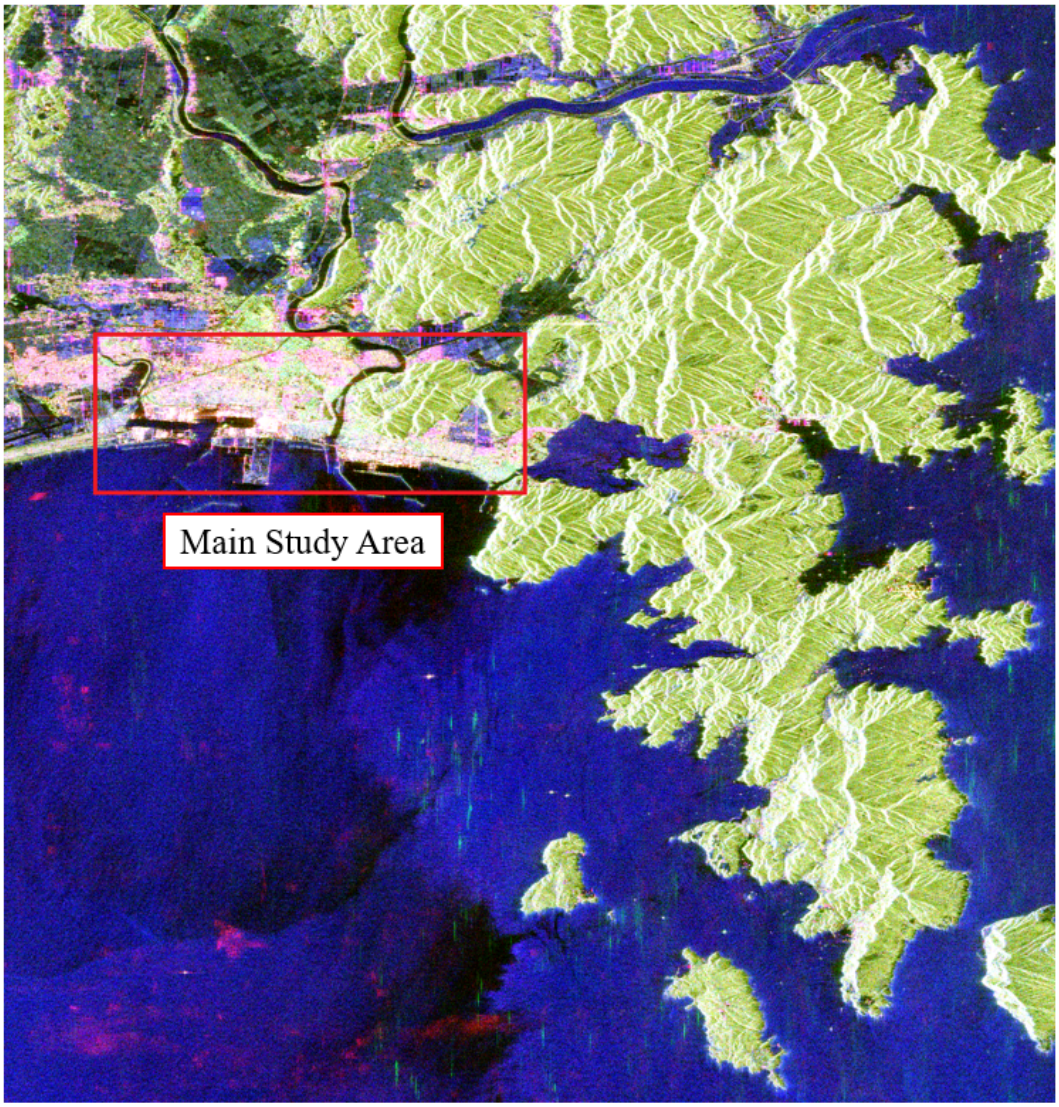

Figure 5.2: Preprocessed post-event PauliRGB image with main study area is marked.

5.3 Methodology

Figure 5.3 is a flowchart of the new damage assessment technique. Preprocessing for the raw post-event dataset includes multi-looking and filtering. An initial classification result is calculated firstly using SVM classification. The whole image is classified into four classes. The inputs are the Polarization Orientation Angle (POA) compensation conducted features. As introduced before, oriented and damaged buildings share similar features with foreshortening mountainous regions. The polarimetric features that ex-

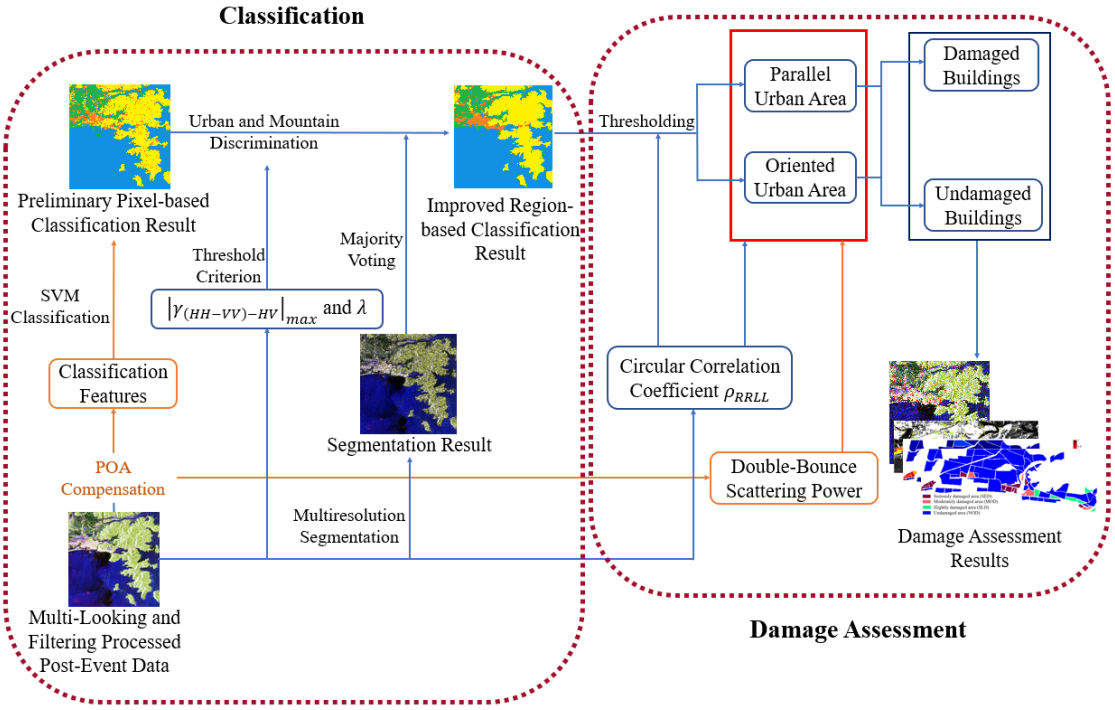

Figure 5.3: Flowchart for the proposed algorithm.

tracted by eigenvalue based decomposition and conventional model cannot effectively distinguish these categories. It leads to that the initial result shows some misclassification between mountain and urban areas. Majority voting and thresholding are introduced to solve this problem. The combination of these two techniques can obtain a better result. Multiresolution segmentation technique is introduced to calculate segmentation result for majority voting.

For Tohoku earthquake/tsunami, its disaster situation is complex. Damaged buildings under large orientation angle exist, it will influence damage assessment work. By conventional methods [50, 53], these buildings will be labeled as oriented and undamaged. This proposed method takes this situation into account. The whole urban areas are classified into oriented and parallel buildings firstly through setting threshold using ρ_{RRLL}. Then, from these two categories, damaged buildings can be detected.

5.4 An improved classification method using majority voting and thresholding

5.4.1 Preliminary classification

The SVM classifier is employed to calculate the initial result. This classification procedure is to detect out all buildings by removing other areas. The polarimetric features are calculated using the POA compensated dataset that obtained after the event, they serve as inputs for SVM classifier. The whole image contains four classes, including farmland, water, mountainous and urban area; the urban area covers all building types.

POA compensation

Oriented buildings are those divergent to the satellite flight path. The POA compensation [99] can solve the problem that these buildings are lacking of reflection symmetry [52].

Right-handed and left-handed circular polarization responses are,

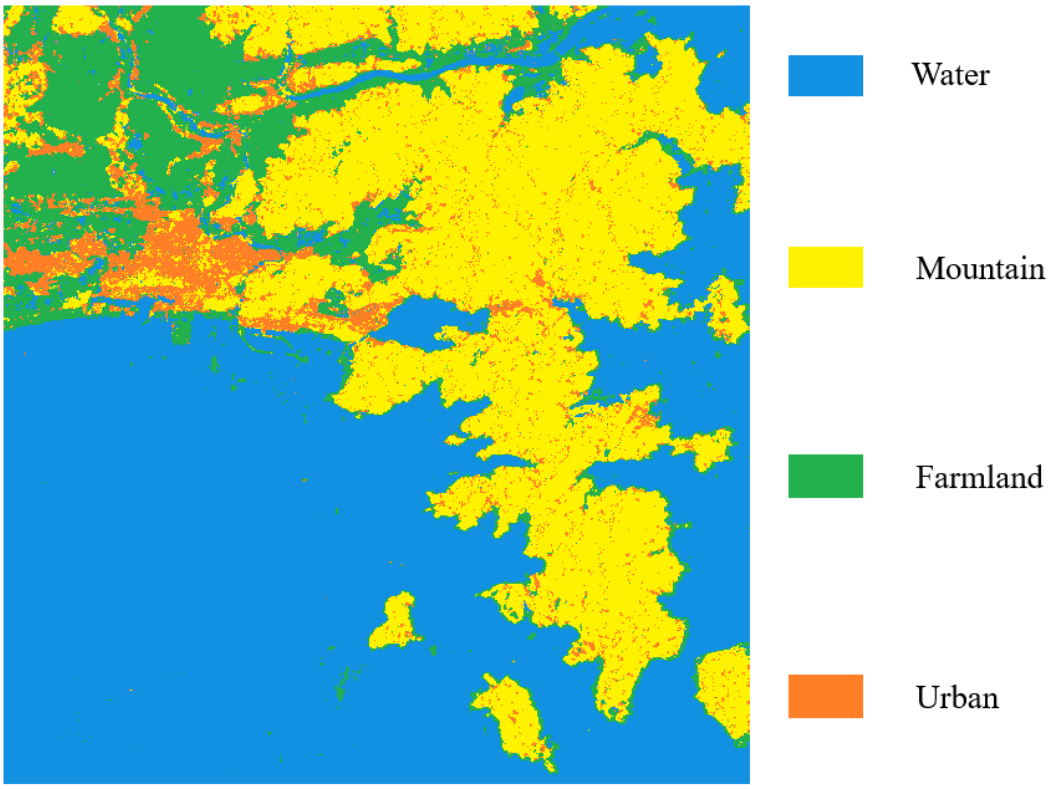

Figure 5.4: Preliminary classification result by SVM classifier.

$$S_{\text{RR}} = (S_{\text{HH}} - S_{\text{VV}} + i2S_{\text{HV}})/2,$$
$$S_{\text{LL}} = (S_{\text{VV}} - S_{\text{HH}} + i2S_{\text{HV}})/2. \tag{5.1}$$

Orientation angle θ is geometrically related to radar look angle and topographical slopes. It is,

$$\theta = [\text{Arg}(\langle S_{\text{RR}} S_{\text{LL}}^{*} \rangle) + \pi]/4. \tag{5.2}$$

$\langle \cdot \rangle$ means the ensemble average, which can be conducted by filtering.

Orientation angle θ compensation can be written as,

$$\mathbf{T}^{(new)} = \mathbf{UTU}^{T} \tag{5.3}$$

where **U** is defined as,

$$\mathbf{U} = \begin{bmatrix} 1 & 0 & 0 \\ 0 & \cos 2\theta & \sin 2\theta \\ 0 & -\sin 2\theta & \cos 2\theta \end{bmatrix} \tag{5.4}$$

Preliminary result

For the SVM method, seven polarimetric parameters are severed as the classification features. They are parameters H, A, and α from Cloude-Pottier decomposition, and four scattering powers from Yamaguchi decomposition. These features are obtained from data that POA compensation conducted.

Figure 5.4 is the acquired preliminary classification result. It shows that farmland and water areas can be classified accurately, and misclassification exists among urban and mountain areas. Significant amount of cross-pol backscattering exists in foreshortening mountain areas and oriented buildings, and they lack reflection symmetry [15]. Even though the POA compensation is applied to correct the data, these buildings still show different characteristics with parallel buildings. It leads to i) parts of oriented buildings and most damaged buildings will be labeled with mountain; ii) parts of fore-

shortening mountainous regions will be classified as urban. All these problems cause the misclassification in this preliminary result.

5.4.2 Majority voting and thresholding based classification

Mountain and urban areas classification

Polarimetric coherence magnitude is shown as follows, it is sensitive to targets' orientation.

$$|\gamma_{1-2}(\theta)| = \frac{|\langle s_1(\theta) s_2^*(\theta)\rangle|}{\sqrt{\langle |s_1(\theta)|^2\rangle \langle |s_2(\theta)|^2\rangle}}. \tag{5.5}$$

s_1 and s_2 are two polarization channels. Rotation angle $\theta_{\gamma-max}$ can be derived as,

$$\theta_{\gamma-\max} = \theta \ \text{ when } \ |\gamma_{1-2}(\theta)|' = 0 \ \text{ and } \ |\gamma_{1-2}(\theta)|'' < 0 \tag{5.6}$$

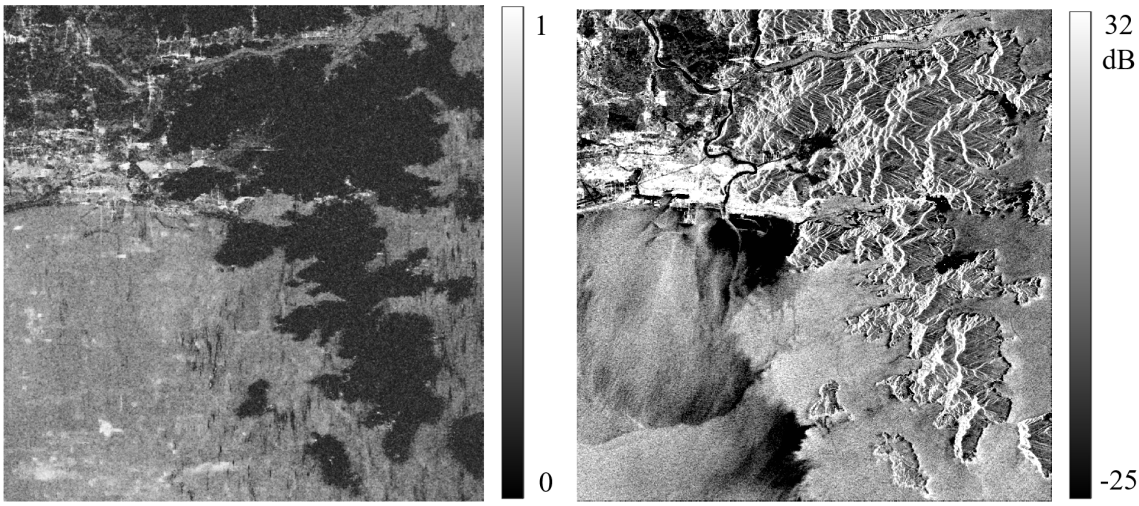

(a) (b)

Figure 5.5: Value distributions of polarimetric features (a) $|\gamma_{(\mathsf{HH-VV})-(\mathsf{HV})}|_{\mathsf{max}}$; (b) λ.

Figure 5.5 (b) indicates the distribution of parameter λ. It shows that values of λ for foreshortening mountainous areas and building areas are larger than those of rest mountainous regions. Thus, the λ based threshold can be set to distinguish these two categories. This thresholding processing is conducted on the pixels that labeled mountainous areas or building areas. After all these areas are detected out, an threshold can

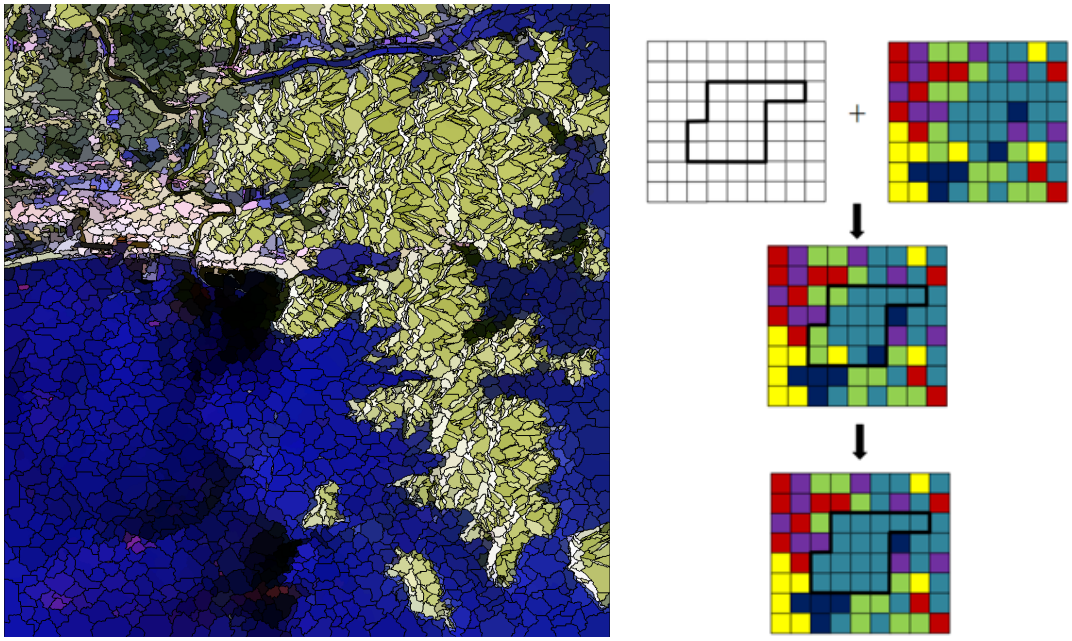

(a) (b)

Figure 5.6: (a) Segmentation result using multiresolution method; (b) Schematic diagram about majority voting algorithm.

be set based on $|\gamma_{(\mathrm{HH-VV})-(\mathrm{HV})}|_{\max}$ to detect foreshortening mountain areas. The distribution of $|\gamma_{(\mathrm{HH-VV})-(\mathrm{HV})}|_{\max}$ is shown as Figure 5.5 (a). Therefore, all the urban areas can be labeled out. Based on the above analysis, the judging criterion is,

$$\begin{aligned} x \in \text{urban}, \ \text{if } x \in \text{mountain} \ \text{ and } \ \lambda(x) > \varepsilon_1; \\ x \in \text{mountain}, \ \text{if } x \in \text{urban} \ \text{ and } \ |\gamma_{(\mathrm{HH-VV})-(\mathrm{HV})}|_{\max}(x) < \varepsilon_2; \end{aligned} \tag{5.7}$$

x means the tested pixel, and thresholds for ε_1 and ε_2 can be calculated based on histograms.

Majority voting

As discussed above, the introduction of the thresholding algorithm can discriminate urban and mountain areas, however, there still exist misclassified pixels. Moreover, noise that exists in PolSAR dataset would affect the result. Majority voting [28, 100] is a useful algorithm to enforce the pixels in the local area share the same class labels. The principle for this method is to set class labels to the whole superpixel, and this

label is calculated by picking out the highest frequency one. Figure 5.6 (b) presents the schematic diagram for the majority voting method.

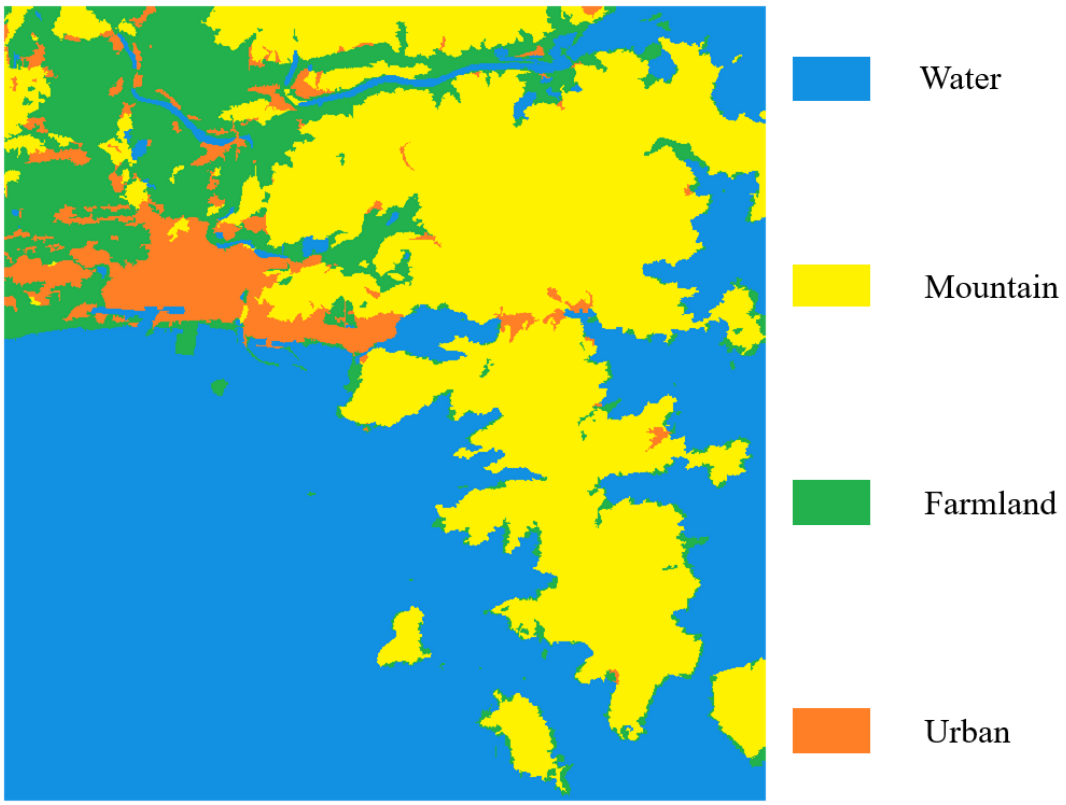

Figure 5.7: Region-based classification result.

Multiresolution segmentation method [89] is introduced to calculate the superpixels. Figure 5.6 (a) shows the segmentation result. The boundary of every superpixel is marked with black color, and the pixels are colored by the averaged color of all pixels in it. This PauliRGB image is over-segmented, and the result contains 4397 regions.

The final classification result is shown as Figure 5.7. Thresholds ε_1 and ε_2 in Equation 5.7 are set as 0.29 and 0.23, respectively. This classification result shows that most misclassified oriented buildings and damaged buildings are now classified correctly. Urban areas can be extracted according to Figure 5.7, and they are for subsequent assessment.

Figure 5.8 (a) is the ground-truth urban area map for Ishinomaki city. Buildings detected from the preliminary result (Figure 5.4) is presented as Figure 5.8 (b), and sub-

figure (c) is the result extracted from the improved result (Figure 5.7). The performance of this improved method is much better. Figure 5.8 (c) detects out oriented buildings and damaged buildings. With the introduction of majority voting and thresholding techniques, the accuracy of urban area extraction is increased.

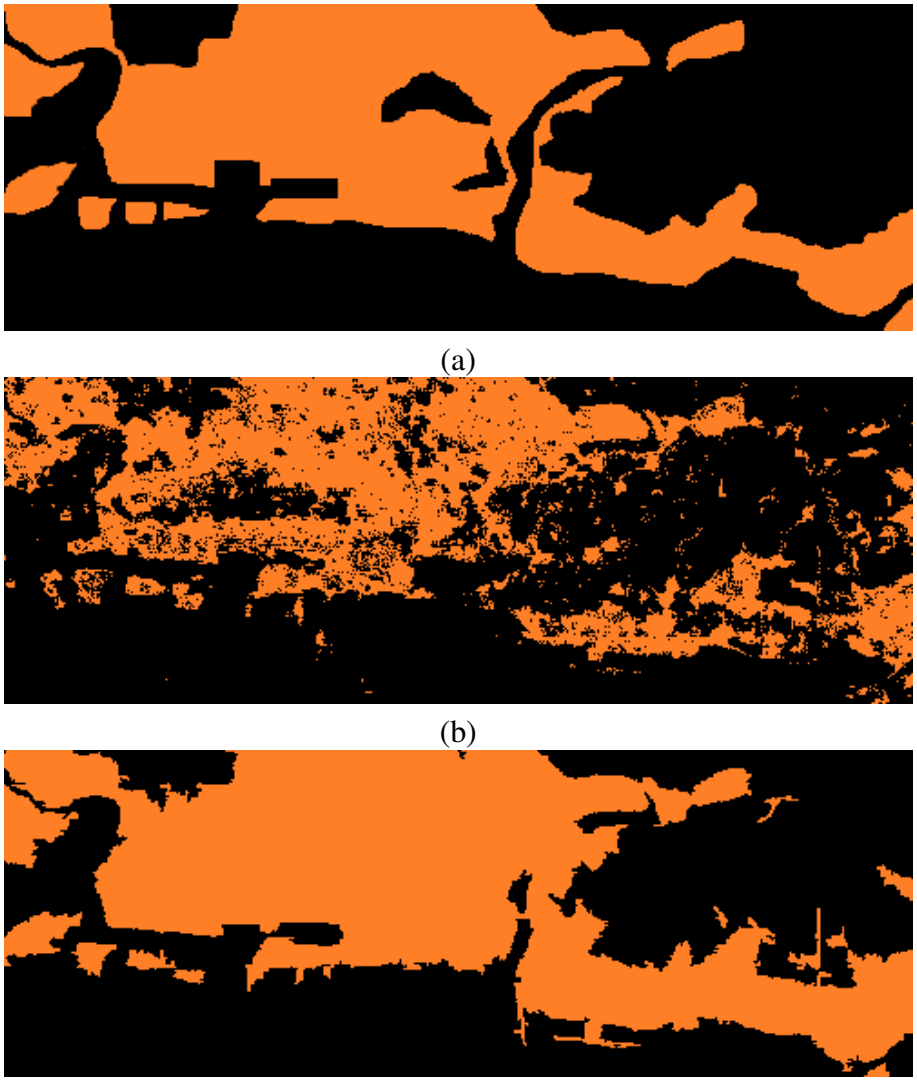

Figure 5.8: (a) Reference map for urban area; (b) Buildings extracted from preliminary result; (c) Buildings extracted from improved classification result.

5.5 Damage information extraction

By analyzing P_d or other polarimetric features, buildings and other man-made structures can be identified. Many previous works [43–45,48,51,52] verified both $\rho_{RRLLRRLL}$ and P_d are valid parameters for building condition analysis. Without pre-event dataset, the changes in these indexes caused by the disaster cannot be calculated. However, damage condition can be distinguished by the difference of these values.

5.5.1 Analysis about the coastal area of Ishinomaki city

Aftereffect debris of buildings has random orientation and spatial arrangement, which is similar to oriented buildings. Oriented buildings are defined as undamaged in the works [50, 53]. However, a large orientation angle can also be found in damaged buildings. By the above methods, these collapsed buildings will be regarded as oriented, which are undamaged. A series of detailed analysis is conducted to detect the polarimetric characteristics of urban areas, which is to discuss this situation.

Figure 5.9 (a) shows the distribution map of ρ_{RRLL} around main study area. The background image (gray scale image) for it is SPAN image. The distribution map shows that the whole urban area can be clearly classified into two categories, including the undamaged parallel buildings with large values, and the damaged and oriented buildings with small values.

By analyzing the P_d value changes caused by POA compensation, oriented buildings can be identified, which are the pixels that great change occurs. Figure 5.9 (b) is distribution of ρ_{RRLL} for parallel buildings. When all the oriented buildings have been removed, the difference in ρ_{RRLL} values can be employed to pick out damaged buildings. But compared with the reference map, Figure 5.9 (b) does not include all the damaged buildings. There should exist damaged areas marked with a red rectangle which are not shown in the image. It is because these damaged buildings are also oriented, and they are shown in Figure 5.9 (c). By defining the oriented buildings as undamaged, these damaged areas cannot be detected out.

Figure 5.10 presents the distribution of orientation angles. It indicates that the an-

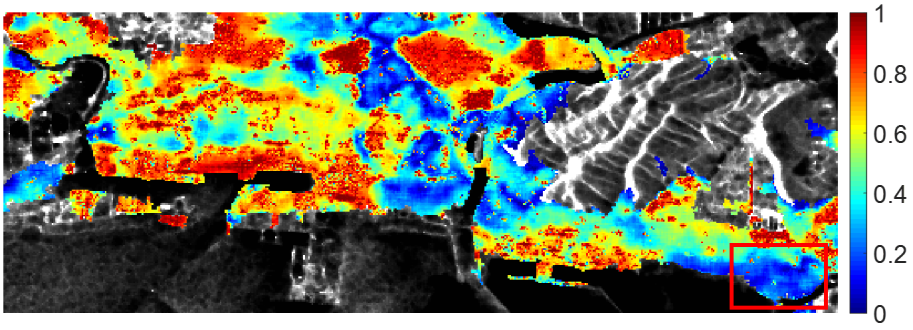

(a)

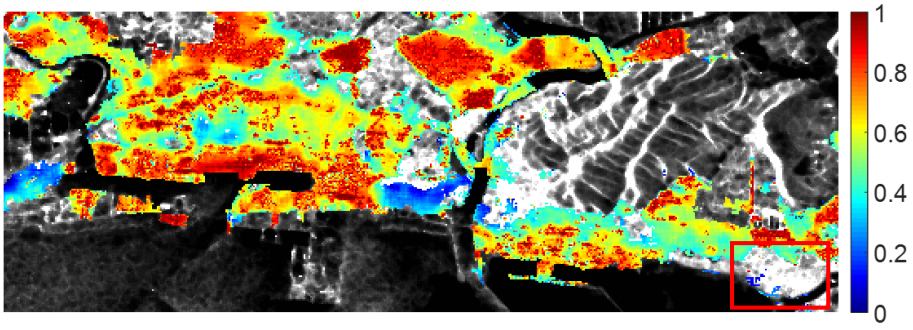

(b)

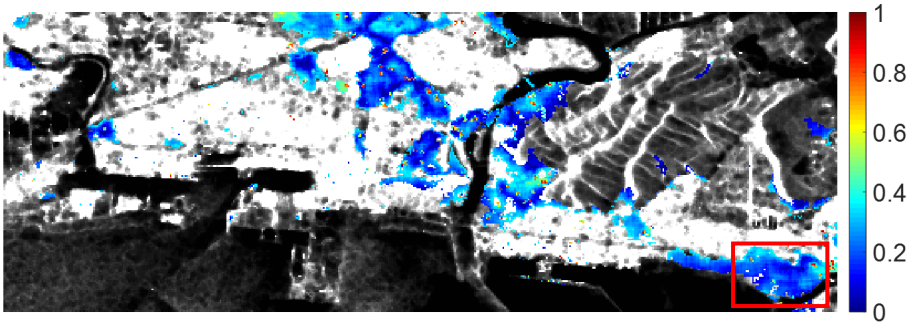

(c)

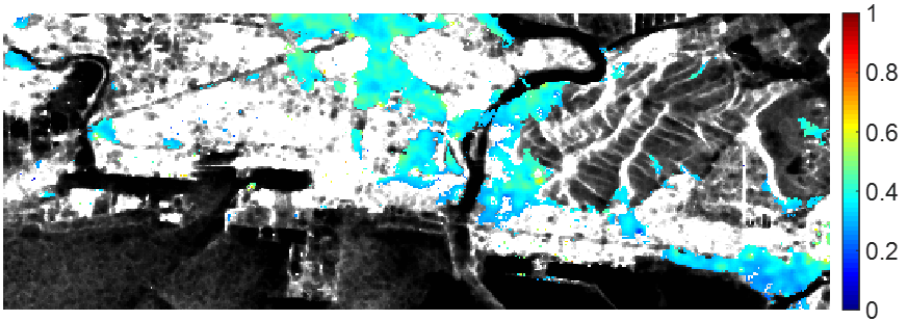

(d)

Figure 5.9: Distribution maps of two parameters in different urban area. (a) Distribution of ρ_{RRLL} for whole urban area; (b) Distribution of ρ_{RRLL} for parallel area; (c) Distribution of ρ_{RRLL} for oriented area; (d) Distribution of P_d for oriented area.

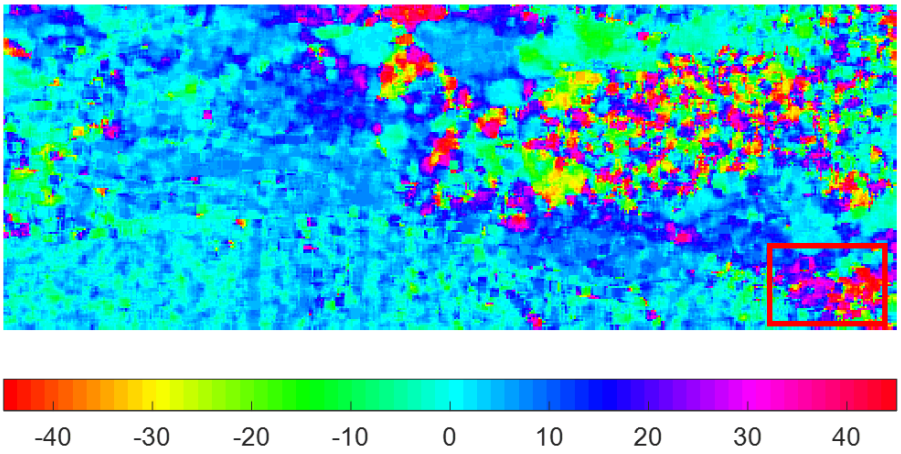

Figure 5.10: Orientation angle distribution in the study urban area.

gle values for the red rectangle marked buildings are much bigger than those for other damaged buildings. According to Equation 5.2, 5.3, and 5.4, large orientation angle will lead to the big change in coherency matrix T. Therefore, P_d value change would be big. These damaged buildings under large orientation angle should be considered. According to the discussions above, the condition of all the buildings shall be categorized into four classes. Which are i) undamaged parallel building, ii) damaged parallel building, iii) undamaged oriented building, and, iv) damaged oriented building.

To explore the difference in the polarimetric characteristics of these four kinds of buildings, samples are selected from every building category. These pixels are selected from seven zones that marked with different colored rectangle boxes. Figure 5.11 (a) shows their location. The chosen of undamaged and damaged buildings is based on ground-truth information, and the distinguishing of oriented and parallel buildings is according to P_s value change caused by POA compensation [53].

Figure 5.11 (b) shows the values of real and imaginary part of ρ_{RRLL}. It indicates that the parallel buildings are located in second and third quadrants, and oriented buildings are located in the fourth quadrant. Moreover, this map shows that the circular correlation coefficient's real part value can distinguish oriented and parallel buildings. Figure 5.11 (c) presents the circular correlation coefficient's modulus and phase value, and it indicates undamaged and damaged buildings have different values. There exists great value

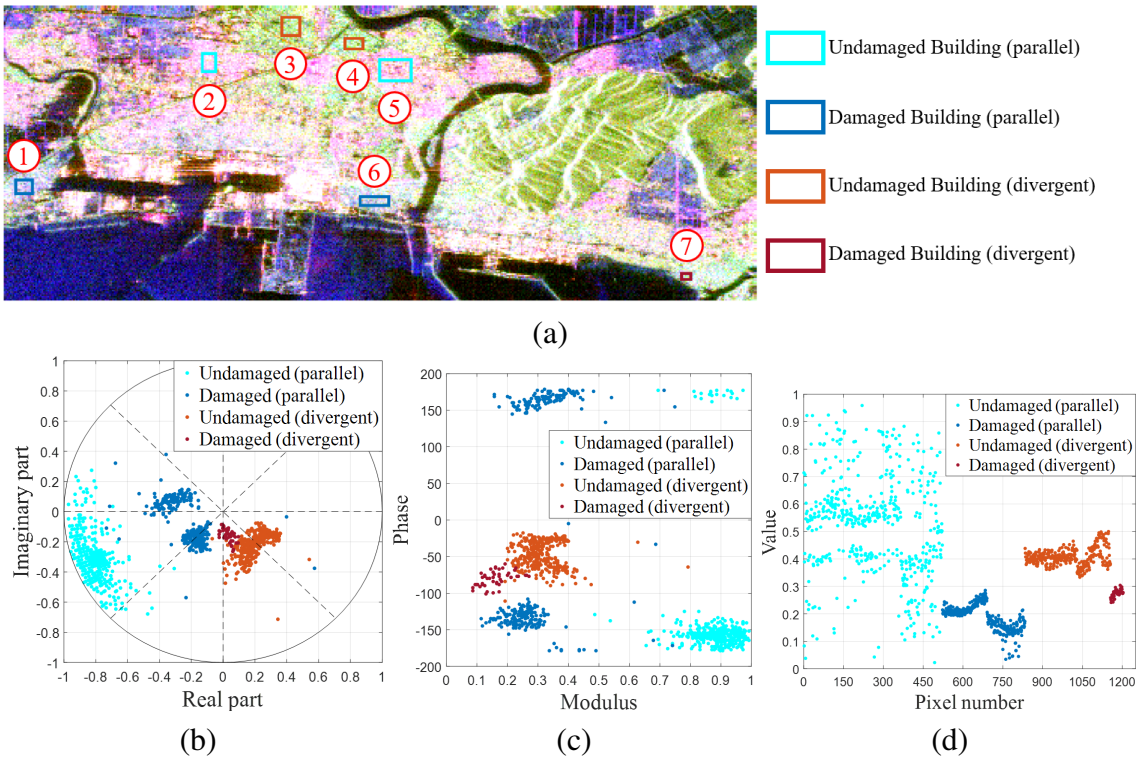

Figure 5.11: Polarimetric characteristic analysis. (a) Location of tested pixels; (b) Distribution of real and imaginary part of ρ_{RRLL}; (c) Distribution of modulus and phase value of ρ_{RRLL}; (d) Value distribution of P_s.

difference between undamaged and damaged parallel building, both damaged parallel building have similar values with undamaged and damaged oriented building.

For damaged building identification in the orientation area, P_d is found as a more effective index. Figure 5.11 (d) shows the value distribution of P_d for tested samples. It indicates that this index is not appropriate in differentiating undamaged and damaged parallel buildings. But there exists a great difference between undamaged and damaged orientation buildings. Figure 5.9 (d) is the distribution map for P_d for the oriented area, from which difference can be detected between undamaged and damaged buildings. Therefore, a threshold based on P_d can be set to detect damaged orientation buildings.

5.5.2 An unsupervised damaged building extraction algorithm

The damaged buildings identification work can be done by separately detecting them from oriented and parallel areas. For parallel areas, the magnitude of the circular corre-

lation coefficient is a suitable parameter to detect out all the damaged buildings. While oriented areas, P_s can be introduced.

According to the discussions, an unsupervised algorithm can be introduced. When all urban areas have been extracted, they will be classified into two categories firstly, including oriented and parallel areas. For these two areas, damaged buildings can be detected separately by two thresholds. A criterion is designed as,

$$\begin{aligned} x \in \text{damaged building, if } x \in \text{parallel area and } \rho_{\text{RRLL}}(x) < T_1; \\ x \in \text{damaged building, if } x \in \text{oriented area and } P_{\text{d}}(x) < T_2; \end{aligned} \tag{5.8}$$

where x is the urban labeled test pixel. Thresholds T_1 and T_2 are determined by statistical histogram analysis.

5.6 Results and discussions

Figure 5.12 presents the damaged building assessment result of the whole PolSAR dataset. Thresholds T_1 and T_2 in Equation 5.8 are 0.47 and 0.305, respectively. Extracted damaged buildings are labeled with red color.

5.6.1 Coastal area of Ishinomaki city

The obtained result is transformed into a block scale result to better evaluate the damage information. The ratio of damaged building labeled pixels' number to the entire pixel number for every block means the damage level. Figure 5.13 (a) shows the damage level result, and subfigure (b) is the damage degree map. The damage degree map shows that the result is accurate. Figure 5.13 (c) is the distribution map of misclassified blocks, which are labeled as red color.

ρ_{RRLL} is sensitive to man-made structures. It can be used as a valid index to represent damage level. This index can be written as Equation (5.9). Figure 5.13 (d) indicates the damage level mapping result created by index $I_{\rho_{\text{RRLL}}}$. This map describes both the damaged buildings' location and the corresponding damage severity.

$$I_{\rho_{\text{RRLL}}} = 1 - \langle \rho_{\text{RRLL}} \rangle \tag{5.9}$$

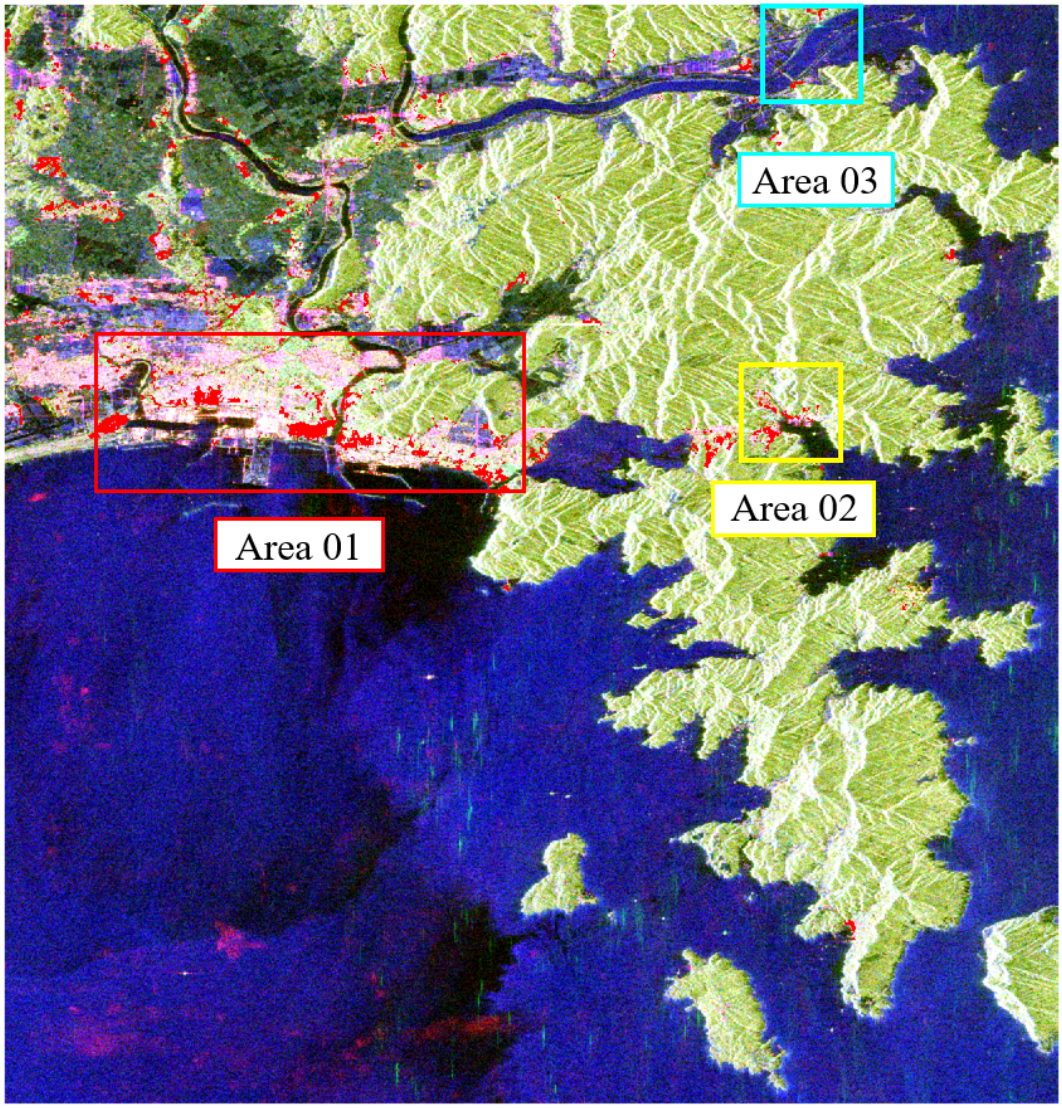

Figure 5.12: Damaged building extraction result.

5.6.2 Analysis for another two areas

The proposed method is also implemented in another two areas to test its validity. Figure 5.12 Area 02 and Area 03 show the location of these two regions.

Figure 5.14 (b) shows the extracted damaged buildings for Onagawa Town, Miyagi Prefecture (Area 02). The ground-truth map shows that most buildings near the ocean were damaged. The proposed method can interpret this situation.

Figure 5.14 (d) shows the extraction result of damaged buildings for Ishinomaki City's river area. Damaged buildings that close to the bridge can be detected success-

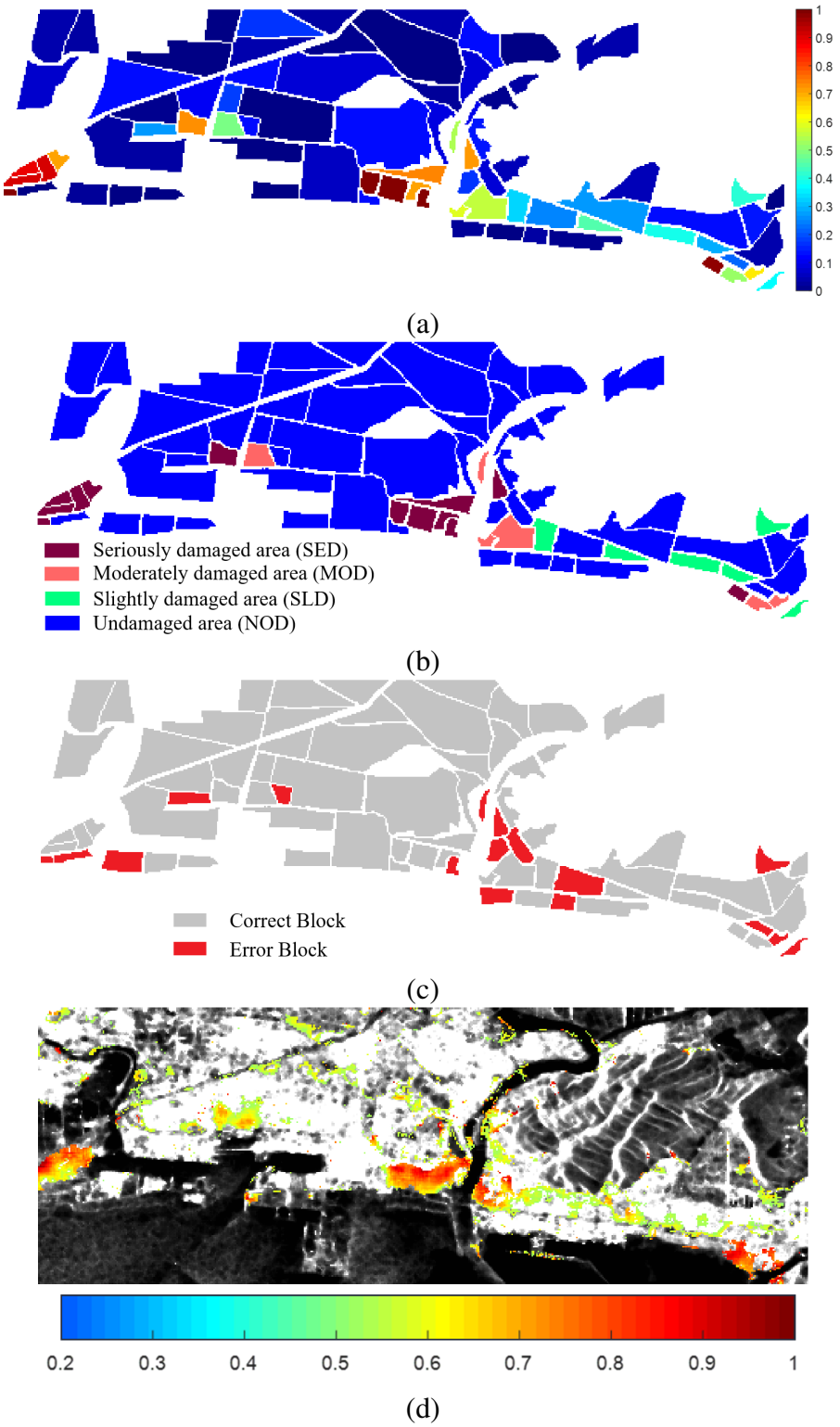

Figure 5.13: (a) Damage level result ; (b) Damage degree result; (c) Error blocks map; (d) Damage assessment result by $I_{\rho_{\mathrm{RRLL}}}$.

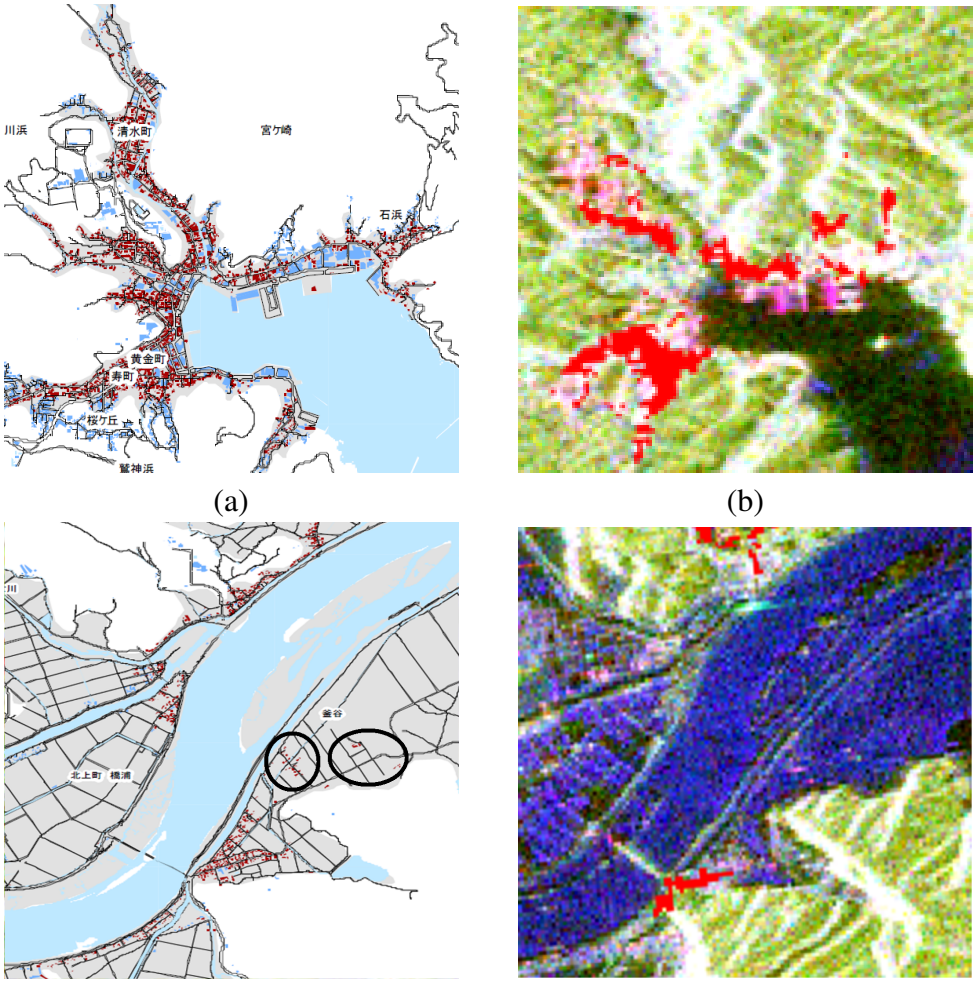

(a) (b)

(c) (d)

Figure 5.14: (a) Reference map for Onagawa Town; (b) Extracted damaged buildings for Onagawa Town; (c) Reference map for the river area in Ishinomaki city; (d) Extracted damaged buildings for the river area in Ishinomaki city.

fully. However, there exist mistakes, especially buildings close to the estuary (marked with a black circle in Figure 5.14 (c)) are not identified. For these areas, all the man-made structures have been destroyed by the tsunami. Moreover, the standing water caused that these pixels are labeled as water. Without pre-disaster data, damaged buildings in this area cannot be figured by this technique.

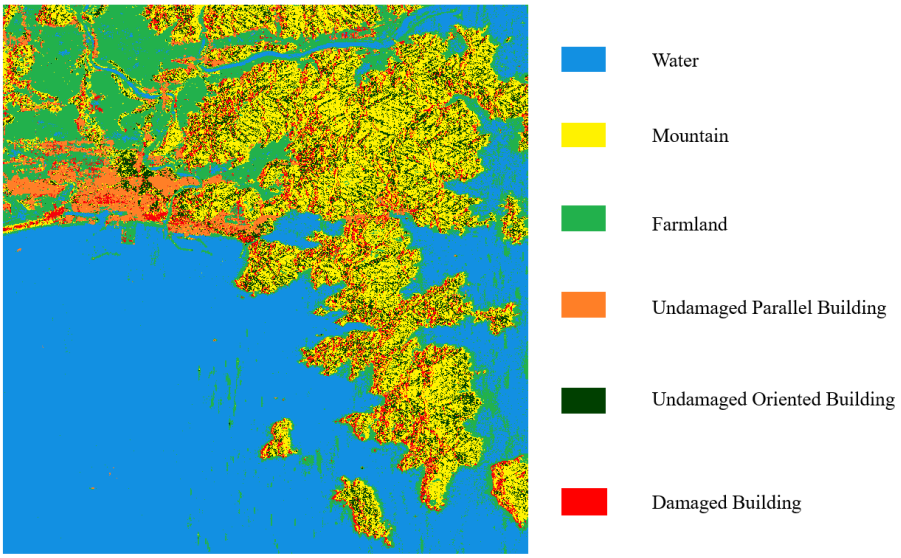

(a)

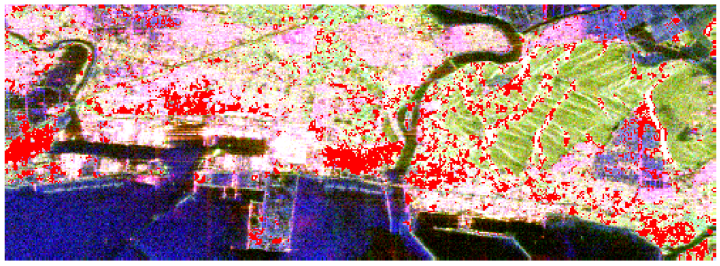

(b)

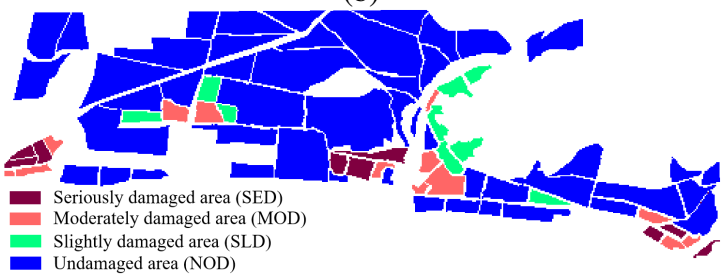

(c)

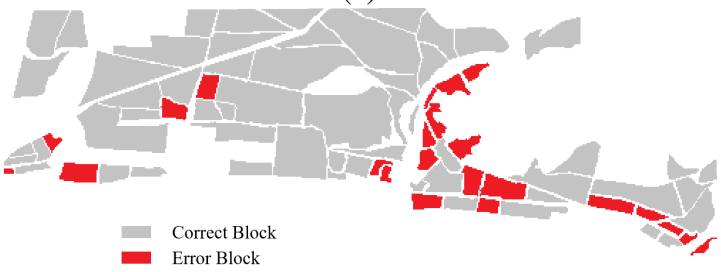

(d)

Figure 5.15: Damage assessment by SVM method. (a) Classification result; (b) Extracted damaged buildings; (c) Damage degree map; (d) Error block map.

5.6.3 Comparison with supervised method

The proposed algorithm can interpret the damage without training processing, it means ground-truth damage information is not needed. To benchmark this method against the existing approaches, a comparison experiment is conducted between the result of this work and that using SVM classification method. Cloude-Pottier decomposition features, Yamaguchi decomposition features, ρ_{RRLL}, and $|\gamma_{(\mathrm{HH-VV})-(\mathrm{HV})}|_{\max}$ serve as classification features. Training samples for SVM classification are chosen from the ground-truth map. Figure 5.15 (a) is the damage assessment result. The whole image was classified into 6 classes, including farmland, water, mountainous area, damaged building, undamaged oriented building, and undamaged parallel building. This supervised method can obtain a good result. However, misclassification exists because of the existing noise. What's more, many foreshortening mountainous pixels were classified as buildings.

Figure 5.15 (b) is the damaged building distribution map for the main study area. Figure 5.15 (c) is damage degree map. These two images show that this method can give a relatively good result, most MOD and SED regions can be marked accurately. However, there still exists the situation that many SLD and NOD areas are wrongly marked. Figure 5.15 (d) is the error distribution map, it shows that this supervised

Table 5.1: Comparison of proposed method to the SVM classifier.

		SVM				Proposed method			
		SED	MOD	SLD	NOD	SED	MOD	SLD	NOD
		(Number of blocks matched to true damage degree)							
GT	SED	7	3	0	0	10	0	0	0
	MOD	0	5	0	0	0	4	0	1
	SLD	1	3	4	8	2	1	4	9
	NOD	1	2	5	41	1	1	2	45
	C/T	7/10	5/5	4/16	41/49	10/10	4/5	4/16	45/49
	Accuracy(%)	73.72	100	23.05	96.6	100	87.67	27.57	98.74
		Overall Accuracy: 88.81%				Overall Accuracy: 92.28%			

C represents the number of correct blocks. T represents the total number of blocks according to ground truth.

method is worse than the proposed method.

Table 5.1 shows the accuracy of these two damage assessment methods. C/T means the percentage of correct blocks to all zones. All accuracies are based on the pixel scale. The method in this chapter can detect all SED areas, most NOD and MOD areas. Accuracy for the SVM method is 88.81% and that for the introduced algorithm is 92.28%. The comparison indicates the unsupervised method proposed in this chapter is better than the supervised method.

5.7 Conclusion

A novel damage assessment method has been introduced in this chapter. This method can extract damage information for building areas under complex damage situation. It shows great superiority, and only post-event data is needed. The method is implemented in the Tohoku earthquake event by analyzing L-band ALOS/PALSAR dataset.

The proposed technique can identify most damaged buildings. To overcome the existing problem, effective techniques such as majority voting and thresholding are introduced, by which all the urban areas can be extracted. Moreover, different kinds of buildings are analyzed, and many valid parameters are found out, such as double-bounce scattering power and circular correlation coefficient, they can better extract damaged buildings by considering about the oriented buildings that under big orientation angle. Four types of buildings are proposed, the comparison with the SVM classification method shows that this kind of method can better assess damage information.

6

Summery and Outlook

6.1 Summery

With the development of radar technology, polarimetric SAR image processing and it's application for disaster monitoring, which is one of the research focus in radar image processing, has made significant progress. This thesis introduced a novel image classification method and two kinds of earthquake damage assessment algorithms. The features which can be extracted from PolSAR data was introduced firstly. For PolSAR image processing, a new unsupervised classification technique is presented, and it employs sparse representation theory. As for the application of PolSAR image, two kinds of earthquake damage assessment algorithms were introduced. One of them is based on a novel damage level index to calculate earthquake damage level mapping result by post- and pre-event dataset, the second one is just based on the single post-event image, this method can extract all the damaged buildings without the need of prior damage information for training processing.

Chapter 2 mainly introduced the PolSAR data description forms and many target decomposition methods. Polarimetric features which can provide useful information about target terrains can be extracted by the introduced target decomposition methods. This thesis introduced these theories by classifying them into two classes, including coherent target decomposition methods (Pauli decomposition and Krogager decomposition) and incoherent target decomposition methods (Cloude-Pottier decomposition, Freeman decomposition, Yamaguchi four-component decomposition, and Neumann two-component decomposition). The extracted polarimetric features were used as the classification features in Chapter 3, image classification, and to provide useful

information for earthquake damage assessment (Chapter 4 and Chapter 5). Except for the features extracted from target decomposition methods, another polarimetric feature, the correlation coefficient was also introduced in this chapter. This feature shows great potential in damage assessment work. It can be used to compose the damage level index, which can better evaluate the building damage in Chapter 3. This feature was also introduced in Chapter 5 to distinguish undamaged buildings and damaged buildings by considering orientation angle's influence.

Chapter 3 introduced an unsupervised PolSAR image classification algorithm. 49 classification features, including polarimetric features and color features, were extracted to provide varied information. An energy function based on label smoothness constraint and sparse representation theory was defined. A corresponding optimization method was designed to update the dictionary and final result, class labels. This unsupervised method was implemented on three PolSAR datasets. A series of experiments were conducted, which verified that the dictionary and class labels were optimized effectively during every loop by the optimization method. The analysis of parameters values was also conducted. It indicated the influence of different parameter values to the final result, and also verified the effectiveness of the proposed unsupervised classification technique. The comparison with other unsupervised/supervised method indicated the superiority of the proposed method. It can acquire high accuracy classification result without the need of training samples.

Chapter 4 and Chapter 5 are about the application of PolSAR data in disaster monitoring, and two kinds of earthquake damage assessment methods were introduced. The main study event for these two methods is the Tohoku earthquake/tsunami. The algorithm in Chapter 4 is conducted on the analyses of both pre- and post-event datasets. Change value of double-bounce scattering power before and after disaster provides useful information. The proposed method combined this feature and the other three valid polarimetric features to compose the improved damage level index. The improved index was under the Mahalanobis metric. By the proposed index, accurate damage level and damage degree mapping results can be calculated. A series of experiments were con-

ducted which verified the superiority of this proposed damage level index. The analyses about another disaster event, Kumamoto earthquake further indicated its robustness.

The earthquake damage assessment algorithm introduced in Chapter 5 was based on the post-disaster image. Contribution of this method is the improvement in both the urban area extraction and the damaged building detection. The thresholding and majority voting methods were combined to extract all the building areas, it can better distinguish urban and mountainous areas. For damaged areas detection, all the urban areas were classified into four categories by considering the influence of orientation angle. This method can better extract all damaged buildings, especially the oriented damaged buildings. The method is unsupervised, which means no prior damage information is needed, and it shows better performance even than the supervised method.

A PolSAR image can provide multitudinous information for image processing works and applications. Features extracted from the PolSAR dataset can effectively describe the characteristic of target terrains, which is important for many image processing works. The two earthquake damage assessment methods introduced in Chapter 4 and 5 also manifest the great potential of PolSAR dataset for damage condition exploration.

6.2 Outlook

With the development of technology, acquisition ability for radar data is greatly improved. However, the corresponding image processing technique still needs to be further improved.

For the image classification work, the unsupervised method using sparse representation theory that introduced in this thesis can obtain results with high accuracy without the need of training samples. However, For the reason that both the sparse representation method and the iteration processing occupies time, the computational speed of this method is slower than classical classification methods. For the Flevoland dataset, it takes 1481s; for the Foulum dataset, it takes 2941s; for the San Francisco dataset, it takes 2830s (Matlab R2016b; Iteration time=6; 4 cores CPU with a core frequency of 3.2GHz). Even though its classification accuracy is much higher than many other su-

pervised classification methods, seeking the ways that can speed up the computational speed is still the next key work. Deep learning technique which has been widely used to solve remote sensing problems is also a good option to handle the image classification work. For future research, the study about its applications will also be the main work.

For the disaster monitoring work, even though the two kinds of technique introduced in this thesis can obtain satisfactory damage assessment results, the algorithms which can be widely used for different kinds of disaster events should also be studied. More complex disaster situations should be considered, and accurate unsupervised methods should be the main research content for its advantage that this kind of method can obtain fast result without the need of ground-truth information. Moreover, other satellite datasets such as images by Sentinel and RADARSAT can also be applied to this research. They will provide valid information for disaster damage assessment.

7

List of Publications

First Author in Peer Review International Journal:

1. Yaqi Ji, Josaphat Tetuko Sri Sumantyo, Ming Yam Chua, and Mirza Muhammad Waqar, "Earthquake/Tsunami Damage Level Mapping of Urban Areas Using Full Polarimetric SAR Data", *IEEE Journal of Selected Topics in Applied Earth Observations and Remote Sensing*, Vol. 11, Issue: 7, 2296 - 2309, 19/04/2018. https://ieeexplore.ieee.org/abstract/document/8341956

2. Yaqi Ji, Josaphat Tetuko Sri Sumantyo, Ming Yam Chua, and Mirza Muhammad Waqar, "Earthquake/tsunami damage assessment for urban areas using post-event PolSAR data", *Remote Sensing*, Vol. 10, Issue: 7, 1088, 08/07/2018. https://www.mdpi.com/2072-4292/10/7/1088

3. Yaqi Ji, Josaphat Tetuko Sri Sumantyo, Ming Yam Chua, and Mirza Muhammad Waqar, "Unsupervised PolSAR Image Classification based on Sparse Representation", *International Journal of Remote Sensing*, Vol. 40, Issue: 16, 6224 - 6248, 21/03/2019. https://www.tandfonline.com/doi/abs/10.1080/01431161.2019.1587209

Co-Author in Peer Review International Journal:

1. Jian Cheng, Yaqi Ji, Haijun Liu, "Segmentation-based PolSAR image classification using visual features: RHLBP and color features", *Remote Sensing*, Vol. 7, Issue: 5, 6079-6106, 15/05/2015. https://www.mdpi.com/2072-4292/7/5/6079/htm

2. Ming Yam Chua, Josaphat T. Sri Sumantyo, Cahya E. Santosa, Good F. Panggabean, Karna Sasmita, Franciskus D. Sri Sumantyo, Tomoro Watanabe, Ya Qi Ji, Peberlin P. Sitompul, Mohammad Nasucha, Farohaji, Kurniawan, Babag Purbantoro, Asif Awaludin, Eko T. Rahardjo, Gunawan Wibisono, Retnadi H. Jatmiko, Sudaryatno Sudaryatno, Taufik H. Purwanto, Barandi S. Widartono, Muhammad Kamal, "The Maiden Flight of Hinotori-C: The First C Band Full Polarimetric Circularly Polarized Synthetic Aperture Radar in the World", *IEEE Aerospace and Electronic Systems Magazine*, Vol. 34, Issue: 2, 24-35, 12/06/2019. https://ieeexplore.ieee.org/abstract/document/8736180

Oral Presentation in Conference :

First Author

1. Yaqi Ji, Josaphat Tetuko Sri Sumantyo, Ming Yam Chua, and Mirza Muhammad Waqar, "Single Post-event PolSAR Data based Earthquake/Tsunami Damage Information Extraction in Urban Areas", Innovative Microwave Remote Sensing, 2P1, Progress in Electromagnetics Research Symposiums (PIERS 2018), 1-4 August 2018, Toyama.

2. Yaqi Ji, Josaphat Tetuko Sri Sumantyo, Ming Yam Chua, and Mirza Muhammad Waqar, "Earthquake/Tsunami Damage Level Mapping of Urban Areas using Full Polarimetric SAR Sata", The 63rd Autumn Conference of the Remote Sensing Society of Japan, 21-22 November 2017, Hokkaido.

Co-Author

1. Ming Yam Chua, Josaphat Tetuko Sri Sumantyo, and Yaqi Ji, "An 8-channels FPGA-based Reconfigurable Chirp Generator for Multi-band Full Polarimetric Airborne/Spaceborne CP-SAR," Innovative Microwave Remote Sensing, 2P1, Progress in Electromagnetics Research Symposiums (PIERS 2018), 1-4 August

2018, Toyama.

2. Ming Yam Chua, Josaphat Tetuko Sri Sumantyo, Cahya Edi Santosa, Good Fried Panggabean, Yaqi Ji, Peberlin Parulian Sitompul, and Mohammad Nasucha, "An PC-based Airborne SAR Baseband System," Innovative Microwave Remote Sensing, 2P1, Progress in Electromagnetics Research Symposiums (PIERS 2018), 1-4 August 2018, Toyama.

3. Josaphat Tetuko Sri Sumantyo, Ming Yam Chua, Cahya Edi Santosa, Good Fried Panggabean, Kengo Tsushima, Tomoro Watanabe, Karna Sasmita, Agus Mardiyanto, Franciscus Dwikoco Sri Sumantyo, Eko Tjipto Rahardjo, Gunawan Wibisono, Edi Supartono, Steven Gao, Peberlin Parulian Sitompul, Mohammad Nasucha, Farohaji Kurniawan, Asif Awaludin, Babag Purbantoro, Yaqi Ji, and Nobuyoshi Imura, "Hinotori-C: A Full Polarimetric C Band Airborne Circularly Polarized Synthetic Aperture Radar for Disaster Monitoring," SC5: SAR Imaging and Applications, Progress in Electromagnetics Research Symposiums (PIERS 2018), 1-4 August 2018, Toyama.

Poster Presentation in Conference :

First Author

1. Yaqi Ji, Josaphat Tetuko Sri Sumantyo, Ming Yam Chua, and Mirza Muhammad Waqar, "Earthquake Damage Investigation of Urban Areas using Polarimetric SAR Data", 2017 Future Earth Kick-off Workshop, 2 March 2017, Chiba.

8

References

[1] George Sinclair. The transmission and reception of elliptically polarized waves. *Proceedings of the IRE*, 38(2):148–151, 1950.

[2] Jakob J Zyl, Howard A Zebker, and Charles Elachi. Imaging radar polarization signatures: Theory and observation. *Radio Science*, 22(4):529–543, 1987.

[3] Diane L Evans, Tom G Farr, Jakob J Van Zyl, and Howard A Zebker. Radar polarimetry: analysis tools and applications. *IEEE Transactions on Geoscience and Remote Sensing*, 26(6):774–789, 1988.

[4] Jong-Sen Lee and Eric Pottier. *Polarimetric radar imaging: from basics to applications*. CRC press, 2009.

[5] S Quegan and I Rhodes. Statistical models for polarimetric data: consequences, testing and validity. *International Journal of Remote Sensing*, 16(7):1183–1210, 1995.

[6] Knut Conradsen, Allan Aasbjerg Nielsen, Jesper Schou, and Henning Skriver. A test statistic in the complex wishart distribution and its application to change detection in polarimetric sar data. *IEEE Transactions on Geoscience and Remote Sensing*, 41(1):4–19, 2003.

[7] Pierre Formont, Frédéric Pascal, Gabriel Vasile, Jean-Philippe Ovarlez, and Laurent Ferro-Famil. Statistical classification for heterogeneous polarimetric sar images. *IEEE Journal of Selected Topics in Signal Processing*, 5(3):567–576, 2011.

[8] Corina C Freitas, Alejandro C Frery, and Antonio H Correia. The polarimetric g distribution for sar data analysis. *Environmetrics: The official journal of the International Environmetrics Society*, 16(1):13–31, 2005.

[9] Anthony P Doulgeris, Stian Normann Anfinsen, and Torbjørn Eltoft. Automated non-gaussian clustering of polarimetric synthetic aperture radar images. *IEEE Transactions on Geoscience and Remote Sensing*, 49(10):3665–3676, 2011.

[10] Wei Gao, Jian Yang, and Wenting Ma. Land cover classification for polarimetric sar images based on mixture models. *Remote Sensing*, 6(5):3770–3790, 2014.

[11] Jean Richard Huynen. *Phenomenological theory of radar targets*. PhD thesis, TU Delft, Delft University of Technology, 1970.

[12] Shane R Cloude and Eric Pottier. An entropy based classification scheme for land applications of polarimetric sar. *IEEE Transactions on Geoscience and Remote Sensing*, 35(1):68–78, 1997.

[13] E Krogager. New decomposition of the radar target scattering matrix. *Electronics Letters*, 26(18):1525–1527, 1990.

[14] Anthony Freeman and Stephen L Durden. A three-component scattering model for polarimetric sar data. *IEEE Transactions on Geoscience and Remote Sensing*, 36(3):963–973, 1998.

[15] Yoshio Yamaguchi, Toshifumi Moriyama, Motoi Ishido, and Hiroyoshi Yamada. Four-component scattering model for polarimetric sar image decomposition. *IEEE Transactions on Geoscience and Remote Sensing*, 43(8):1699–1706, 2005.

[16] J. A. Kong, A. A. Swartz, H. A. Yueh, L. M. Novak, and R. T. Shin. Identification of terrain cover using the optimum polarimetric classifier. *Journal of Electromagnetic Waves and Applications*, 2(2):171–194, 1988.

[17] Jong-Sen Lee, Mitchell R Grunes, and R Kwok. Classification of multi-look polarimetric sar imagery based on complex wishart distribution. *International Journal of Remote Sensing*, 15(11):2299–2311, 1994.

[18] Jong-Sen Lee, Mitchell R Grunes, Thomas L Ainsworth, Li-Jen Du, Dale L Schuler, and Shane R Cloude. Unsupervised classification using polarimetric decomposition and the complex wishart classifier. *IEEE Transactions on Geoscience and Remote Sensing*, 37(5):2249–2258, 1999.

[19] Dirk H Hoekman and Martin AM Vissers. A new polarimetric classification approach evaluated for agricultural crops. *IEEE Transactions on Geoscience and Remote Sensing*, 41(12):2881–2889, 2003.

[20] Gonzalo Pajares, Carlos López-Martínez, F Javier Sánchez-Lladó, and Íñigo Molina. Improving wishart classification of polarimetric sar data using the hopfield neural network optimization approach. *Remote Sensing*, 4(11):3571–3595, 2012.

[21] L. Breiman. Random forests. *Mach. Learn.*, 45(1):5–32, 2001.

[22] Lien Loosvelt, Jan Peters, Henning Skriver, Bernard De Baets, and Niko EC Verhoest. Impact of reducing polarimetric sar input on the uncertainty of crop classifications based on the random forests algorithm. *IEEE Transactions on Geoscience and Remote Sensing*, 50(10):4185–4200, 2012.

[23] S Fukuda and H Hirosawa. Support vector machine classification of land cover: application to polarimetric sar data. *Geoscience and Remote Sensing Symposium*, 1:187–189, 2001.

[24] C Lardeux, P. L Frison, C Tison, J. C Souyris, B Stoll, B Fruneau, and J. P Rudant. Support vector machine for multifrequency sar polarimetric data classification. *IEEE Transactions on Geoscience and Remote Sensing*, 47(12):4143–4152, 2009.

[25] Jian Cheng, Yaqi Ji, and Haijun Liu. Segmentation-based polsar image classification using visual features: Rhlbp and color features. *Remote Sensing*, 7(5):6079–6106, 2015.

[26] John Wright, Allen Y Yang, Arvind Ganesh, S Shankar Sastry, and Yi Ma. Robust face recognition via sparse representation. *IEEE Transactions on Pattern Analysis and Machine Intelligence*, 31(2):210–227, 2009.

[27] Lamei Zhang, Liangjie Sun, Bin Zou, and Wooil M Moon. Fully polarimetric sar image classification via sparse representation and polarimetric features. *IEEE Journal of Selected Topics in Applied Earth Observations and Remote Sensing*, 8(8):3923–3932, 2015.

[28] Jilan Feng, Zongjie Cao, and Yiming Pi. Polarimetric contextual classification of polsar images using sparse representation and superpixels. *Remote Sensing*, 6(8):7158–7181, 2014.

[29] Michael B Wakin, Marco F Duarte, Shriram Sarvotham, Dror Baron, and Richard G Baraniuk. Recovery of jointly sparse signals from few random projections. In *Advances in Neural Information Processing Systems*, pages 1433–1440, 2006.

[30] Paul R Kersten, Jong-Sen Lee, and Thomas L Ainsworth. Unsupervised classification of polarimetric synthetic aperture radar images using fuzzy clustering and em clustering. *IEEE Transactions on Geoscience and Remote Sensing*, 43(3):519–527, 2005.

[31] Peter Yu, AK Qin, and David A Clausi. Unsupervised polarimetric sar image segmentation and classification using region growing with edge penalty. *IEEE Transactions on Geoscience and Remote Sensing*, 50(4):1302–1317, 2012.

[32] Neng Zhong, Wen Yang, Anoop Cherian, Xiangli Yang, Gui-Song Xia, and Mingsheng Liao. Unsupervised classification of polarimetric sar images via rie-

mannian sparse coding. *IEEE Transactions on Geoscience and Remote Sensing*, 55(9):5381–5390, 2017.

[33] Fumio Yamazaki and Masashi Matsuoka. Remote sensing technologies in post-disaster damage assessment. *Journal of Earthquake and Tsunami*, 1(03):193–210, 2007.

[34] Dominik Brunner, Guido Lemoine, and Lorenzo Bruzzone. Earthquake damage assessment of buildings using vhr optical and sar imagery. *IEEE Transactions on Geoscience and Remote Sensing*, 48(5):2403–2420, 2010.

[35] M Pesaresi, A Gerhardinger, and F Haag. Rapid damage assessment of built-up structures using vhr satellite data in tsunami-affected areas. *International Journal of Remote Sensing*, 28(13-14):3013–3036, 2007.

[36] Mustafa Turker and BT San. Detection of collapsed buildings caused by the 1999 izmit, turkey earthquake through digital analysis of post-event aerial photographs. *International Journal of Remote Sensing*, 25(21):4701–4714, 2004.

[37] Masashi Matsuoka and Fumio Yamazaki. Use of satellite sar intensity imagery for detecting building areas damaged due to earthquakes. *Earthquake Spectra*, 20(3):975–994, 2004.

[38] Masashi Matsuoka, Shunichi Koshimura, and Nobuoto Nojima. Estimation of building damage ratio due to earthquakes and tsunamis using satellite sar imagery. In *2010 IEEE International Geoscience and Remote Sensing Symposium (IGARSS)*, pages 3347–3349. IEEE, 2010.

[39] Masashi Matsuoka and Fumio Yamazaki. Building damage mapping of the 2003 bam, iran, earthquake using envisat asar intensity imagery. *Earthquake Spectra*, 21(S1):285–294, 2005.

[40] Milad Janalipour and Ali Mohammadzadeh. Building damage detection using object-based image analysis and anfis from high-resolution image (case study:

Bam earthquake, iran). *IEEE Journal of Selected Topics in Applied Earth Observations and Remote Sensing*, 9(5):1937–1945, 2016.

[41] Hiroyuki Miura, Saburoh Midorikawa, and Masashi Matsuoka. Building damage assessment using high-resolution satellite sar images of the 2010 haiti earthquake. *Earthquake Spectra*, 32(1):591–610, 2016.

[42] Milad Janalipour and Ali Mohammadzadeh. A fuzzy-ga based decision making system for detecting damaged buildings from high-spatial resolution optical images. *Remote Sensing*, 9(4):349, 2017.

[43] Yoshio Yamaguchi. Disaster monitoring by fully polarimetric sar data acquired with alos-palsar. *Proceedings of the IEEE*, 100(10):2851–2860, 2012.

[44] Gulab Singh, Yoshio Yamaguchi, Wolfgang-Martin Boerner, and Sang-Eun Park. Monitoring of the march 11, 2011, off-tohoku 9.0 earthquake with super-tsunami disaster by implementing fully polarimetric high-resolution polsar techniques. *Proceedings of the IEEE*, 101(3):831–846, 2013.

[45] Sang-Eun Park, Yoshio Yamaguchi, and Duk-jin Kim. Polarimetric sar remote sensing of the 2011 tohoku earthquake using alos/palsar. *Remote sensing of Environment*, 132:212–220, 2013.

[46] Lorenzo Bruzzone and Diego F Prieto. Automatic analysis of the difference image for unsupervised change detection. *IEEE Transactions on Geoscience and Remote sensing*, 38(3):1171–1182, 2000.

[47] Stuart Geman and Donald Geman. Stochastic relaxation, gibbs distributions, and the bayesian restoration of images. *IEEE Transactions on pattern analysis and machine intelligence*, (6):721–741, 1984.

[48] Si-Wei Chen and Motoyuki Sato. Tsunami damage investigation of built-up areas using multitemporal spaceborne full polarimetric sar images. *IEEE Transactions on Geoscience and Remote Sensing*, 51(4):1985–1997, 2013.

[49] Si Wei Chen, Xue Song Wang, and Motoyuki Sato. Urban damage level mapping based on scattering mechanism investigation using fully polarimetric sar data for the 3.11 east japan earthquake. *IEEE Transactions on Geoscience and Remote Sensing*, 54(12):6919–6929, 2016.

[50] Wei Zhai and Chunlin Huang. Fast building damage mapping using a single post-earthquake polsar image: a case study of the 2010 yushu earthquake. *Earth, Planets and Space*, 68(1):86, 2016.

[51] Xinwu Li, Huadong Guo, Lu Zhang, Xiao Chen, and Lei Liang. A new approach to collapsed building extraction using radarsat-2 polarimetric sar imagery. *IEEE Geoscience and Remote Sensing Letters*, 9(4):677–681, 2012.

[52] Lingli Zhao, Jie Yang, Pingxiang Li, Liangpei Zhang, Lei Shi, and Fengkai Lang. Damage assessment in urban areas using post-earthquake airborne polsar imagery. *International journal of remote sensing*, 34(24):8952–8966, 2013.

[53] Wei Zhai, Huanfeng Shen, Chunlin Huang, and Wansheng Pei. Building earthquake damage information extraction from a single post-earthquake polsar image. *Remote Sensing*, 8(3):171, 2016.

[54] TL Ainsworth, DL Schuler, and J-S Lee. Polarimetric sar characterization of man-made structures in urban areas using normalized circular-pol correlation coefficients. *Remote Sensing of Environment*, 112(6):2876–2885, 2008.

[55] Lei Shi, Weidong Sun, Jie Yang, Pingxiang Li, and Lijun Lu. Building collapse assessment by the use of postearthquake chinese vhr airborne sar. *IEEE Geoscience and Remote Sensing Letters*, 12(10):2021–2025, 2015.

[56] Weidong Sun, Lei Shi, Jie Yang, and Pingxiang Li. Building collapse assessment in urban areas using texture information from postevent sar data. *IEEE Journal of Selected Topics in Applied Earth Observations and Remote Sensing*, 9(8):3792–3808, 2016.

[57] LJ Cox. Ellipsometry and polarized light. *Journal of Modern Optics*, 25(3):270–271, 1978.

[58] Petr Beckmann and Joseph B. Keller. The depolarization of electromagnetic waves. *American Journal of Physics*, 40(10):1557–1557, 1972.

[59] George Gabriel Stokes. On the composition and resolution of streams of polarized light from different sources. *Transactions of the Cambridge Philosophical Society*, 9:399, 1851.

[60] Wolfgang M. Boerner and Wolfgang M. Boerner. Inverse methods in electromagnetic imaging. *Mathematics of Computation*, 46(174), 1986.

[61] Wolfgang M Boerner, Leonard A Cram, William A Holm, David E Stein, Werner Wiesbeck, Wolfgang Keydel, Dino Giuli, Dag T Gjessing, Frédéric A Molinet, and Hans Brand. *Direct and inverse methods in radar polarimetry*, volume 350. Springer Science & Business Media, 2013.

[62] E Lüneburg. Radar polarimetry: A revision of basic concepts. *Pitman Research Notes in Mathematics Series*, pages 257–275, 1996.

[63] Ernst LÜNEBURG. Principles of radar polarimetry. *IEICE Transactions on Electronics*, 78(10):1339–1345, 1995.

[64] Ernst Lüneburg. Polarimetric target matrix decompositions and the karhunen-loeve expansion. pages 2658–2660, Hamburg, 1999. IEEE International Geoscience and Remote Sensing Symposium.

[65] E. Krogager. New decomposition of the radar target scattering matrix. *Electronics Letters*, 26(18):1525–1527, 1990.

[66] Shane R Cloude and Eric Pottier. A review of target decomposition theorems in radar polarimetry. *IEEE Transactions on Geoscience and Remote Sensing*, 34(2):498–518, 1996.

[67] Anthony Freeman and Stephen L. Durden. A three-component scattering model for polarimetric sar data. *IEEE Transactions on Geoscience and Remote Sensing*, 36(3):963 – 973, 1998.

[68] Maxim Neumann, Laurent Ferro-Famil, and Eric Pottier. A general model-based polarimetric decomposition scheme for vegetated areas. *Proc. POLINSAR, Frascati*, 2009.

[69] Koji Kimura, Yoshio Yamaguchi, Toshifumi Moriyama, and Hiroyoshi Yamada. Circular polarization correlation coefficient for detection of non-natural targets aligned not parallel to sar flight path in the x-band polsar image analysis. *IEICE Transactions on Electronics*, 87(10):3050–3056, 2004.

[70] Michal Aharon, Michael Elad, Alfred Bruckstein, et al. K-svd: An algorithm for designing overcomplete dictionaries for sparse representation. *IEEE Transactions on Signal Processing*, 54(11):4311, 2006.

[71] Meng Yang, Lei Zhang, Xiangchu Feng, and David Zhang. Sparse representation based fisher discrimination dictionary learning for image classification. *International Journal of Computer Vision*, 109(3):209–232, 2014.

[72] Jong-Sen Lee. Refined filtering of image noise using local statistics. *Computer Graphics and Image Processing*, 15(4):380–389, 1981.

[73] Stefan Uhlmann and Serkan Kiranyaz. Integrating color features in polarimetric sar image classification. *IEEE Transactions on Geoscience and Remote Sensing*, 52(4):2197–2216, 2014.

[74] E Pottier. Unsupervised classification scheme of polsar images based on the complex wishart distribution and h/a/α polarimetric decomposition theorems. In *Proc. European Conf. on Synthetic Aperture Radar: EUSAR, 2000*, 2000.

[75] Joel A Tropp and Anna C Gilbert. Signal recovery from random measurements via orthogonal matching pursuit. *IEEE Transactions on Information Theory*, 53(12):4655–4666, 2007.

[76] Marshall F. Tappen and William T. Freeman. Comparison of graph cuts with belief propagation for stereo, using identical mrf parameters. In *IEEE International Conference on Computer Vision, 2003. Proceedings*, pages 900–906 vol.2, 2003.

[77] Meng Yang, Lei Zhang, Jian Yang, and David Zhang. Metaface learning for sparse representation based face recognition. In *17th IEEE International Conference onImage Processing (ICIP), 2010*, pages 1601–1604. IEEE, 2010.

[78] Julien Mairal, Marius Leordeanu, Francis Bach, Martial Hebert, and Jean Ponce. Discriminative sparse image models for class-specific edge detection and image interpretation. In *European Conference on Computer Vision*, pages 43–56. Springer, 2008.

[79] Haixia Bi, Jian Sun, and Zongben Xu. Unsupervised polsar image classification using discriminative clustering. *IEEE Transactions on Geoscience and Remote Sensing*, 55(6):3531–3544, 2017.

[80] Liu Yang and Rong Jin. Distance metric learning: A comprehensive survey. *Michigan State Universiy*, 2(2), 2006.

[81] Eric P Xing, Michael I Jordan, Stuart J Russell, and Andrew Y Ng. Distance metric learning with application to clustering with side-information. In *Advances in neural information processing systems*, pages 521–528, 2003.

[82] U.s. geological survey, magnitude 9.0v near the east coast of honshu, japan. `http://earthquake.usgs.gov/`.

[83] Geospatial information authority of japan (gsi), tsukuba, japan. `http://www.gsi.go.jp/kikaku/kikaku40014.html`.

[84] Japan aerospace exploration agency. `http://global.jaxa.jp/`.

[85] M Shimada, M Watanabe, M Takahashi, T Motooka, M Ohki, T Yamanokuchi, Y Miyagi, N Kawano, T Shiraishi, and R Thapa. Monitoring the great east japan earthquake using alos. *IEEE GRSS Newsletter*, pages 19–24, 2011.

[86] Masanobu Shimada, Takeo Tadono, and Ake Rosenqvist. Advanced land observing satellite (alos) and monitoring global environmental change. *Proceedings of the IEEE*, 98(5):780–799, 2010.

[87] Shane R Cloude and Konstantinos P Papathanassiou. Polarimetric sar interferometry. *IEEE Transactions on Geoscience and Remote Sensing*, 36(5):1551–1565, 1998.

[88] Shane Cloude. *Polarisation: applications in remote sensing*. Oxford University Press, 2010.

[89] Martin Baatz. Multiresolution segmentation: an optimization approach for high quality multi-scale image segmentation. *Angewandte Geographische Informations verarbeitung XII*, pages 12–23, 2000.

[90] Chih-Chung Chang and Chih-Jen Lin. Libsvm: a library for support vector machines. *ACM Transactions on Intelligent Systems and Technology (TIST)*, 2(3):27, 2011.

[91] HT Li, HY Gu, YS Han, and JH Yang. Object-oriented classification of polarimetric sar imagery based on statistical region merging and support vector machine. In *International Workshop on Earth Observation and Remote Sensing Applications*, pages 1–6. IEEE, 2008.

[92] Stefan Uhlmann and Serkan Kiranyaz. Integrating color features in polarimetric sar image classification. *IEEE Transactions on Geoscience and Remote Sensing*, 52(4):2197–2216, 2014.

[93] Building damage map for tohoku earthquake/tsunami. http://www.tsunami.civil.tohoku.ac.jp/tohoku2011/mapping_damage.html.

[94] Si Wei Chen and Motoyuki Sato. Tsunami damage investigation of built-up areas using multitemporal spaceborne full polarimetric sar images. *IEEE Transactions on Geoscience and Remote Sensing*, 51(4):1985–1997, 2013.

[95] Kilian Q Weinberger and Lawrence K Saul. Distance metric learning for large margin nearest neighbor classification. *Journal of Machine Learning Research*, 10(Feb):207–244, 2009.

[96] Jerome H Friedman. Greedy function approximation: a gradient boosting machine. *Annals of statistics*, pages 1189–1232, 2001.

[97] Masumi Yamada, Junzo Ohmura, and Hiroyuki Goto. Wooden building damage analysis in mashiki town for the 2016 kumamoto earthquakes on april 14 and 16. *Earthquake Spectra*, 33(4):1555–1572, 2017.

[98] Shigeyuki Okada and Nobuo Takai. Classifications of structural types and damage patterns of buildings for earthquake field investigation. In *Proceedings of the 12th world conference on earthquake engineering, Auckland, New Zealand*, volume 30, pages 1–8, 2000.

[99] Jong-Sen Lee, Dale L Schuler, and Thomas L Ainsworth. Polarimetric sar data compensation for terrain azimuth slope variation. *IEEE Transactions on Geoscience and Remote Sensing*, 38(5):2153–2163, 2000.

[100] Yuliya Tarabalka, Jón Atli Benediktsson, and Jocelyn Chanussot. Spectral–spatial classification of hyperspectral imagery based on partitional clustering techniques. *IEEE Transactions on Geoscience and Remote Sensing*, 47(8):2973–2987, 2009.